Catalysis Today 162 (2011) 1–48

Contents lists available at ScienceDirect

Catalysis Today

journal homepage: www.elsevier.com/locate/cattod

Review

Methane decomposition to CO_x-free hydrogen and nano-carbon material on group 8–10 base metal catalysts: A review

Yongdan Li*, Douxing Li, Gaowei Wang

Tianjin Key Laboratory of Applied Catalysis Science and Technology and State Key Laboratory of Chemical Engineering (Tianjin University), School of Chemical Engineering, Tianjin University, Tianjin 300072, China

ARTICLE INFO

Article history:
Received 15 August 2010
Received in revised form
14 December 2010
Accepted 24 December 2010

Keywords:
Methane catalytic decomposition
CO_x-free hydrogen
Carbon nano-material
High efficient chemical energy conversion
Kinetics and catalyst

ABSTRACT

Methane catalytic decomposition is a promising process that simultaneously produces CO_x-free hydrogen and carbon nanomaterial. The hydrogen produced can be consumed directly by proton exchange membrane fuel cell (PEMFC), while the carbon can be used as the fuel of direct carbon fuel cell (DCFC) and as the components of advanced materials. The recent advances in the reaction mechanism and kinetics on group 8–10 base metal catalysts are reviewed. Special attention is paid to the roles of metal particles and the deactivation mechanism of the catalyst during the reaction. The performances of the often used catalysts are summarized and the effects of the promoters, supports and preparation techniques are outlined. The kinetic models derived from different mechanism and the empirical correlations are compared. The process characteristics, such as the origin of the trace amount of CO in the product, the process factors influencing CO formation and the overall catalyst productivity are discussed. Processes based on the topic reaction and their applications are introduced.

Contents

* Corresponding author. Tel.: +86 22 27405613; fax: +86 22 27405243.
E-mail address: ydli@tju.edu.cn (Y. Li).

0920-5861/$ – see front matter © 2011 Elsevier B.V. All rights reserved.
doi:10.1016/j.cattod.2010.12.042

Nomenclature

AES	auger electron spectroscopy
AFCs	alkaline fuel cells
C_{b1}	a carbon atom in the bulk phase of the nickel crystal at a subsurface site ss1 just below the surface on which the surface reaction takes place
C_{b2}	a carbon atom at a subsurface site ss2 just below the interface between the nickel particle and the carbon segregating out the nickel particle
$c_{C,(Ni,f)}$	the concentration of carbon dissolved in nickel at the front of the particle
CNFs	carbon nanofibers
$C_{Ni,f}$	carbon dissolved in nickel at the front of the particle, just below the selvedge
$C_{Ni,r}$	concentration of carbon dissolved in nickel at the rear of the particle
CNMs	carbon nanomaterials
CNTs	carbon nanotubes
Cp	the encapsulating carbon
CSTR	continuous stirred tank reactor
CT	total concentration of sites
CTR	constant-temperature reaction
C_W	carbon precipitation from the nickel particle
DCFC	direct carbon fuel cell
DDM	direct dissociation mechanism
DFT	density functional theory
DWCNTs	double-walled carbon nanotubes
EELS	electron energy loss spectroscopy
E_o	apparent activation energy of the carbon deposit formation
EXAFS	edge X-ray absorption fine structure
FBR	fixed-bed reactor
FC	Feitknecht compound
FLBR	fluidized bed reactor
HRTEM	high resolution transmission electron microscope
IR	infrared spectroscopy
IRSOFC	internal reforming solid-oxide fuel cell
k	specific rate constant for MCD reaction
K_C	equilibrium constant for carbon adsorption
K_{CH_4}	equilibrium constant for CH_4 adsorption
k_d	specific constant for the rate of deactivation reaction
K_e	equilibrium constant for MCD reaction
K_{H_2}	equilibrium constant for hydrogen adsorption
k_i^+, k_i^-	rate constants of the forward and the reverse reactions of the step i
K_i	equilibrium constant for step i
k_M^+, k_M^-	rate constants of the forward and the reverse reactions of the rate-determining step
k_o	pre-exponential factor in the reaction rate constant
K_W	equilibrium constant for carbon precipitation
LEED	low-energy electron diffraction
MCD	methane catalytic decomposition
MLR	multilayer reactor
MSI	metal–support interaction
MWCNTs	multi-walled carbon nanotubes
NAFLBR	nano-agglomerated FLBR
PEMFC	proton exchange membrane fuel cell
PFR	plug flow reactor
p_i	the partial pressure of component i
PIR	pre-induction reaction
PMM	precursor mediated mechanism
r	rate of MCD reaction
S	surface active site
SAD	selective area diffraction
SWCNTs	single-walled carbon nanotubes
TEM	transmission electron microscope
TEOM	tapered-element oscillating microbalance
TPCR	temperature programmed catalytic reaction
TPD	temperature programmed desorption
UHV	ultra-high vacuum
XANES	X-ray absorption near edge structure
XPS	X-ray photoelectron spectroscopy
XRD	X-ray diffraction

Greek letters

θ_i	the concentration of sites occupied by species i
θ^*	the concentration of sites which are not occupied

1. Introduction

The fossil-fuel-based energy infrastructure has encountered two major challenges: sustainability and environmental impacts [1,2]. It is now clear that fossil fuels will run out sooner than many expected because of the rapid increase in demand and the limited reserves in the earth. On the other hand, the ever increasing consumptions of fossil fuels cause serious environmental problems. CO_2, C_xH_y, NO_x, SO_x and other products resulting from the combustion of fossil fuels have resulted in environmental deterioration, including global warming and the acid rain [3–5]. The other types of energy resources, such as wind, solar and bio will not be the major energy sources in the near future because of their high cost and immature technology. Nuclear energy provides an alternative, however, it also raises a lot of safety concerns. The energy industry, governments and scientific communities reached a consensus that fossil fuels will remain as a major source of energy for foreseeable future, and the most feasible strategies will include: (1) to reduce consumption of fossil fuels; (2) to develop renewable energy resources and technologies; and (3) to control the negative environmental impacts of fossil fuel consumption [6–8].

Hydrogen economy has raised much attention in the last two decades because of its successful demonstration in space technologies, although it needs on purpose manufacture of hydrogen which is complex and costly [9–15]. With hydrogen as an energy carrier, an energy-efficient transportation system can be built to replace a significant amount of petroleum [16]. Hydrogen can be produced from various sources and transformed into electricity and other energy forms with a low pollution [17,18]. The transformation technology is based on fuel cells, which are devices with potentially total efficiency if calculated on the basis of exergy, because the processes are not limited by Carnot cycle thermal efficiency. Therefore,

Table 1
Different approaches to produce CO_x-free hydrogen.

Process	ΔH_{773} (kJ/mol H_2)	Reaction temperature	Cost	Coproduct
H_2O electrolysis	246.35	Room temperature	High	O_2 with low value
NH_3 decomposition	35.57	698–798 K	Low	N_2 with no value
CH_4 decomposition	43.23	Above 773 K	Medium	C with high value
Step-wise reforming of methane	43.23	723–873 K	Medium	H_2 containing CO_x with low value

a "hydrogen economy" is a concept in which energy is utilized the most effectively and cleanly. However, hydrogen is not a primary energy source, and should be produced from other resources.

The present commercial production of hydrogen is mainly based on steam reforming and partial oxidation of hydrocarbons and carbonaceous feed stocks, such as natural gas, petroleum fractions and coal [19–25]. Trimm and Onsan [26] reviewed the on-board hydrogen production techniques and also suggested that a combination of steam reforming and partial oxidation of hydrocarbon fuels are still the most promising processes for the hydrogen fueled vehicles. However, these processes produce carbon monoxide (CO) as the intermediate product, which needs to be cleaned off with high cost. This purification process also produces carbon dioxide (CO_2) which exerts a great contribution to the global warming [3,5,11]. CO_2 sequestration technologies for hydrogen production are under intensive investigation and development [27–29]. However, in order to meet the demands, the cost for conventional production of hydrogen from fossil fuels will significantly increase if combined with sequestration technology [11,30–32].

Compared to the other fossil fuels, natural gas is a better feed for the production of hydrogen [33–35]. It is widely available, easy to handle, and has a high hydrogen-to-carbon ratio. Steam reforming of methane has been the largest and the most economical and popular technology, which contributes about 50% of the world production of hydrogen [20]. However, this process produces CO_2 and CO. In addition, CO and CO_2 in hydrogen feed are harmful to low temperature fuel cells, e.g. proton exchange membrane fuel cells (PEMFCs) require CO less than a few ppm, and CO_2 in ppm level is poisonous to alkaline fuel cells (AFCs) [36]. To obtain CO_x-free hydrogen from syngas, several catalytic reaction steps and high pressure washing techniques are employed, but these procedures are both investment intensive and material consuming [37].

Several technologies are available for directly obtaining CO_x-free hydrogen, as listed in Table 1. Water electrolysis is now a widely used process to obtain high purity hydrogen. However, this process is economically inferior to the hydrocarbon based processes. Several researchers suggested that ammonia catalytic decomposition can both be economical and convenient for producing CO_x-free hydrogen [38–47]. The conversion of ammonia approaches 100% at 900 and 973 K on Ru/SiO_2 and Ir/Al_2O_3 catalysts, respectively [40]. The advantage is that the storage and transportation of ammonia is much easier than hydrogen because ammonia is at liquid state under room temperature and 8 bar pressure. There is already a very large scale and mature ammonia synthesis industry. Nevertheless, several critical issues may have been overlooked. First of all, ammonia is synthesized from hydrogen, and the technology applied for hydrogen production is critical for this ammonia route to be environmentally and economically sound. Secondly, ammonia is an environment-polluting gas, with extremely unpleasant and unhealthy effects on human. Finally, ammonia itself, even at ppm level, is poisonous to the catalyst of PEMFC [48–50]. The ammonia decomposition process is moderately endothermic, and a complete decomposition of ammonia needs a fairly high temperature. Anyhow, the ammonia route provides a seemingly feasible option for hydrogen storage and carriage.

Methane catalytic decomposition (MCD) reaction

$$CH_4 \rightarrow C + 2H_2 \quad \Delta H^0_{298} = 74.8\,\text{kJ/mol} \tag{1}$$

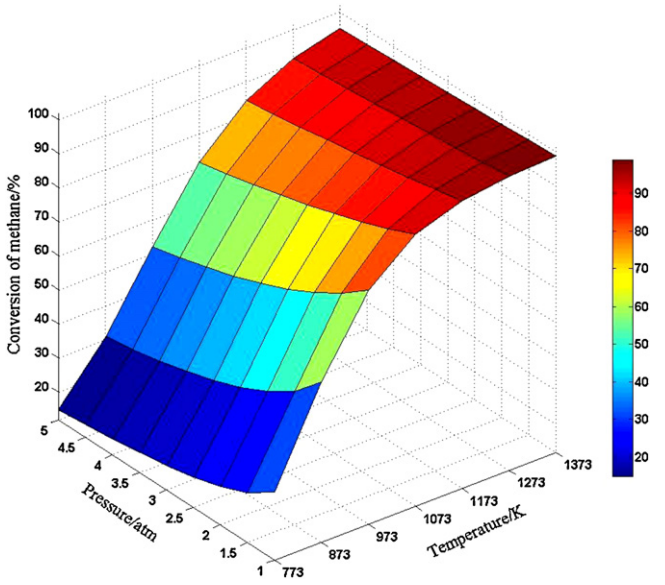

Fig. 1. Equilibrium conversion of methane under different pressure and temperature.

is moderately endothermic. Fig. 1 depicts the equilibrium conversion of methane and the equilibrium concentration of hydrogen in the product gas. The equilibrium conversion curve of the reaction is very close to that of the methane steam reforming reaction with a feed of a stoichiometric steam/methane ratio [51]. MCD reaction has been a topic of great interest for a long time [52]. In 2000, we proposed a hypothesis to produce CO_x-free hydrogen and carbon nanomaterials (CNMs) simultaneously via MCD reaction [51]. Now, the reaction has become an attractive alternative route both for clean hydrogen and for value-added carbon material due to its simplicity in process flow sheet and high efficiency [53–57]. An additional advantage of this process is that, in principle, it does not produce any carbon dioxide. Therefore, it is extremely environmentally attractive due to the concern of the global warming problems associated with the over load emission of carbon dioxide into the air-sphere of the earth [51]. The products are easily separated because that the carbon produced is at solid state and the hydrogen obtained can be used directly by PEMFC without further purification [51]. The co-produced carbon nanotubes (CNTs) or carbon nanofibers (CNFs) have also been investigated extensively because of their excellent properties and great potentials for many utilization purposes [58–69]. Two recent articles reviewed the close topics with emphasizes on different aspects of the MCD and the related reactions [70,71].

Recently, several colleagues suggested that the CNMs can be used as the consuming anode of a direct carbon fuel cell (DCFC) [72,73], and recommended a concept of high efficiency energy conversion system based on MCD reaction and two types of fuel cell stacks, viz. a PEMFC consuming the hydrogen and a DCFC using the carbon with high purity and activity [47,56]. Liu et al. [74] recently proposed another alternative system incorporating an internal reforming solid-oxide fuel cell (IRSOFC) instead of the PEMFC with the MCD reactor and the DCFC stack.

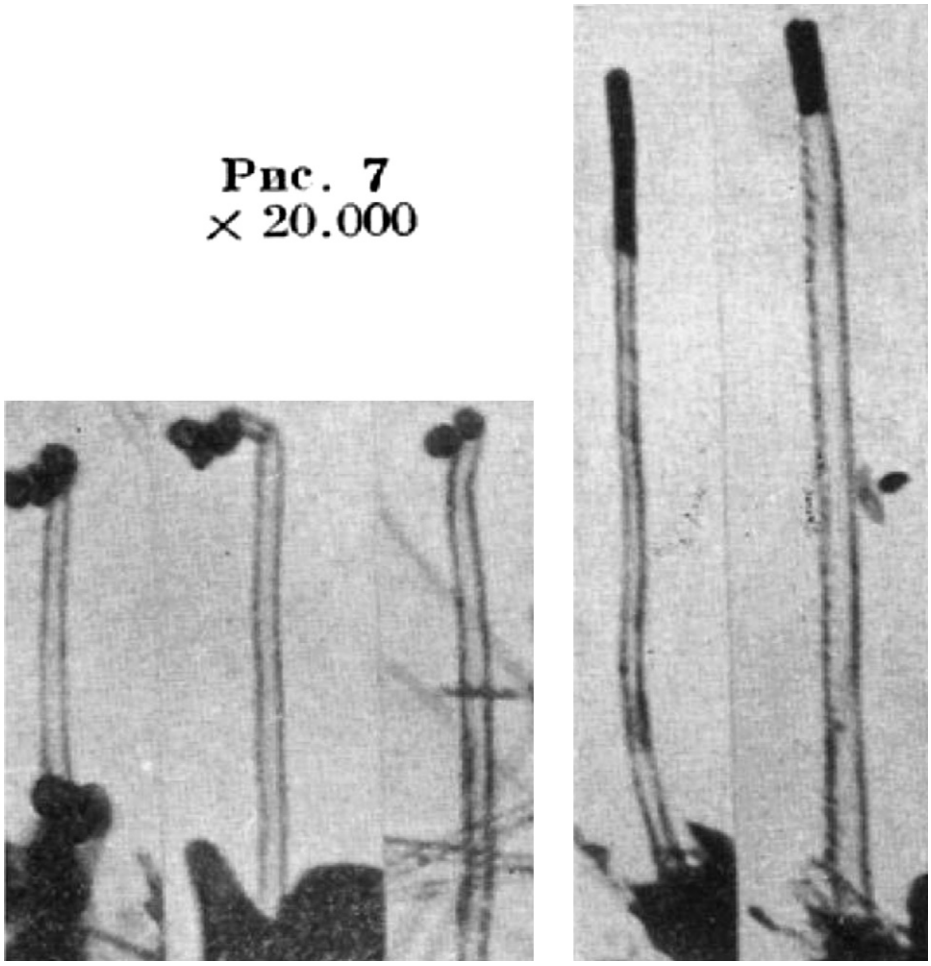

Fig. 2. The very first record of CNTs with TEM. The carbon whiskers grew from the catalyst are well tubular. The metal tips are also seen clearly, however, with different appearances to each other.
Reprinted from [95] with permission of Nauka Publishers.

It is obvious that a high methane conversion is favorable for any application purpose, so that the reaction is better to be carried out at a temperature above 1073 K. A hydrogen stream with near 100% concentration is often demanded, therefore, sometimes it is necessary to conduct the reaction at even higher temperatures, viz. close to 1273 K. Several feasible processes based on MCD also have been proposed. Step-wise reforming is a process combining MCD and deposited carbon oxidative gasification which regenerates the catalyst [75–79]. In this process, MCD is operated at low temperature with low surface carbon coverage and this eases the consequent regeneration of the catalyst with H_2O, O_2 or CO_2. Several research groups proposed to perform MCD on a carbon catalyst in order to eliminate the catalyst regeneration step [80–84]. However, the low methane conversion and the fast catalyst deactivation have to be dealt with in order for it to be practical [82,83,85,86]. MCD reaction on carbon catalysts, such as carbon black, activated carbon, ordered mesoporous carbon, CNF and graphite, needs a high activation energy (143–236 kJ/mol) and has to be operated at higher temperatures (1073–1373 K) than on metal catalysts [83,86–91]. The activity is found to be a function of the carbon conformation [81–83], surface area [81,83], and amount of defects present in the graphene layers [92]. A recent review article [71] discussed the carbon catalyzed MCD reaction with an extent of detailed literature update. Therefore, this article will concentrate on the literature review of the MCD reaction on group 8–10 base metals.

The production of carbon fibers by hydrocarbon decomposition can be traced back to the late 19th century. In a patent dated June 18, 1889, it was recorded that thin carbon filament with great mechanical strength and electrical conductivity was obtained through high temperature hydrocarbon decomposition [93]. The catalyst-assisted growth of carbon fibers was first explored by a French group in 1890 [94]. The invention of the transmission electron microscope (TEM) in 1939 provided a direct tool for observing the morphology of the carbon fibers. Radushkevich and Lukyanovich presented micrographs of carbon fibers (Fig. 2) as early as in 1952 [95]. In their work, tubular fibers with diameters in nano-scale were observed. This was proved to be the first record of CNTs with TEM [96]. In the following years, it was found that the carbon fibers have excellent mechanical properties and a great potential for utilization as materials [97–104]. Baird et al. [105] studied the structure of carbon fibers formed from methane and propane decomposition on Ni foil catalyst with a high resolution TEM (HRTEM), and they found that the tips of the fibers had nests for the metal particles. They further recognized that the carbon fibers have a graphite structure with a 0.34 nm space of the (0 0 0 2) lattice planes, larger than that of graphite. Carbon fibers with good mechanical properties were obtained at relatively high temperatures (~1273 K) on transition metal catalysts, and reported that the length of the fibers ranges from several microns to several centimeters and the diameter in nanometers to microns [106–108]. In recent years, the growth of CNFs on various transition metal catalysts has been explored inten-

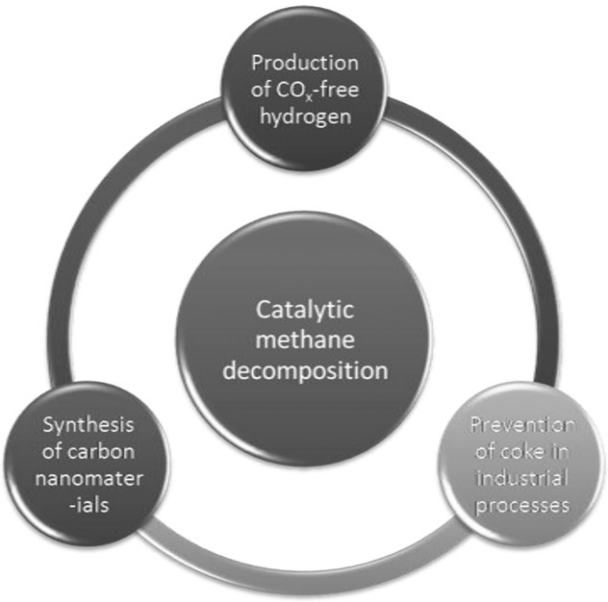

Fig. 3. The driving force for the research activities on the methane catalytic decomposition reaction. It should be noted that the different interests were addressed in different time periods. The understanding and prevention of coking on commercial metal catalyst were the earliest and have been the long lasting interest on this reaction. Then the synthesis of carbon fibrous material was explored much earlier than the emergence of the concept of carbon nanotubes.

sively [51,53,109,110], and several pilot tests have been reported [111].

The mechanism and kinetics of hydrocarbon decomposition on metal catalysts have been investigated over a long period of time because of the need for moderating deactivation due to coke formation in commercial processes, e.g. steam reforming of hydrocarbons, methanation and other processes involving hydrocarbons and carbon monoxide and employing transition metal as catalyst [112–124]. The coke formed in such processes covers active sites, blocks pores of the support and reduces mechanical strength of the catalyst. The carbon formed during the reactions of methane decomposition and carbon monoxide disproportionation always had a fibrous, sometimes tubular morphology [125–128]. These carbons formed during catalytic reactions on metals have been called filamentous carbon, carbon whisker, fibrous carbon or carbon fibril at different times and with different research purposes [129–132]. The illustration by TEM image of the structure of very thin CNTs in 1991 [58] and the discovery of single-walled CNTs (SWCNTs) in 1993 almost simultaneously by Iijima and Ichihashi [133] and Bethune et al. [134] made this family of carbon materials more attractive to the scientific community. So far, SWCNTs have been investigated extensively and many exciting hypothesis have been proposed and tested. Much work has been done to reveal their structural, electrical, mechanical, electromechanical, and chemical properties [62,135,136].

The interests on MCD reaction research are outlined in Fig. 3. Apparently, the reaction has been explored with a great cumulative effort. The improvement of physical tools for being able to investigate even smaller scale at faster speed often leads to substantial advancement in understanding the reaction system. Recently, many *in situ* and *on operando* technologies as well as novel simulation methods have been applied to the MCD research. However, several major challenges for the understanding of the mechanism, the design of the catalyst and the optimization of the reactor still remain.

In [70], the literature on the thermal and plasma aided hydrocarbon decomposition has been reviewed. This work will provide a historical overview and a perception of the reaction on group 8–10 based metal catalysts with focusing on the recent developments with the following key respects: the reaction mechanism, the catalyst, the kinetics, the process needs, the reactor design and perspectives to its future.

2. Reaction mechanism

2.1. An outline

MCD reaction is complex because it involves many phases and steps. MCD, other hydrocarbon decomposition and CO disproportionation reactions have some similar surface reaction pathways and intermediate species, and their mechanisms have been generally outlined as in Refs. [137–139]. MCD reaction is often simplified as including such key steps as methane activation, carbon nucleation and CNT or CNF growth. Methane molecules adsorb dissociatively on metal surface. It gives out carbon atoms with a concomitant desorption of molecular hydrogen. The adsorbed carbon atoms diffuse on the surface or through the bulk of metal particle to a suitable area for graphene sheets formation where the CNT or CNF forms. A number of excellent reviews discussed this mechanism [60,140]. However, this mechanism over simplifies the process. CNF formation on a metal catalyst involves geometry, interface, phase and energy factors and many chemical and physical steps.

2.2. Information from the conformation of formed carbon

The conformation of the formed carbon contains information of its growth mechanism, though deduction is required for understanding the microscopic process. From the structure and morphology of the nanocarbon, reasonable information on its formation mechanism can be derived. Several nanocarbon structures, such as CNTs [110,141–143], CNFs [128,144–149], nanoonions [150,151] and carbon encapsulated metal [119] were obtained in the MCD reaction (see Fig. 4). With these primary structures, different morphologies and textures, such as parallel bundles, octopus like units, and self woven particles are formed [51,144,152]. It has been found that the formation of a particular structure, texture and morphology depends on reaction conditions, i.e. the catalyst, temperature, pressure, gas phase composition and fluid field.

Perfect SWCNT is a cylinder of 3-coordinated carbon, which can be represented with the rolling up of a graphene layer at a certain angle, and multi-walled CNT (MWCNT) consists of many annular concentric cylinders with an interlayer spacing close to that of the graphite [132,153]. The CNTs, if they look like, formed in MCD and other hydrocarbon decomposition reactions always display defects and asymmetric structures [154]. Those formed in MCD are more often CNFs. The structure of CNFs can be classified by the angle α, as shown in Fig. 5, between the graphene layers in the projected image [155]. While α value of the platelet CNFs is close to 180°, the fishbone-type has sharper α values, i.e. $30^\circ < \alpha < 150^\circ$. Tubular CNFs always have small α values, i.e. <0°. CNFs with bamboo structure have a periodical repetition of hollow caves, which are formed by periodical movement of metal particles [147,156]. Carbon onion is another graphite-structured material. It is composed of spherical multilayer graphene-based shell and hollow or metal particle filled core. The distance between graphitic planes in the shell is also close to the *d* spacing of graphite [150,151,157].

The structure of CNM formed in MCD reaction is closely related to the properties of the metal particles and the reaction conditions [147,154,155,158]. The basic properties of the metal particles are size and composition depending on the preparation and the pre-treatment of the catalyst. Other properties such as state of

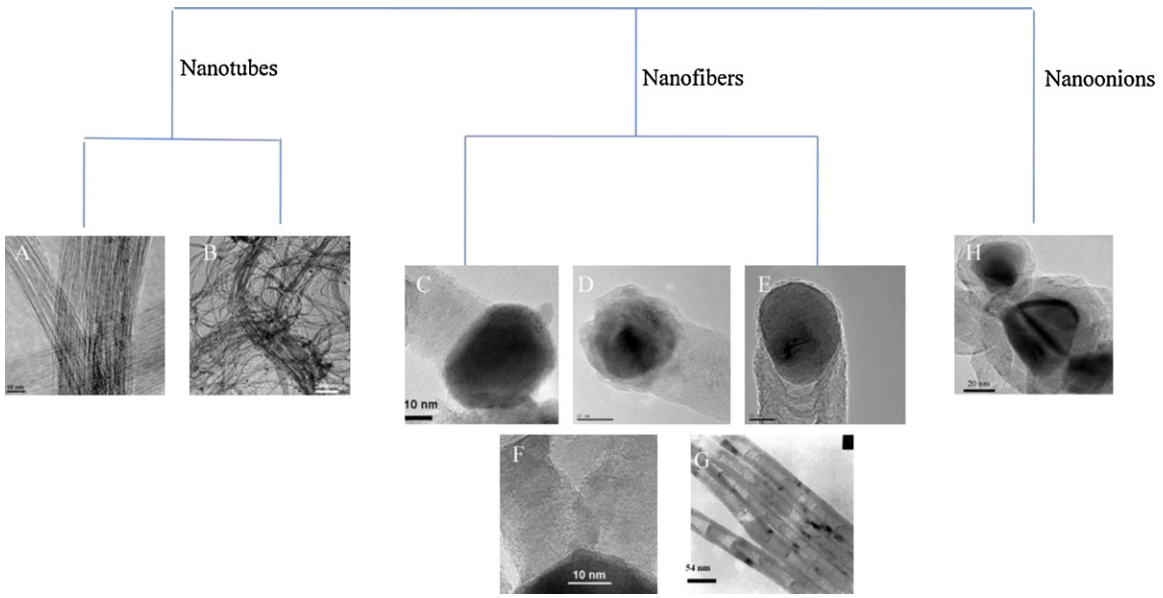

Fig. 4. Various types of nanocarbon formed in MCD reaction. (A) SWCNTs [143]; (B) MWCNTs [152]; (C, D, E) regular CNFs with different α values (the definition is illustrated in Fig. 5) [155,158]. (F) octopus CNFs [155]; (G) bamboo-shaped CNFs [147]; (H) carbon nanoonions [151].
Reprinted from [147,155] with permission of the Royal Chemical Society and from [143,151,152,158] with permission of Elsevier Science Publishers B.V.

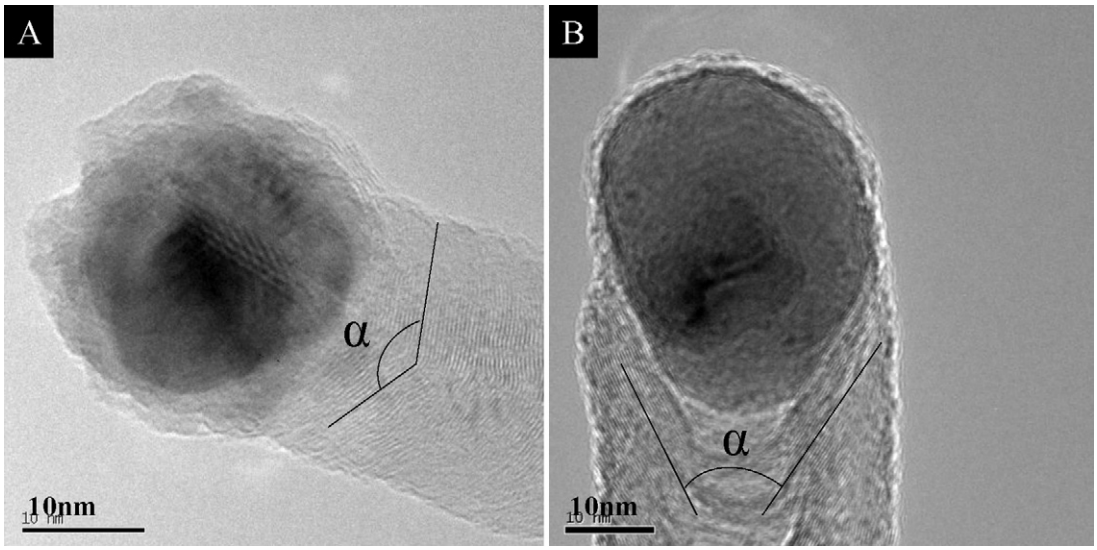

Fig. 5. The definition of the angle α between the graphene layers in the projected images.
Reprinted from [158] with permission of Elsevier Science Publishers B.V.

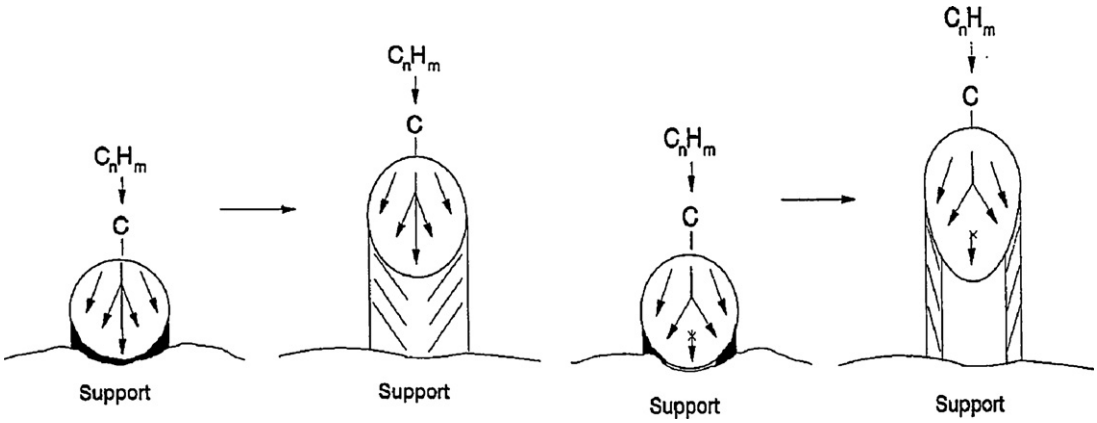

Fig. 6. Schematic pictures of the formation of a full fiber (left) and a hollow tube (right).
Reprinted from [166] with permission of Elsevier Science Publishers B.V.

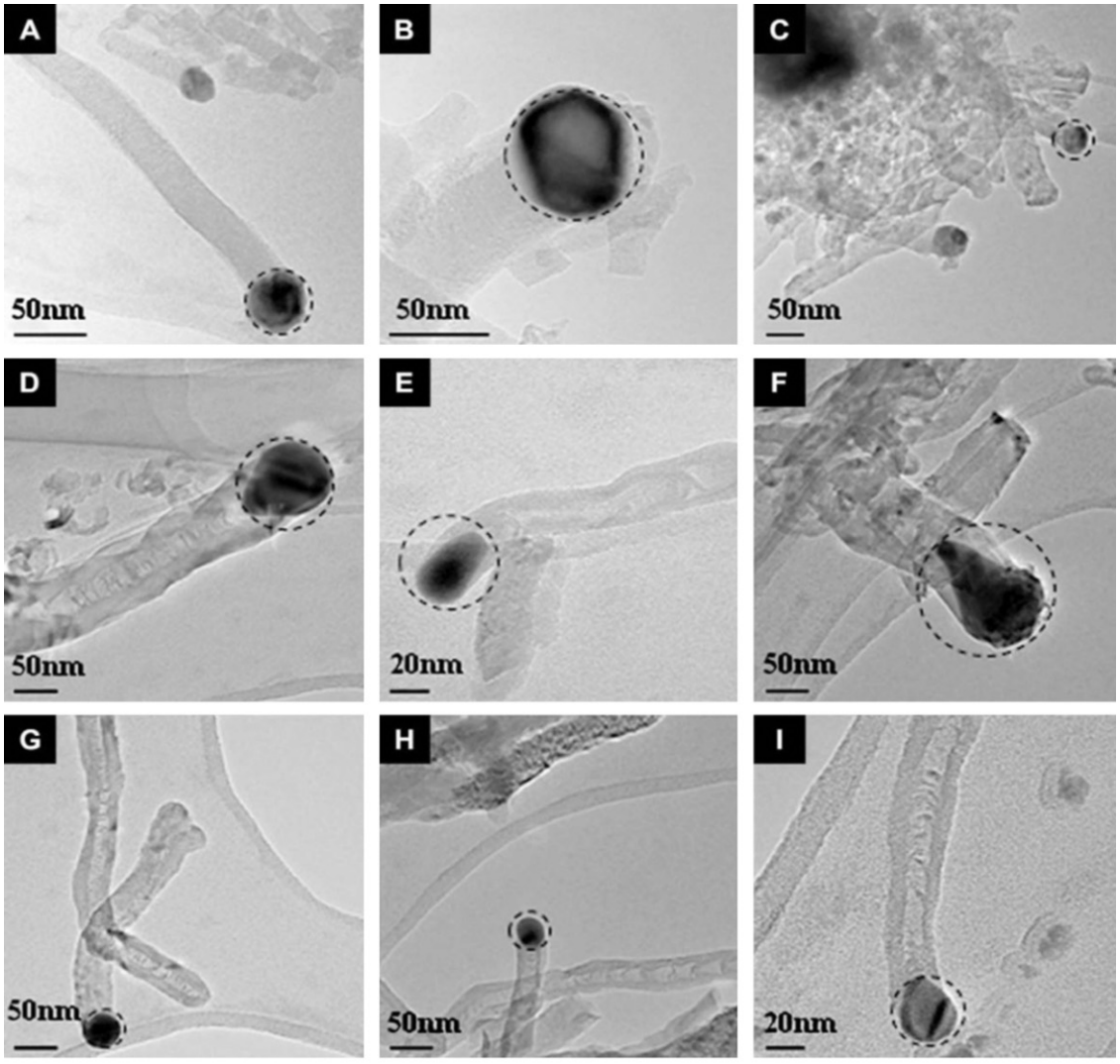

The local compositions measured by EDS

Samples	Microarea	Ni/Cu (mol/mol)
CTR 816 K	A	3.2:1
	B	4.7:1
	C	3.9:1
CTR 1013 K	D	0.89:1
	E	0.89:1
	F	0.96:1
PIR 1013 K	G	3.6:1
	H	2.6:1
	I	2.8:1

Fig. 7. Top: The micrographs of the metal particles and the carbon nanofibers formed in the reaction. Bottom: The corresponding Ni/Cu ratio of the metal tip associated with the carbon fiber measured with an EDX technique. The fibers formed during constant temperature reaction at 816 K (A–C); during constant temperature reaction at 1013 K (D–F); during the reaction with pre-induction at 823 K for 10 min and then reaction at 1013 K (G–I).
Reprinted from [158] with permission of Elsevier Science Publishers B.V.

the particles, affinity to the graphite structure, and catalytic performance are dependent on the basic properties and reaction conditions. Nevertheless, it is easy to understand that the CNM structure depends on the metal–graphite interface. The formation of the graphite layer occurs on the specific faces of the metal crystal. Audier et al. [159–161] investigated CNF formation on fcc-structured Fe–Co, Fe–Ni alloys and bcc-structured Fe–Co alloys using a TEM/SAD technique, and found that the gas/metal interface is (1 0 0) face for the bcc–Fe–Co alloys while it is (1 1 1) for the fcc–Fe–Co and Fe–Ni alloys. Yang and Chen [162] examined the growth of CNFs on Ni catalyst with the same technique and indicated that the Ni (1 0 0) and Ni (1 1 0) surfaces are the gas/metal interfaces, while the Ni (1 1 1) and Ni (3 1 1) surfaces form the graphite/metal interfaces. Furthermore, extended Hückel molecular orbital calculations indicate that the (1 1 1) and (3 1 1) faces of Ni provide stronger epitaxial fits with graphite. *In situ* TEM technique demonstrates that new graphene sheets formed at the graphene–Ni interface with their basal (0 0 2) planes orienting parallel to the Ni surface [154,163]. Chesnokov et al. [164] prepared CNFs on a Ni–Cu/MgO catalyst. Their TEM images showed that the metallic particles are at the end of the CNFs. Their selective area diffraction (SAD) proved that the Ni (1 1 1) face is the most developed one on the metal surface. This face is perpendicular to the direction of the CNF growth and contacts with the (0 0 2) planes of graphite. The unoccupied side is the Ni (1 0 0) faces, which are not contacting with the formed carbon. These faces appear to be the centers for the MCD reaction.

The morphology of CNFs is dependent on the feature of catalyst and reaction conditions [51,147,155,165]. Monthioux et al. [155] examined the carbon formed on a Ni–Cu–Mg–Al catalyst and found that the structure of the CNFs formed is closely related to the physical properties of metal particles which in turn depend on the Ni/Cu ratio. Snoeck et al. [166] investigated the effect of reaction temperature on the morphology of CNFs and found that full CNFs form at low temperature and hollow CNFs form at high temperature. They attributed this to the different carbon atom diffusion rate in the bulk of metal particles at different temperatures (see Fig. 6). This phenomenon was also observed in other works [165,167]. Takenaka et al. [167] obtained dense CNFs with a diameter range in 10–30 nm on a Co catalyst at 773 K, hollow CNFs in the temperature range of 873–973 K, and spiral CNTs and bamboo-shaped CNTs both at 1073 K. CNFs with different structures are also obtained at different reaction temperatures on a Ni–Cu/Al_2O_3 catalyst [137,147,165]. In 773–873 K, octopus-like CNFs formed, and hollow and metal filled CNFs formed at 1013 K [53]. At low temperatures (773–873 K), the catalyst particles are polyhedral and rigid. At high temperatures (>973 K), metal particles are in quasi-liquid state with pear or elongated shape, and hollow CNFs are generated [53]. In a recent work, Li et al. [158] examined the composition deviation of the metal particle tips associated with the CNFs after MCD reaction with a Ni–Cu/Al_2O_3 catalyst. The interesting results are obtained in Fig. 7. The images A–C show the fibers formed during a constant-temperature reaction (CTR) at 816 K. The metal particles are polyhedral and their sizes are in the range of 20–95 nm, bigger than the diameter of the carbon nanofibers grown from them. The angles of the carbon layers are all larger than 90°. Images of D–F show the CNFs formed at 1013 K, where the metal particles are pear-shaped with a long tail and sizes in the range 30–130 nm. The CNFs formed on these particles are obviously hollow and have outer diameters close to those of the metal particles. Images of G–I illustrate those formed with a pre-induction reaction (PIR) technique, in which the reaction temperature was held at 823 K for 10 min. After that the temperature was increased to 1013 K with a ramp of 10 K min^{-1}. The morphologies and the sizes of the CNFs formed are similar to those formed during constant temperature reactions (CTR) at 816 K. However, the shapes of the metal particles are different. Some of them have the features of the particles in the CTR mode at 816 K, but with a smoother surface. The others are more pear-shaped, but their tails are not as sharp as those formed in CTR at 1013 K. The shapes of the metal particle show the shift from rigid polyhedron to soft quasi-liquid along with the increase of the reaction temperature. The CNFs formed in the PIR process, possess both the features of high temperature mode and those of the low temperature one. The table in Fig. 7 shows the corresponding Ni/Cu ratio of the metal tip associated with the carbon fiber measured with an EDX technique. It is also interesting to note that the composition of the metal tips after reaction at a specific condition deviates in quite a large range, due to the fact that the metal particles are reduced from mixed oxides and have distributions of chemical composition and particle size.

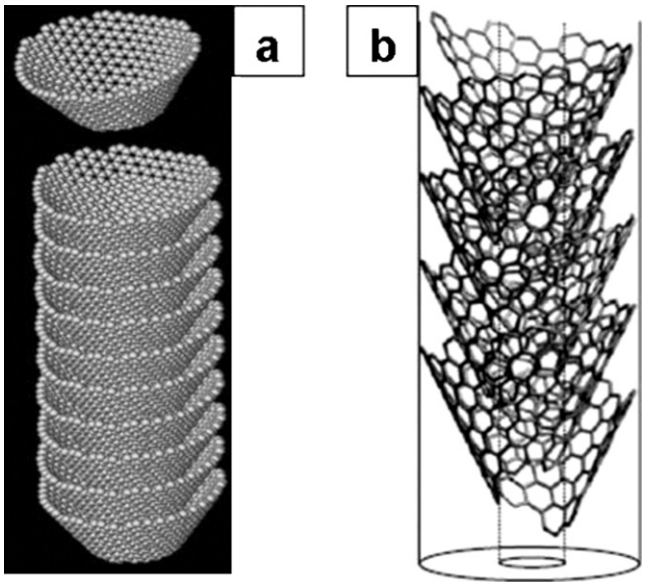

Fig. 8. Sketches for the two possible models account for the herringbone texture of nanotubes. (A) Cup-stack model, each cup is made of an independent carbon sheet. (B) Helical model, the fiber forms with one continues carbon sheet. Reprinted from [155] with permission of the Royal Chemical Society.

Fishbone (or herringbone) type CNFs form on Ni-based catalyst with a CH_4 and H_2 mixed gas feed at a comparatively low temperature [146,168]. Two structural models have been proposed for fishbone-type CNFs, i.e. cup-stack and helical texture models, see Fig. 8. However, these two models cannot be resolved by TEM images [155]. The cup-stack model explains the carbon formed as parallel bowl-shaped graphene sheets, while the helical model describes that as one sheet forming continuous graphite layers. Monthioux et al. [155] favored the cup-stack model because they observed that the CNF samples are easily fragmented by a low shearing stress developed during grinding. The non-continuous structure is also indicated by the non-uniform growth rate and the jump of the metal particles observed with an *in situ* TEM technique [154].

Bamboo-shaped CNFs were obtained in MCD reaction in quite a number of reported works [147–149,156,169–173]. In the work of Li and coworkers [147,148] typical bamboo-shaped CNFs with well-regular caves and fully developed carbon knot were obtained. They found that, uniform bamboo-shaped CNFs are generated with a feed of CH_4/H_2 (1/2 vol. ratio) on a Ni–Cu/Al_2O_3 catalyst at 993–1043 K [148]. Saito [174] proposed the existence of the jump movement of the metal particle and the driving force from carbon layer growth, presented in Fig. 9. Based on the observations of the particular morphology of the bamboo-shaped CNFs and the properties of metal particles, Chen et al. [148] proposed a growth

Fig. 9. Schematic diagram of the growth of bamboo-shape CNF. Saito remarked that "It is not clear whether the Ni particle at the tip was liquid or solid during the growth of the tube. We infer that the cone-shaped Ni was always at the tip and it was absorbing carbon vapor. The dissolved carbon diffused into the bottom of the Ni needle, and carbon segregated as graphite at the bottom and the side of the needle. After graphitic layers (about 20 layers) were formed, the Ni particle probably jumped out of the graphitic sheath to the top of the tube. The motive force of pushing out the Ni needle may be a stress accumulated in the graphitic sheath due to the segregation of carbon from the inside of the sheath".
Reprinted from [174] with permission of Elsevier Science Publishers B.V.

mechanism in which two kinds of movement of the metal particle are involved for the formation of bamboo-shaped CNTs. The first is a smooth movement, driven by the insertion of new carbon layers at the carbon–metal interface, leading to the formation of a continuous and uniform wall and cave. The second is the jump of the metal particle and is possible only when the metal particle is in a quasi-liquid state, and the molten metal has a low wetting of the graphene surface. During the formation of the new carbon lay-

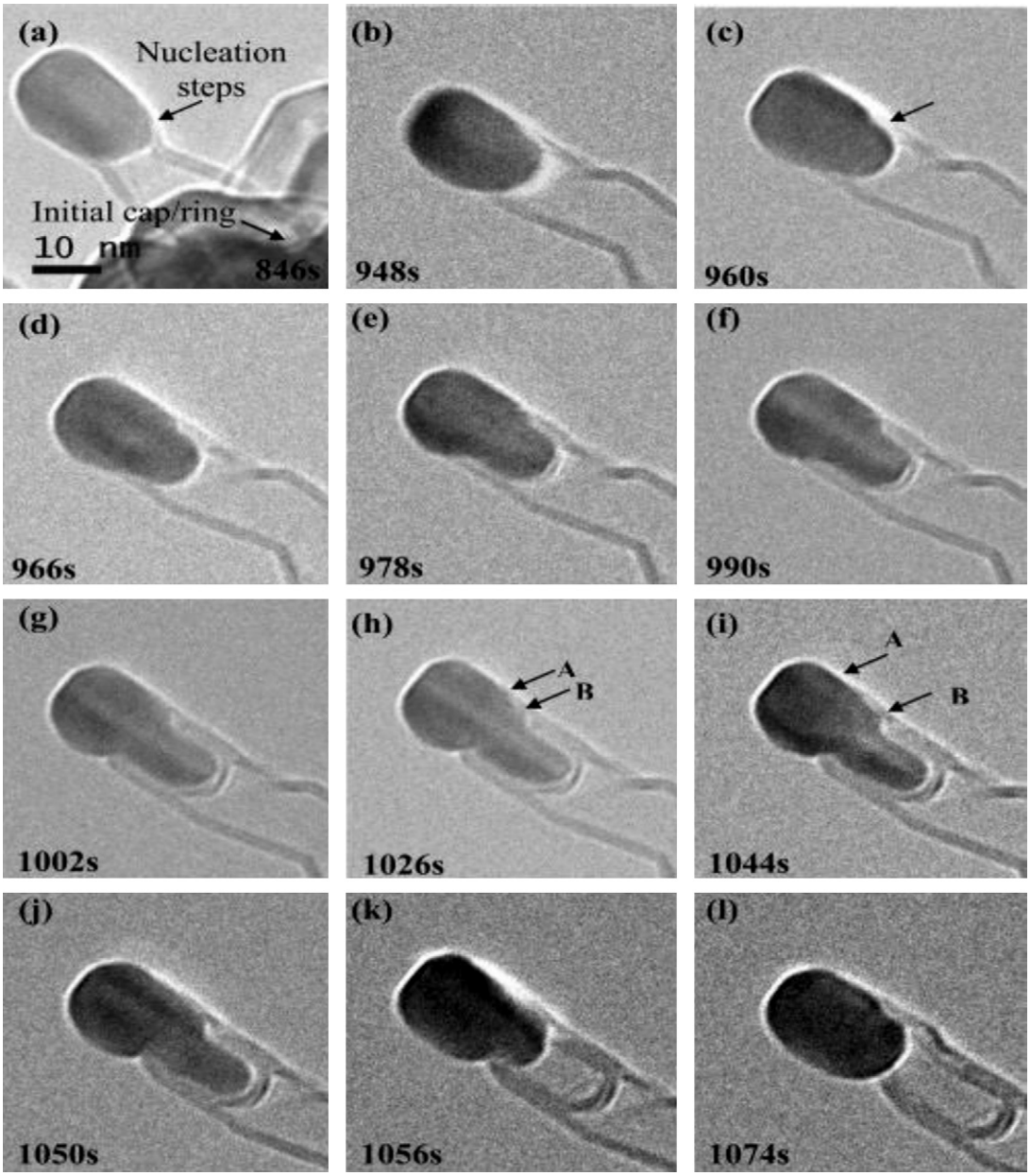

Fig. 10. A sequence of *in situ* TEM images showing the growth of a bamboo-like carbon nanotube (BCNT) from C_2H_2 catalyzed by a Ni particle at 923 K. During BCNT growth, the shape of the catalyst particle changes constantly but remains metallic and crystalline. Graphene sheets (bamboo knots) within the nanotube preferentially nucleate on the multistep Ni-graphite edges at the point where the graphene joins the catalyst particle, where it is stabilized by both the graphene walls and the Ni catalyst surface.
Reprinted from [171] with permission of the American Chemical Society.

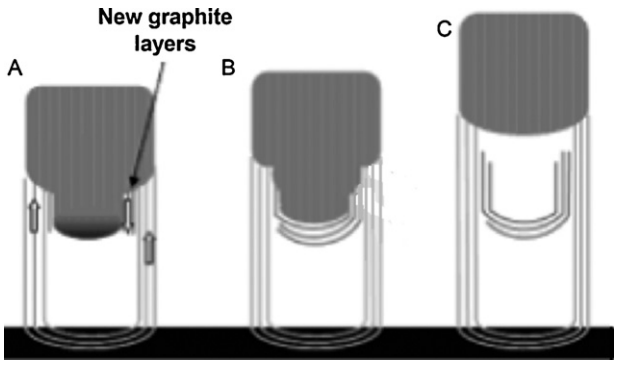

Fig. 11. Schematic diagram showing (A) the nucleation of a partial bamboo-knot graphite sheet at the graphene wall-catalyst junction; (B) the growth of the inner wall around the bottom of the Ni catalyst particle as adatoms are added to the inner wall edges through diffusion along the graphene–Ni interface; (C) subsequent formation of a hemispherical cap around the bottom of the catalyst particle (arrows indicate the direction of movement of the graphite relative to the Nigraphite step edges).
Reprinted from [171] with permission of the American Chemical Society.

ers, a depressing force is exerted on the metal particle towards its axis and growing direction. This stress accumulates as the insertion continues. When the stress is larger than the combination force of carbon and metal, a jump of the metal particle happens. This mechanism is clearer than the earlier one proposed by Saito [174], in which they supposed the periodical jumping of the metal particle. Zhang et al. [149] investigated the growth of bamboo-shaped CNFs and suggested that the metal particle is first sucked into the hollow fiber under the capillary force. Then the area of the metal surface exposed in the reactant atmosphere is decreased which decreases the transportation of carbon through the catalyst particle. In this condition, its surface tension increases with decreasing the carbon content while the capillary effect decreases due to the increase of the inner diameter of the cave. When the surface tension of the metal particle is larger than the capillary force, the sucked metal particle is pulled back. Bamboo-shaped CNF thus forms with these circles. Lin et al. [171] observed the growth of bamboo-shaped CNFs with an *in situ* TEM. A sequence of *in situ* TEM images is shown in Fig. 10. They noticed that after the initial nucleation, a small tail forms at the bottom of the metal particle and the partial bamboo-knot graphite sheet forms at the junction of the graphene wall and the tail of the metal particle. Thereafter, a hemispherical cap forms around the bottom of the metal particle. Consequently, the metal particle and the graphite cap are separated as shown in Fig. 11. However, the bamboo-shaped CNFs formed in their work has very irregular knot and is not the same as those reported previously. Holmes and coworkers [172,173] observed the change of the particle shape from spherical to elliptical in MgO-supported Pd and Cu catalysts. A "plastic" phase of the catalyst particles which is elliptical and elongated is observed after the growth of bamboo-shaped CNFs, which is similar to that found by Lin et al. [171]. They also believed that the surface energy of a catalytic nanoparticle is lowered by the formation of a graphene cap. As the carbon layer grows, the nanoparticle deforms in order to maintain the stability until such a point where the energy cost from being elongated is more than the energy gained from being bound to the graphene layer. The chamber forming process repeats this way.

SWCNTs and MWCNTs have been synthesized via MCD reaction [110,141,142,175–177]. As the simplest CNT, the growth mechanism of SWCNTs has been the subject of intensive research in the literature, and it has been often explained with similar models which are originally proposed for CNF growth. However, SWCNT growth is more specifically related to the size effect of the metal particle in nanometer scale [178]. Nano-sized metal particles exhibit a high surface energy, which facilitates the assembling of a graphene cap and eases the formation of a SWCNT. The hemifullerene cap formed on the partially carbon-coated particle lifts off and additional carbon atoms are continuously added to the edge of the cap, forming a hollow tube with constant diameter which grows away from the particle [179]. As the growth of SWCNT, the total surface energy diminishes since the formed basal planes of graphite have an extremely low surface energy [180]. Based on the result of molecular dynamic simulation of the SWCNT formation, Shibuta and Maruyama [181] reached a conclusion that carbon atoms are first absorbed into the metal cluster until saturation to make a hexagonal network of carbons on the surface of the cluster. Further supply of carbon atoms leads to a separation of the carbon network from the metal surface itself or from a hump on the surface of the metal cluster, which in turn results in carbon cap formation. As a consequence, carbon atoms inside the supersaturated nickel cluster gradually stick at the edge of the tube and thus lift up the carbon-shell. This process can be regarded as an initial stage of the growth process of SWCNT and is consistent with the Yarmulke mechanism [180].

Control of the diameter and structure of CNTs can be realized by manipulating the metal particles and reaction conditions. Chai et al. [182] examined the effect of calcination temperature of a CoO–MoO/Al_2O_3 catalyst on the formed metal particle size, which in turn, influences the uniformity of the CNT diameter. They obtained CNTs with diameters in the range of 7.6–21.8 nm. Kuo et al. [183] investigated the factors influencing the diameter of CNTs using a fractional factorial experimental design method, and it is found that the reaction temperature, methane flow rate, and pressure are the key factors for controlling the diameter of CNTs. Kang et al. [184] synthesized SWCNTs and doubled-walled carbon nanotubes (DWCNTs) over a Fe–Mo/MgO catalyst and they found that the proportion of DWCNTs increased with the increase of the reaction temperature which may be due to the agglomeration of the catalyst particles at a relatively high temperature. Hornyak et al. [185] demonstrated the existence of a temperature window for the effective growth of SWCNTs via MCD reaction. Their results showed that a low temperature (953–1073 K) is preferred for the growth of high-yield SWCNTs. In this temperature range, the growth rate of SWCNTs is high and the deposition of amorphous carbon is hindered, while at high temperatures (>1073 K) the deposition of amorphous carbon becomes competitive.

2.3. Methane activation on metal surface

Because of the long term commercial interest on steam reforming of methane, methane activation on transition metals has been the topic of a large amount of the literature. The dissociative adsorption of methane is considered as the rate-determining step in MCD and steam reforming reactions [186–188]. Several excellent reviews have been published on this topic [189,190]. The interaction of methane and transition metal surface has been investigated intensively with well defined surfaces under ultra-high vacuum (UHV). Much information has been obtained with either bulb [191–193] or molecular beam techniques [194–199]. Various instruments, such as X-ray photoelectron spectroscopy (XPS), Auger electron spectroscopy (AES), electron energy loss spectroscopy (EELS), infrared spectroscopy (IR), temperature programmed desorption (TPD), and low-energy electron diffraction (LEED) have been employed for characterizing the metal surface [191–198,200–202]. It is beyond the scope of this review to go into experimental details. Here we focus only on the introduction of the fundamental knowledge obtained on this topic.

The dissociation of methane on metal surface is considered to follow a pathway of a precursor mediated mechanism

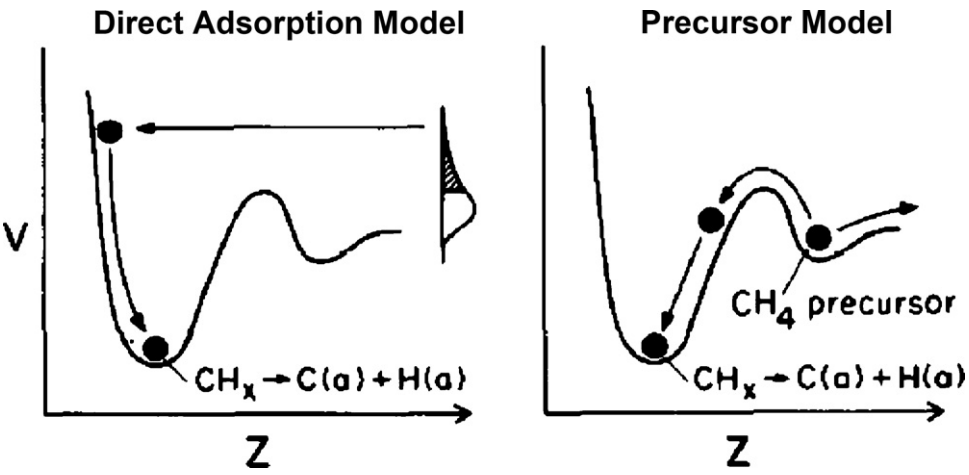

Fig. 12. Schematic diagrams of the two pathways of methane activation on metal surfaces, direct dissociation mechanism (DDM) and precursor mediated mechanism (PMM). Reprinted from [193] with permission of Elsevier Science Publishers, B.V.

(PMM) [192,202] or a direct dissociation mechanism (DDM) [193,196,198,201,203], as presented in Fig. 12. In the PMM, methane molecule is adsorbed and transformed into an intermediate state, which can either desorb from the surface or undergo further dissociation. For the DDM, methane dissociates directly without forming any intermediate state. Table 2 lists some literature reporting experimental results of methane activation. Interaction of methane and Ni (1 1 1) surface was examined by Hanley et al. [193] with bulb experiments. They found that the sticking coefficient is largely dependent on the pressure in the range of 0.02–1.6 mbar, which indicates a DDM mechanism. Lee et al. [196] derived similar results on Ni (1 1 1) with molecular beam method. However, there are some controversies on the behavior of methane on Ni (1 0 0) surface. Chorkendorff et al. [201] and Jiang et al. [202] proposed that methane dissociative adsorption proceeds with a DDM mechanism. However, Campbell et al. [203] demonstrated that the sticking coefficient is only weakly dependent on the pressure, and therefore they concluded that it is rather a PPM process.

The sticking coefficient and the activation energy of methane on metal surface are important information for understanding the interaction between the molecule and the surface, and they can be either experimentally or theoretically derived. Beebe et al. [192] showed with bulb experiment that Ni (1 1 0) is the most reactive surface and Ni (1 1 1) the least reactive, as shown in Fig. 13. Yang and Chen [162], based on the TEM/SAD characterization and extended Hückel molecular orbital calculations, suggested that Ni (1 0 0) and Ni (1 1 0) surfaces are the gas/metal interfaces, while Ni (1 1 1) and Ni (3 1 1) surfaces form graphite/metal interfaces. Beebe et al. [192] gave similar activation energies (53–56 kJ/mol) on Ni (1 1 0) and Ni (1 1 1), but approximately half of this value for Ni (1 0 0). Egeberg et al. [204] measured the activation energy for the dissociative adsorption of CH_4 on Ni (1 1 1) and derived a value of 74 ± 10 kJ/mol. For Ni (1 0 0) surface, Nielsen et al. [198] observed an activation energy value 59 kJ/mol for CH_4 dissociative adsorption and Xing et al. [205] got an activation energy of 57.8 kJ/mol for the same process, which is close to that Beebe et al. reported [192].

Some activation energy data on low index faces based on simulation results have been reported. In the first-principle calculations, Ni (1 0 0) surface has either been represented as a small cluster or a periodic slab. Swang et al. [206] performed *ab initio* quantum chemistry calculation using a cluster model and obtained an activation energy of CH_4 chemisorption on Ni (1 0 0) surface as 67 ± 4 kJ/mol. In another early work, Bengaard et al. [207] conducted density functional theory (DFT) calculation in which the slab was kept rigid to reduce computational effort and gained an

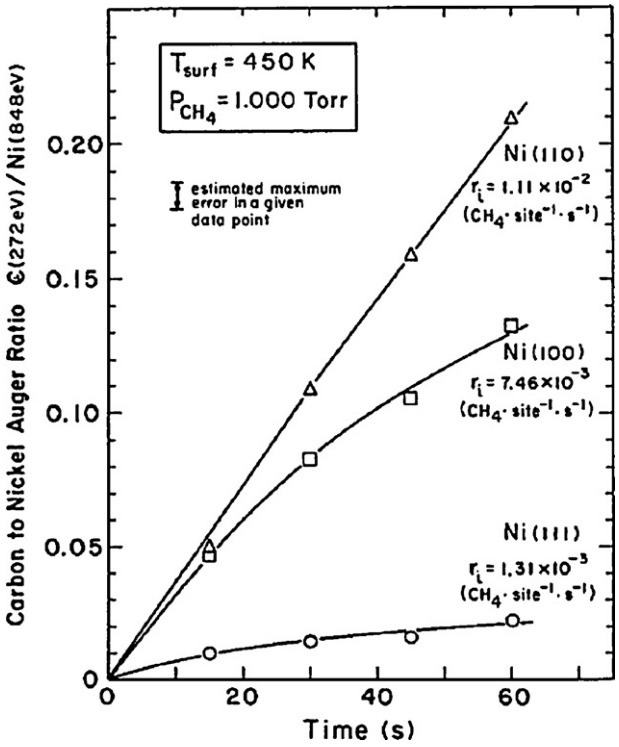

Fig. 13. Methane decomposition kinetics on the low index planes of nickel single crystal surfaces.
Reprinted from [192] with permission of American Institute of Physics.

energy barrier of 115 kJ/mol. Recently, Lai et al. [208] got activation energies of 62 kJ/mol without spin-polarization and 70 kJ/mol with spin-polarization, respectively. Henkelman et al. [209] obtained an activation energy 79 kJ/mol for the CH_4 dissociation on Ni (1 1 1) surface with representing the surface as a five-layered slab and with DFT calculation taking spin-polarization into consideration. According to the DFT calculations of Watwe et al. [210], the dissociation of methane on Ni (1 1 1) has a barrier of 127 kJ/mol without considering the spin-polarization of the electrons. Zhu et al. [211] considered the zero-point energy and dispersion energy corrections in the first-principle calculation and they obtained the barrier of methane activation on Ni (1 0 0) surface as 59–60 kJ/mol.

The long term continued research effort on the adsorption of methane on Ni single crystal surface has accumulated a large

Table 2
Summary of methane activation on single crystal Ni surfaces.

Surface	Activation energy (kJ/mol)	Sticking coefficient	Experiment methods	Result description	Reference
Ni (1 0 0)	0	-5×10^{-9} (474–563 K)	Bulb experiment LEED AES	The sticking coefficient is initially 5×10^{-9} and does not depend on the temperature in the range 474–563 K. Diffusion of carbon from a surface carbide into the bulk is the limiting step on Ni (1 0 0)	Schouten et al. [191]
	26.8 ± 4.6	6×10^{-8} (500 K)	Bulb experiment AES TPD	PPM mechanism A large (factor of 20) kinetic isotope effect for CH_4 vs. CD_4 was observed for Ni (1 0 0). The sticking coefficient depends on the temperature in the range 450–600 K. No significant pressure dependence was observed in the pressure range of 1–3 mbar	Beebe et al. [192]
	52 ± 1	10^{-7} (550 K) 1.1×10^{-9} (400 K)	Bulb experiment XPS	DDM mechanism Initial sticking coefficient depends on the temperature in the range of 400–550 K	Chorkendorff et al. [201]
		$3–5 \times 10^{-8}$ (500 K)	Bulb experiment AES, LEED, TPD	PPM mechanism Sticking coefficient was measured as a function of pressure in a range from 0.07 to 1.3 mbar and only a weak increase in the sticking coefficient was observed in this pressure regime	Campbell et al. [202]
	–	–	Molecular beam and bulb experiments	DDM mechanism A dramatic activation due to translational energy as well as vibrational excitation is observed. An isotope effect of approximately a factor 5–10 is observed and CH_4 is more reactive than CD_4 at the same translational energy	Holmblad et al. [197]
	59 ± 1.5	1.7×10^{-9} (400 K)	Molecular beam and bulb experiments	DDM mechanism The dissociative chemisorption of methane on Ni (1 0 0) was proved to be a DDM mechanism both under isothermal as well as non-equilibrium conditions	Nielsen et al. [198]
Ni (1 1 0)	88.2 ± 12.6	$0.14–3.0 \times 10^{-8}$ (473 and 579 K)	Bulb experiment AES, LEED and ellipsometry	In the temperature range 473–579 K, the coverage versus exposure curves show an induction effect at low coverage followed by an almost linear increase up to a saturation coverage of about l/3 monolayer of carbon	Schouten et al. [200]
	88	10^{-8}	Bulb experiment LEED AES	Diffusion of carbon from a surface carbide into the bulk is the limiting stage on Ni (1 1 0)	Schouten et al. [191]
	55.68 ± 6.28	1.6×10^{-7} (500 K)	Bulb experiment	PPM mechanism No kinetic isotope effect for CH_4 vs. CD_4 was observed for Ni (1 1 0) surface and no significant pressure dependence was observed in the pressure range of 1–3 mbar. The sticking coefficient depends on the temperature in the range 450–600 K	Beebe et al. [192]
Ni (1 1 1)	–	$\leq 10^{-1}$ (523–618 K)	Bulb experiment LEED AES	Methane does not interact with Ni (1 1 1) No carbon deposition could be detected after 5 h exposure to methane at a pressure of 10^{-2} Torr in the temperature range of 523–618 K	Schouten et al. [191]
	68.1	–	Molecular beam experiment concomitant with high-resolution electron-energy spectroscopy (HREELS)	DDM mechanism Surface temperature had no influence on the dependence of the sticking coefficient with translational energy. The dissociative chemisorption of CD_4 exhibits a large kinetic isotope effect	Lee et al. [196]
	52.9 ± 5	1.2×10^{-8} (500 K)	Bulb experiment	PPM mechanism No significant pressure dependence was observed in the pressure range of 1–3 mbar. The sticking coefficient depends on the temperature in the range 450–600 K	Beebe et al. [192]
	–	4×10^{-8} (600 K)	Bulb experiment	DDM mechanism The sticking coefficient was significantly dependent on the pressure in the regime from 0.02 to 1.6 mbar. The activation of CH_4 via dissociation on Ni (1 1 1) proceeds with a direct process	Hanley et al. [193]

amount of fundamental data and this leads to a better understanding of methane dissociation. However, it should be noted that these model examinations do not represent the real working status of the transition metal catalysts which are much more complex. Catalytic reaction experiments [212,213] over SiO_2 and Al_2O_3 supported Ru nanoparticles yield apparent sticking coefficient 10^2–10^3 times lower than those reported by Wu and Goodman [214] and Egeberg et al. [204] for CH_4 on Ru (0 0 0 1) crystal surface. Carstens and Bell [212] measured an activation energy 27 ± 2 kJ/mol for dissociative sticking of CH_4 on Ru particle with 6 nm average diameter

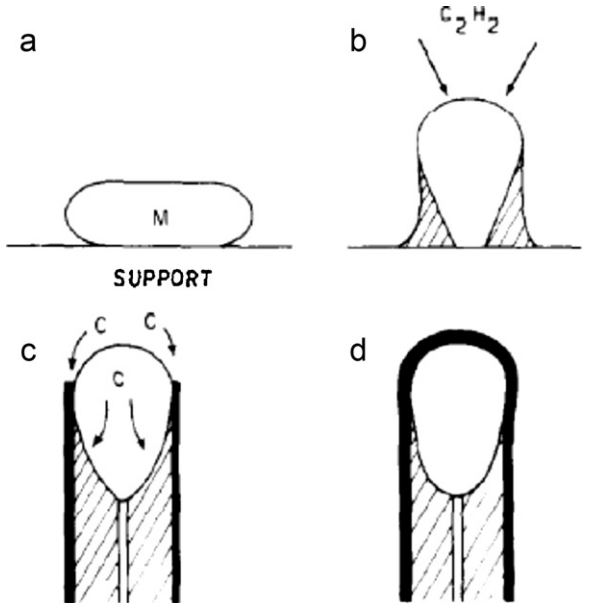

Fig. 14. The growth of carbon nanofibers dominated by bulk diffusion. Adsorption of carbon species induces the reform of the metal particle. The carbon atoms diffuse mainly through the bulk phase of the metal and deposit as the carbon fiber in the other side of the particle.
Reprinted from [137] with permission of Elsevier Science Publishers, B.V.

supported on SiO_2 over a 473–673 K temperature range, whereas Wei and Iglesia [213] measured activation energy as 99 kJ/mol for Ru particles with 2.5 nm average diameter supported on Al_2O_3 in 823–1023 K. Furthermore, they performed kinetic and isotopic tracer and exchange experiments and found that the rate of forward reaction increases with increasing Ru dispersion [213]. This suggests that the coordinatively unsaturated surface atoms prevalent in small crystallites are significantly more active than those in the low-index planes predominately exposed on large crystallites.

2.4. Carbon atom migration

MCD is complex because it involves the formation of solid carbon, viz. the carbon atom dissociated from methane has to undergo a diffusion and reaction process to form graphite layers. Presland and Warker suggested [215] a solution and precipitation model for the formation of graphite over metals. Baker et al. [137] described bulk diffusion mechanism of CNF growth in some detail as in Fig. 14. Hydrocarbon molecule dissociates to carbon atoms on particular crystal plane and they subsequently diffuse through the nickel particle to the other side and form a CNF. They used the earliest *in situ* TEM technique to observe the temperature dependence of the CNF growth rate, and determined the activation energy of ethylene decomposition on different metals [138]. They found that the measured activation energy is very close to the diffusion activation energy of carbon atoms within the bulk metal phase. This led them to conclude that this phenomenon is an evidence of carbon bulk diffusion mechanism. Bernardo and Lobo [118] used a single crystal Ni foil as catalyst and examined the mechanism of carbon diffusion process. A series of Ni foils with 0.1 mm thickness treated under various pre-coating conditions were used for acetylene catalytic decomposition. No reaction was observed on the Ni foil pre-coated with carbon at both sides. Carbon formed on the Ni foil pre-coated with carbon on one side, and it was found that the growth of carbon took place on the coated side while the uncoated side remained clean. Since the coated side has no activity for C_2H_2 catalytic decomposition, it is obvious that carbon atoms migrate through the nickel crystal from the uncoated side to the coated side during the reaction. This is a strong evidence to support the bulk diffusion mechanism. Avdeeva et al. [216] investigated MCD on a Ni-based catalyst using *in situ* XRD. They tried to correlate the change of Ni (2 2 0) diffraction peak during the experiment with carbon atom diffusion in the Ni crystal lattice. They showed that during the first 8 min, the Ni (2 2 0) diffraction peak shifted to a smaller angle by 0.3° (2θ). They attributed this phenomenon to the carbon dissolution in metal bulk phase with a concentration of 2 at.%. They found no nickel carbide phase formed during the reaction. Yoshida et al. [217] observed the nucleation and growth process of CNTs from iron carbide (Fe_3C) nanoparticles in chemical vapor deposition (CVD) with C_2H_2 by *in situ* environmental TEM. Graphitic networks are formed on the fluctuating iron carbide nanoparticles, and subsequently CNTs are expelled from them. They suggested that carbon atoms diffuse through the bulk of iron carbide nanoparticles during the growth of CNTs.

The bulk diffusion mechanism is also supported by a relationship between the solubility of carbon and the ability to catalyze the CNTs formation of the transition metals. Holstein [218] explained that Fe, Co, and Ni have good carbon solubility and high activity, while Cu, Au, and Ag have low carbon solubility and have no activity for CNF growth. Deck and Vecchio [219] confirmed this concept with testing various transition metals and found that Cr, Mn, Zn, Cd, T, Zr, La, Cu, V and Gd do not catalyze the growth of CNTs. They examined the phase diagrams of carbon and various metals and postulated that carbon diffusivity has some correlation with its solubility. Snoeck et al. [166,186] verified the concept with thermodynamic analysis and kinetic study and agreed that the carbon atoms dissolve and diffuse in nickel particle. They extended this mechanism to explain the different morphotypes of CNT grown at different temperatures. They proposed that at low temperatures, the rate of nucleation is lower than that of diffusion, and the nucleation is uniform over the whole metal/carbon interface. Therefore, full filaments without hollow channels will form. At high temperatures, nucleation is instantaneously and intrinsically much faster than the rate of diffusion and no driving force is present for nucleation at places with long diffusion path. Therefore, hollow filaments are obtained, as shown in Fig. 6. Some other research groups observed the same phenomenon [165,167].

Presland and Warker [215] reported that surface diffusion of atomic carbon species might happen and form graphite layers over metal surface. Baird et al. [144] proposed that the dissociated carbon atoms diffuse along the surface of metal particles to the other side to form carbon filament. Oberlin et al. [107] gave a similar mechanism, as illustrated in Fig. 15. In recent years, several groups investigated the MCD with the aid of computer simulation and supported this mechanism [154,220–222]. Hofmann et al. [220] performed MCD in a plasma-enhanced reactor and obtained activation energy in 22–39 kJ/mol. They simulated the carbon diffusion process with *ab initio* plane wave density functional calculations and showed a low activation energy of 39 kJ/mol for carbon diffusion on Ni and Co (1 1 1) planes, which is much lower than that of bulk diffusion (~150 kJ/mol). Helveg and coworkers [154,163,223,224] also obtained a lower activation energy for surface diffusion than that from bulk diffusion with density functional calculations. This led them to suggest carbon atoms diffuse along graphene–Ni interface. Pinilla et al. [225] found that the structural properties of the Ni particle do not change after carbon deposition. They believed that the atomic carbon diffuses on the Ni surface instead of through the Ni bulk.

Different from the bulk and surface diffusion mechanisms, carbide sometimes behaves as the intermediate during the reaction. Buyanov and coworkers [226,227] proposed a metal carbide mechanism and suggested that surface carbide-like compound is the reaction intermediate. Alstrup and coworkers [228,229] assumed that a few atom layers of metastable metal carbide form and decompose to form carbon atoms and stable metal or metal carbides.

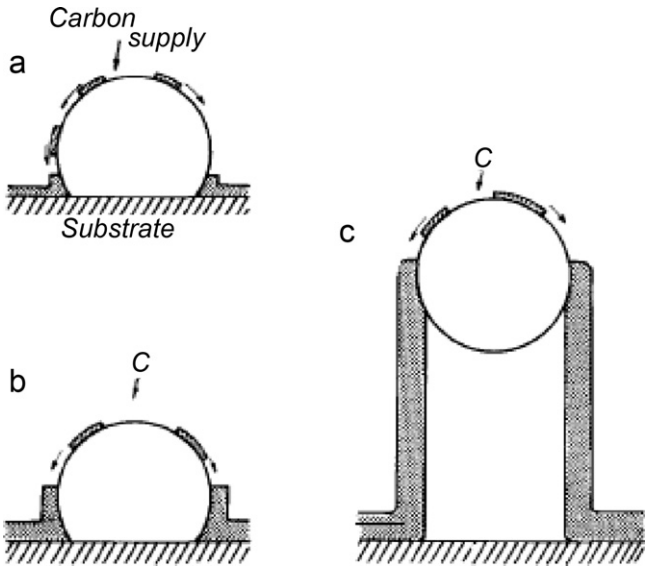

Fig. 15. Schematic illustration of carbon nanofibers growth with surface diffusion mechanism. At the beginning small "liquid-like" droplets of iron form. On that clean surface begins to nucleate an association of metal and hydrocarbons which diffuses on the surface and dissociates at the contact angle between the droplet and the substrate. A carbon shell is then produced. New hydrocarbon species dissociate on its edges and the carbon layers develop by lateral growth following the external surface of the catalyst (A and B). Such a lateral growth exerts a force strong enough to lift up the catalyst particle above the surface of the substrate (C).
Reprinted from [107] with permission of Elsevier Science Publishers, B.V.

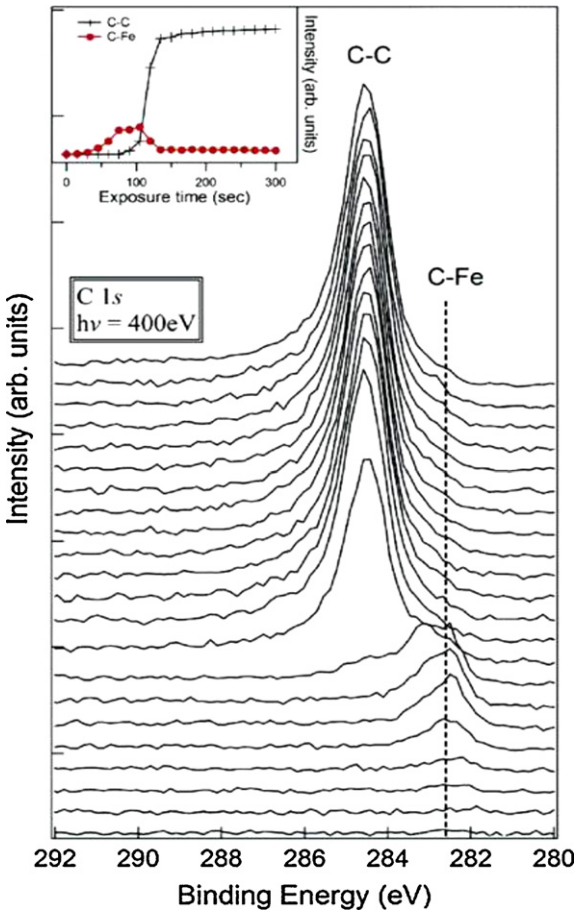

Fig. 16. Time-resolved evolution of C 1s core level during Fe exposure to 2×10^{-7} mbar (background pressure) C_2H_2 at 853 K. Insets show the time-evolution of the chemisorbed (dots) and graphitic (crosses) carbon peaks.
Reprinted from [234] with permission of the American Chemical Society.

The metastable surface carbide maintains a constant concentration through formation and decomposition on the front surface. The carbon atoms diffuse through the catalyst particle and form CNF on the other side of the surface. They postulated that, when its thickness exceeds a certain critical value, metastable metal carbide decomposes into a stable θ-Fe_3C and graphite phases which leads to the encapsulation of the catalyst particle and prevents the catalyst from contacting with the hydrocarbon molecules, resulting in deactivation. Geus and coworkers [230–232] measured the magnetic susceptibility during the decomposition of methane and disproportionation of carbon monoxide on the supported nickel and iron catalysts and suggested a metal carbide intermediate growth mechanism. They found that the presence of substoichiometric nickel carbide during steady-state growth and high carbide content is necessary for the nucleation of graphite layers. For iron catalyst the hexagonal ε-Fe_2C or ε'-$Fe_{2-n}C$ is likely to be the intermediate in filament growth. Narkiewicz et al. [233] measured the apparent activation energy of the MCD reaction and proved the iron carbide formation. Their results showed that both the activation energies of the two processes are similar and equal to 150 kJ/mol in a temperature range of 773–873 K under atmospheric pressure. They proposed that iron carbide is involved in the formation of carbon from methane. Yoshida et al. [217] performed an atomic-scale *in situ* observation of Fe catalyzed CVD growth of CNTs, and showed that iron carbide (Fe_3C) nanoparticle acts as catalyst and its morphology changes along with the growth of the CNT.

However, it is likely that the mechanism of MCD differ depending on various metal catalysts. For Fe catalysts, surface and bulk iron carbides have previously been observed. Recently, Hofmann et al. [234] studied the growth process of CNTs on a Fe catalyst with an *in situ* TEM and a time-resolved XPS techniques. During the initial stage of the reaction (~30 s), the formation of Fe–C bond is detected. As the reaction proceeds, the Fe–C is weakened and disappeared, as shown in Fig. 16. This is attributed to the formation of the C–C bond on the surface. The presence of bulk Fe_3C has been verified by a recent study with *in situ* XRD [235]. These results support the carbide intermediate mechanism. For the Ni catalyst, no nickel carbide is detected with *in situ* XRD [216]. In another study with *in situ* TEM, the electron diffraction also indicates the absence of bulk Ni_3C during CNT growth [236].

CNF and CNT growth are complex process. The diffusion of carbon atom is difficult to observe and measure accurately. Therefore, simulation turns to be a suitable technique. However, most established models are based on infinite surface or metal clusters which are significantly different from the real metal nanoparticles. MCD is a structure sensitive reaction and the metal particle size is important [237]. Abundant experimental results suggest that bulk diffusion of carbon atoms is involved in MCD reaction. However, it is still uncertain whether it is the dominant pathway for the migration of carbon atoms. During the induction process of MCD reaction, the carbon atoms can dissolve into metal crystal lattice or form metal carbide. However, as the reaction proceeds, it is probable that the growth of CNF and CNT mostly takes place through surface diffusion of carbon atoms due to the lower energy barrier of surface diffusion than bulk diffusion.

2.5. The driving force

For the bulk diffusion mechanism, the driving force for carbon diffusion through metal particle was attributed either to a temperature gradient [137,162,238], or a concentration gradient [139,231]. Baker and coworkers [137,138] found that MCD does not take place while the decomposition of the other hydrocarbons happens. They attributed this as due to the failure of establishing a temperature

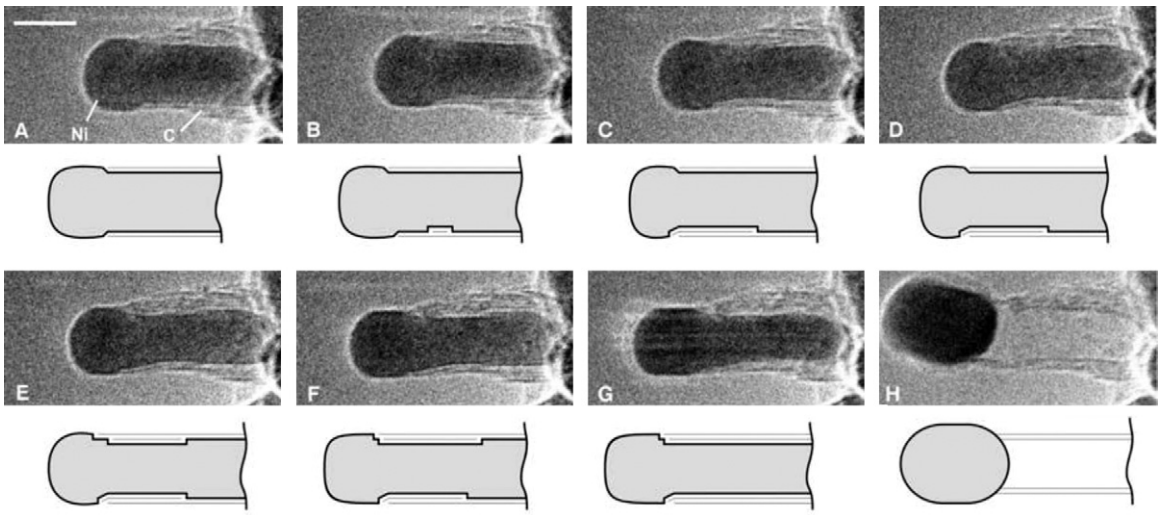

Fig. 17. Image sequence of a growing carbon nanofiber. Images A–H illustrate the elongation/contraction process. Drawings are included to guide the eye in locating the positions of mono-atomic Ni step edges at the C–Ni interface. The images are acquired *in situ* with CH_4:H_2 1:1 at a total pressure of 2.1 mbar with the sample heated to 809 K. All images are obtained with a rate of 2 frames s^{-1}. Scale bar in A, 5 nm.
Reprinted from [154] with permission of the Nature Publishing Group.

gradient in metal particle because that MCD reaction is endothermic. Meanwhile, Audier et al. [239,240] showed later that MCD took place and formed CNFs on the same catalyst at a higher temperature and there is no change in thermodynamic trend. Cale and coworkers [241,242] thought that no temperature gradient exists in the metal particle and the support phase. Calculations by Tibbetts et al. [243] indicated that the temperature gradient is smaller than 10^{-5} K, which cannot ensure the observed growth rate of carbon filaments. Holstein and Boudart [244] also proved with theoretical reasoning that the temperature gradient driving mechanism is invalid.

Rostrup-Nielsen and Trimm [139] demonstrated that carbon solubility at the gas/metal interface is different compared with the metal/carbon interface and thought that the concentration gradient mechanism is more reliable. Holstein [218] showed that the diffusion model and experimental results are consistent only with a mechanism in which the driving force for carbon diffusion is an isothermal carbon concentration gradient. Snoeck et al. [166] proposed a detailed model coupling of the surface reactions, the segregation process, and the diffusion of carbon through the nickel particle. The results showed that the driving force for carbon diffusion and for the global process of carbon filament formation is the difference in solubility at the gas/metal interface and the carbon filament/metal interface. Tibbetts [245] proposed that during MCD the metal particle becomes supersaturated and the chemical potential gradient forming from the carbon concentration gradient causes carbon diffusion from the front face to the back face of the particle where precipitation takes place. Nevertheless, differing from the above arguments, Kock et al. [231] proposed that the driving force for bulk carbon diffusion is the gradient of the carbon content of the nonstoichiometric carbide, which decreases towards the metal–carbon interface.

2.6. The roles of metal particle

Several remarkable common features of catalytic grown CNFs have been observed with TEM technique. The metal particles are always located at the tip of growing CNF, and in most cases they are carried away from the support. The deactivated metal particles are always encapsulated by non-reactive graphene layers. In addition, after reaction the metal/carbon interfaces display good affinity of metal particle and the graphene layer in shape.

Several groups observed that the metal particles within the catalyst undergo agglomeration and reconstruction process during the induction period of reaction [147,154,163,223]. Li et al. [147] found that the metal particles enlarge after reaction and change in shape from semi-spherical to polyhedral-shaped after the reaction at 773 K. They postulated that the metal particles are reformed during the initial period. This phenomenon has also been confirmed by Helveg et al. [154].

Helveg et al. [154,163,223] employed an *in situ* HRTEM, examined the CNTs growth, and recorded the process with a camcorder. It shows that, during the initiation period, metal particle transforms into highly elongated shape and the graphene sheet grows along the graphene–Ni interface. Thereafter, the metal particle contracts quickly into a spherical shape and thus completes one growth period, as shown in Fig. 17. They suggested that monoatomic steps exist at the Ni surface and that a graphene sheet terminates at each of these steps, and such Ni step edges play as the site for the nucleation and growth of the graphene sheets, as illustrated in Fig. 18. The graphene layer starts growing as the Ni layer is induced. They also proposed that a Ni flux exists besides the carbon atom diffusion during the growth.

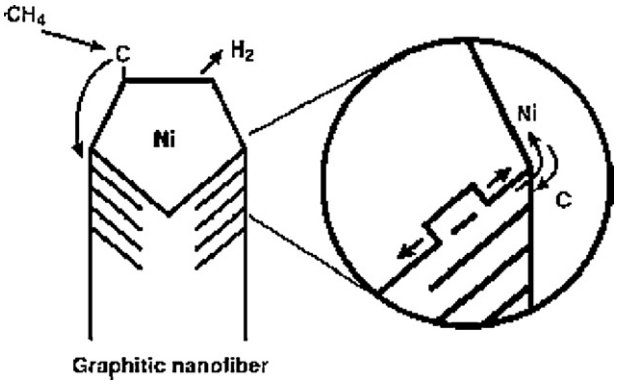

Fig. 18. Illustration of the growth mechanism for graphitic nanofibers formed by methane decomposition over nickel nanocrystals. The illustration highlights the surface transport of carbon and nickel atoms and the spontaneous Ni step-edge formation at the graphene–Ni interface.
Reprinted from [224] with permission of Elsevier Science Publishers, B.V.

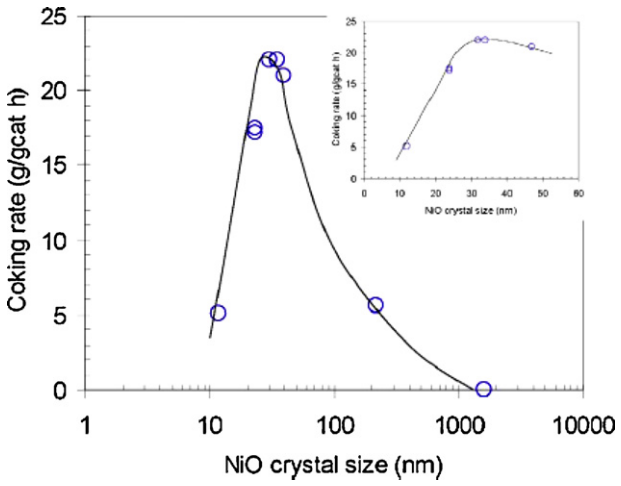

Fig. 19. Effects of NiO crystal size on the growth rate of CNF. Reaction conditions: T = 853 K, P_{tot} = 100 kPa, p_{CH_4} = 80 kPa, p_{H_2} = 5.5 kPa. Total flow: 50 ml/min. The horizontal axis should be Ni crystal size cording to the context of the original article.
Reprinted from [237] with permission of Elsevier Science Publishers, B.V.

Sharma and coworkers [234,246–252] also performed intensive *in situ* TEM observations. They reported that the growth of both straight and serpentine CNTs tends to proceed at non-uniform rates. They observed that the growth of CNTs includes two movements of the metal particle, i.e. a smooth movement leading to the formation of several graphite walls and a jump movement charged by the newly formed carbon layers. This was also confirmed by the work presented in [148]. Sharma et al. [250] reported also that the morphology of the CNTs is a dependent factor of reaction condition. With high temperature and low pressure, straight SWCNTs tend to form, while curved, zigzag and MWCNTs tend to form at lower temperature and higher pressure. They explained this result with the competition between the arrival rate of carbon atoms and the nucleation rate of CNTs [250].

It is well known that the catalyst performance in the MCD is highly dependent on the metal particle domain size. Beyond certain size range, being either too small or too big, metal particles will be inappropriate for CNFs growth. Chen et al. [237,253] obtained a variety of catalysts with different sized Ni particle by sintering cat-

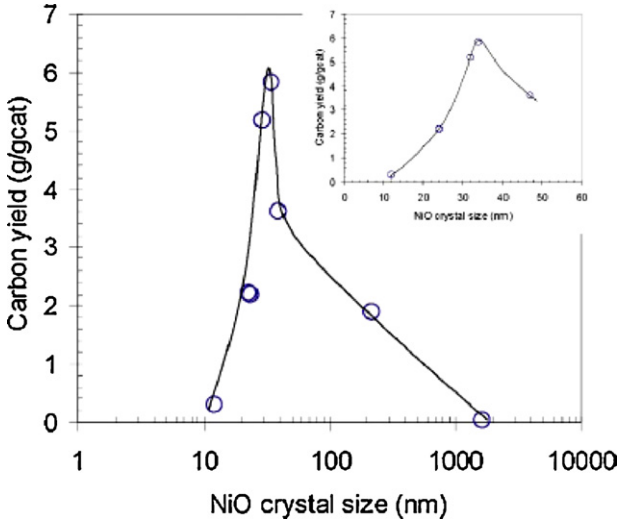

Fig. 20. Effects of NiO crystal size on the final carbon yield of CNF. Reaction conditions: T = 853 K, P_{tot} = 100 kPa, p_{CH_4} = 80 kPa, p_{H_2} = 5.5 kPa. Total flow: 50 ml/min. The horizontal axis should be Ni crystal size.
Reprinted from [237] with permission of Elsevier Science Publishers, B.V.

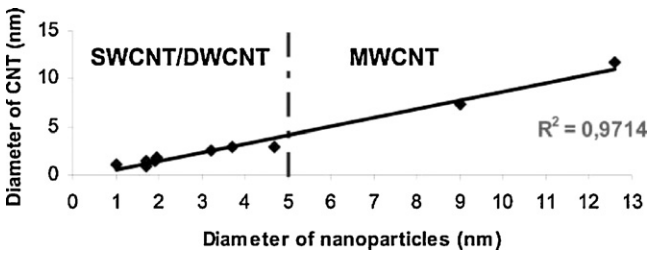

Fig. 21. Correlation between the size of the catalyst particle and the diameter of the carbon nanotubes. Typically, particle sizes of 2–5 nm are adapted to SWCNT growth, whereas with larger particles the number of DWCNT, TWCNT, and MWCNT increases. It is known that reducing to the nanometer scale the metallic particle diameter influences significantly the physicochemical properties of the material. As: (i) high dispersions are obtained that will enhance the catalytic activity with regard to the carbon source decomposition; (ii) carbon diffusion increases; and (iii) the melting point of the particle decreases, inducing a faster diffusion through the particle.
Reprinted from [263] with permission of Taylor & Francis Group, LLC.

alyst at different conditions and used them for MCD reaction, the major results are given in Figs. 19 and 20. Under their conditions the highest initial growth rate and yield of CNFs are obtained on a catalyst with an average particle size of 34 nm. The authors postulated that the larger particles resulted in a decrease of the active surface area, while the smaller particles led to a low activity due to high carbon concentration and a lower concentration gradient in nickel particles. Ermakova et al. [254,255] gave similar results for MCD on a Ni-based catalyst. They achieved highest carbon yield with an average nickel particle size in the range of 30–40 nm. Takenaka et al. [168] examined a Ni/SiO_2 catalyst in MCD reaction, and found that the catalyst with nickel particle diameters in between 60 nm and 100 nm maintained longer active time, while in the work of Pinilla et al. [256], Ni and Ni–Cu catalysts supported on Al_2O_3 and MgO have a crystallite size ranging from 10 to 30 nm and a good performance in MCD reaction.

It is generally accepted that the metal particles are in crystalline state [154] at low temperature, and in a quasi-liquid state at high temperatures [137,147,254]. Baker et al. [137] speculated that the Ni particles have the properties of the liquid during the growth of CNFs based on the distortion pattern of the particles. Li and his coworkers [147,148] suggested that metal particles are in crystalline state in a temperature range of 773–873 K and in a quasi-liquid state at the temperatures higher than 973 K. The melting points of Ni and Cu is 1726 K and 1357 K, respectively, and that of the Ni–Cu alloy is between the two temperatures [257]. Nevertheless, the dissolution of C in the metal particles and the nanosize effect may decrease the melting point effectively [258–260]. It is reasonable to assume that the appearance of metal particle after reaction is dependent on their size and composition, and is also strongly affected by the gas phase composition and the interface with carbon [148]. Moreover, the formation of bamboo-shaped CNFs is closely related to the quasi-liquid state of the metal particles [148].

The size of metal particle is also believed to influence the nature of the resulting SWCNTs. Many groups have conducted experiments to investigate the dependence of the SWCNT diameter on the catalyst particle size. Cheung et al. [261] prepared iron nanoclusters with average values of diameter of 3, 9 and 13 nm, and employed these nanoclusters to grow CNTs. The resulting CNTs have average diameters of 3, 7 and 12 nm, respectively, very relevant to the diameters of the metal particles. The CNTs produced from small (average diameter 3 nm) iron nanoclusters consist primarily of SWCNTs with *ca.* 30% DWCNTs, while the catalyst with medium-sized metal particles produces SWCNTs and thin-walled MWCNTs with typical wall thicknesses of 2–4 graphene layers. The large (average diameter 13 nm) diameter nanoparticles catalyze

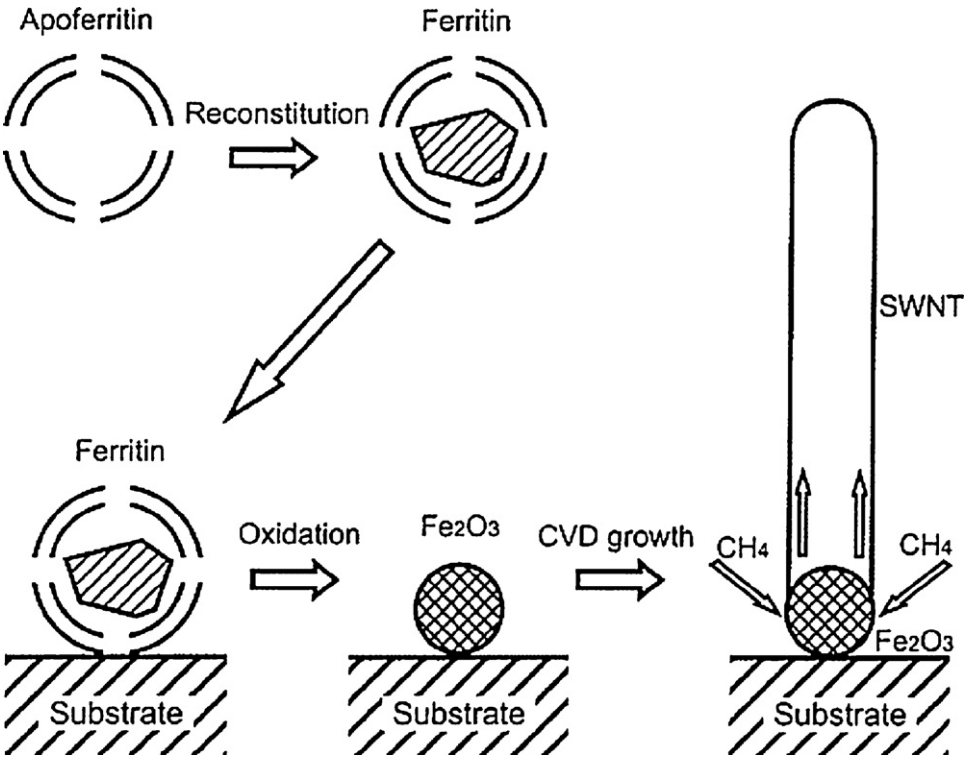

Fig. 22. Schematic process for SWCNTs synthesis on a catalytic nanoparticle derived from apoferritin. Fe(III) are placed into the cores of apoferritins in aqueous solutions to obtain artificial ferritin. The synthesized ferritins are automatically stabilized against agglomeration in aqueous solutions by functional groups on the proteins, and allow the deposition of isolated ferritin on various substrates. Upon high temperature calcination to remove the organic shells and fully oxidize the iron core, discrete iron oxide nanoparticles with mean diameter 1.9 nm are obtained on the substrate. CVD growth with the substrate produces SWCNTs from the discrete catalytic nanoparticles, and the average diameter of the nanotubes (1.5 nm) is found to be close to that of the nanoparticles. To vary the size of iron oxide nanoparticles, catalytic nanoparticles with 3.7 nm in diameter can be derived, and the mean diameter of the produced SWCNTs is 3.1 nm.
Reprinted from [265] with permission of the American Chemical Society.

the growth of thin-walled MWCNTs with typical wall thicknesses of 2–4 graphene sheets, without producing SWCNTs. Uniform iron–molybdenum nanoparticles prepared by thermal decomposition of metal carbonyl complexes were employed for the SWCNTs growth [262]. It is found that there is an upper limit for the size of the catalyst particle to nucleate SWCNTs and this limit is between 4 and 8 nm under their growth conditions. Dai et al. [180] noticed that larger particles always appear to be onionated and are inactive for growth of CNTs. Lamouroux et al. [263] showed the evolution of the CNT diameter according to the particle size, which indicates that the catalyst particle size dictates the tube diameter. The CNTs produced with the smallest catalyst particles of 1–5 nm are primarily SWCNTs with a few DWCNTs, whereas with larger particles MWCNTs forms dominantly, as presented in Fig. 21.

In order to get the most desirable SWCNTs, several attempts have been made to control the size distribution and dispersion of the catalyst particles. Li et al. [262] employed a mixture of long-chain carboxylic acid and long-chain amine as the protective agents, and got uniform iron–molybdenum nanoparticles. Rashidi et al. [264] tested several kinds of organic additives, and showed that the sorbitol-reduced catalyst has the smallest metal particle size of 2.5 nm. Using organic carrier, such as apoferritin [265,266] or polyamidoamine dendrimers [267], Dai and co-workers obtained discrete catalytic nanoparticles with diameters in the range of 1–5 nm, and grew isolated SWCNTs with these nanoparticles. Fig. 22 shows the schematic of the process for SWCNTs synthesis on catalytic nanoparticles derived from apoferritin. In order to obtain suitable metal particle size during high temperature reduction, mixed metal oxides were used as the catalyst precursor. Govindaraj and coworkers [268,269] employed a catalyst reduced from $Mg_{1-x}M_xAl_2O_4$ spinel for the growth of SWCNTs, and showed that the metal nanoparticles (<5 nm) are formed during reduction, which are active for the SWCNTs growth. Calcination at 1223 K for 8–12 h of an Fe/MgO catalyst prepared by impregnation was found to result in a uniform $MgFe_2O_4$/MgO solid solution [270]. When methane was exposed to the heat-treated catalyst at 1173 K, small iron enriched particles (<5 nm) appear on the catalyst surface due to the reduction effect, and are active for SWCNTs growth. Fig. 23 illustrates the catalyst preparation and SWCNTs growth with $MgFe_2O_4$/MgO as a catalyst precursor.

2.7. Metal–support interaction

Metal–support interaction (MSI) is known to influence the reduction of metal oxide precursors and metal dispersion on supported metal catalysts. A strong MSI increases the difficulty of reduction of the precursor oxide, either by increasing the reduction temperature of the oxide or by the production of metal–support species that is difficult to reduce or even irreducible [271,272]. Furthermore, a strong MSI decreases the mobility of the metal particles on the support surface so that the metal dispersion is enhanced. It may also change the crystallography and the electronic state of the metal particles, which consequently affect the activity and stability of the catalyst in MCD reaction. It has been found that a weak interaction results in a tip-growth mode, i.e. the catalyst particle is lifted up by the growing CNM and continues to promote CNM growth at its tip, while strong interaction leads to a base-growth mode, i.e. CNM grows up with the catalyst particle rooted at its base, as presented in Fig. 24.

Ermakova et al. [254] got superior activity with a silica-supported nickel catalyst containing 85–95% Ni with Cu as a dopent

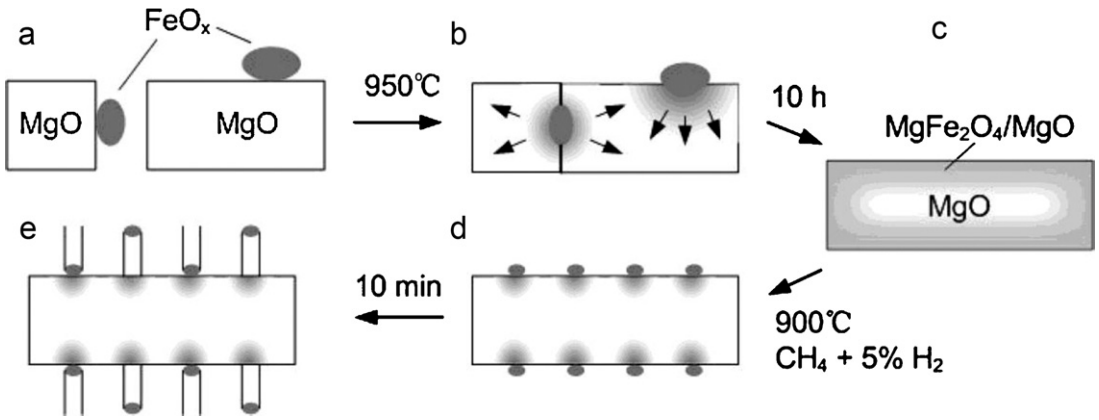

Fig. 23. Proposed mechanism by Ning et al. of the heat treatment and SWCNT growth over the Fe/MgO catalyst: (a) the noncalcined Fe/MgO catalyst prepared by impregnation; (b and c) formation of the $MgFe_2O_4$/MgO solid solution by heat treatment at 1223 K for 10 h from the diffusion of iron into the MgO lattice; (d) some small iron-enriched particles appearing on the surface of the catalyst particle due to reduction by the CH_4 reactant at 1173 K; (e) carbon nanotube growth from the iron enriched particles. Reprinted from [270] with permission of the American Chemical Society.

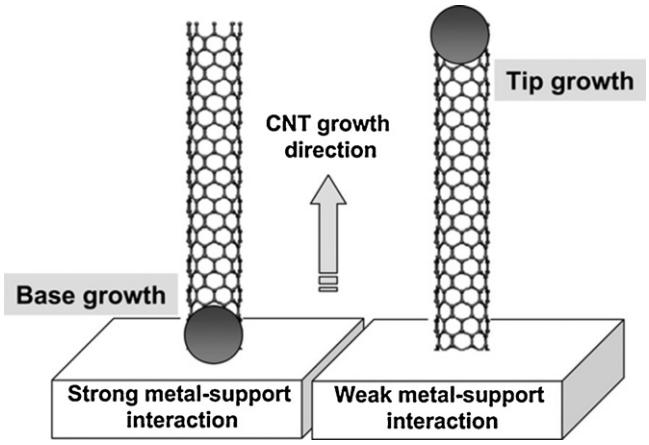

Fig. 24. Schematic representation of the base and tip growth mechanism of CNT. The MSI has influence on the growth mechanism. If the interaction is not very strong and in any case weaker than the metal–carbon one, the particle is detached from the support and localized at the nanotube tips. Otherwise, the metal particle remains anchored to the support.
Reprinted from [263] with permission of Taylor & Francis Group, LLC.

to the NiO–MgO catalyst. They attributed the lower activity of the NiO–MgO catalyst to the presence of a strong MSI and the formation of a NiO–MgO solid solution. Li et al. [273] reported that the interaction between Ni and Ce influence the activity. For a Ni/CeO_2 catalyst prepared by impregnation or deposition–precipitation method, the nickel particles locate on the top of the formed CNFs and act as the active centers for MCD reaction, while the nickel particles in the Ni/CeO_2 catalyst prepared by a co-precipitated method are covered by the graphite carbon or incorporated into the CNFs, so that they show a low reaction rate. The authors believed that the Ni/CeO_2 catalyst prepared with co-precipitation method exhibits a strong MSI through the formation of a Ni–O–Ce solid solution. Li et al. [274] investigated the effect of MSI on the CNFs formation on a series of Co–silica catalysts. The MSI was manipulated by the addition of BaO, La_2O_3 or ZrO_2 to silica. The catalyst deactivation rate was found to get faster with the increase of the MSI. In the case of the catalyst with strong MSI, the encapsulating carbon formation is dominant and hence leads to a rapid deactivation of the catalyst. Zhu et al. [275] found that MSI becomes stronger after a plasma treatment and the CNF growth mode is changed from a mixed tip and base growth for the untreated sample to a base growth mode for the plasma treated sample. The strong interaction results in a low CH_4 conversion rate and low carbon yield on the plasma treated Ni/Al_2O_3 catalyst. A strong MSI often means a low carbon yield and a short life time of the catalyst, which may be due to the difficulty in detachment of the metal particles from the support.

A strong MSI allows high metal dispersion and thus a high density of the catalytic sites. A suitable strength of MSI facilitates to prevent metal clusters from aggregation and forming unwanted large particles which result in graphite particles or defective MWCNTs. Cassell et al. [176] reported that Fe–Mo particles on alumina (Al_2O_3) produce a much higher amount of SWCNTs than those grown on SiO_2, which is an example of suitable MSI. They observed that 95% of the SWCNTs ends are free of metal particles. However, there is also a small fraction (5%) of SWCNTs having metal particles at their ends, which suggests that the SWCNTs are formed predominantly through the base growth mechanism, and the tip-growth is the secondary SWCNT growth mechanism in their process. Kong et al. [175] proposed that the SWCNTs in their MCD processes grow via the base-growth mechanism, since all the observed ends appear closed and particle-free. Ago et al. [276] used MgO supported iron catalyst and studied the roles of MSI in the growth of SWCNTs. Their results showed that the iron particles become smaller when annealed in Ar which is due to the strong MSI between iron and MgO. The metal particle size then decides the diameter of the SWCNTs. These findings provide some clues for controlling the structure of the CNM.

2.8. Catalyst deactivation

During MCD reaction, carbon deposits continuously on the catalyst and forms graphite-like structures. Carbon deposition or coking phenomenon has long been recognized as a reason of metal catalyst deactivation in hydrocarbon processing reactions [277]. Coking is generally referred to as deposition of a variety of carbon species, such as carbonaceous, containing polyaromatic structure with high carbon-to-hydrogen ratio, amorphous and graphite-like carbons. The graphite-structured carbon species are found to cover the meal surface which leads to deactivation and damage the catalyst granulate structure due to volume expansion in several commercial processes [113–115]. MCD and CO disproportionation reactions have been attributed to as the two major reactions leading to coking and deactivation in hydrocarbon and syngas processing processes [278].

However, MCD reaction can stay in a quasi-stable state under some special reaction conditions, while the catalyst may quickly deactivate in some other circumstances. For catalyst design and reaction optimization, it is important to understand and describe correctly the deactivation mechanism and process. Site-blocking

Table 3
Performance of different supported metal catalysts for MCD reaction.

Reference	Catalysts	Reactor	Max methane conversion	Carbon yield	Reaction temperature (K)	Reduced temperature (K)	Feed	Activity maintained (h)
[51]	9Ni–1Al (atomic ratio)	Fixed-bed	20%	244 g C/g Ni	773	1023	CH_4:N_2 = 0.6:0.4 (vol)	More than 40
[51]	2Ni–1Cu–1Al (atomic ratio)	Fixed-bed	70%	191 g C/g Ni	1023	973	CH_4/N_2 = 0.37:0.63	13
[146]	9Ni–1Al (atomic ratio)	An *in situ* thermal balance		116.4 g C/g Ni	773	973	CH_4/N_2 = 1:2	More than 6.7
[165]	15Ni–3Cu–2Al (atomic ratio)	Fixed-bed	22%	630.6 g C/g Ni	873	973	Undiluted methane	70
[165]	15Ni–3Cu–2Al (atomic ratio)	Fixed-bed	60%	465 g C/g Ni	973	973	Undiluted methane	20
[165]	2Ni–1Cu–1Al (atomic ratio)	Fixed-bed	70%	362.5 g C/g Ni	1023	973	Undiluted methane	10
[216]	87Ni–3Cu–10Al (wt.%)	Vibrating flow reactor	12%	275.9 g C/g Ni	823	823	Undiluted methane	28
[216]	90Ni–10Al (wt.%)	Vibrating flow reactor	16%	161.1 g C/g Ni	823	823	Undiluted methane	15.5
[295]	50Fe–50Al_2O_3 (wt.%)	Vibrating flow reactor	4%	53 g C/g Fe	898	853	Undiluted methane	23
[295]	50Fe–6Co–Al_2O_3 (wt.%)	Vibrating flow reactor	8%	104.8 g C/g Fe	898	853	Undiluted methane	40
[311]	70Ni–10Cu–10Fe–10Al_2O_3 (mole ratio)	Rotating reactor	60%	17.14 g C/g Ni	973	973	Undiluted methane	More than 14
[304]	60Ni–25Cu–15SiO_2 (mole ratio)	Fixed-bed	60%	801 g C/g Ni	923	873	CH_4/He = 1:1	30
[334]	23Ni–77La_2O_3 (wt.%)	Fixed-bed	75%	78.2 g C/g Ni	973	973	Undiluted methane	22
[340]	15Ni–85CFC (wt.%)	Vibrating flow reactor	10%	224 g C/g Ni	798	623	Undiluted methane	16
[341]	15Ni–85CFC (Fe–Ni) (wt.%)	Vibrating flow reactor	8.5%	268.5 g C/g Ni	798	623	Undiluted methane	20.5
[341]	10Ni–90CFC ((Ni) + CO_2) (wt.%)	Vibrating flow reactor	12%	229 g C/g Ni	798	623	Undiluted methane	11.5
[341]	10Ni–90CFC ((Ni) + H_2) (wt.%)	Vibrating flow reactor	9%	238 g C/g Ni	798	623	Undiluted methane	12.75
[344]	50Ni–50Ce–MCM41 (wt.%)	Fixed-bed	70%	More than 155.2 g C/g Ni	853	773	CH_4/Ar = 1:1	More than 23
[396]	NiO	Fixed-bed	10%	More than 398 g C/g Ni	773	773	Undiluted methane	More than 75
[356]	90Ni–10SiO_2 (wt.%)	Vibrating flow reactor	18%	375 g C/g Ni	823	823	Undiluted methane	30
[432]	10Ni–90SiO_2 (wt.%)	90Pd10Ag membrane reactor	70%	More than 200 g C/g Ni	773	673	CH_4/N_2 = 1:9	60
[435]	19.5Ni–80.5SiO_2 (wt.%)	Multilayer reactor	35.2%	61.3 g C/g Ni	773	773	CH_4/N_2/Ar = 10:5:85	13.6

and pore-mouth plugging models have often been adopted to explain the kinetic data of catalyst deactivation due to coking. Zhang and Amiridis [279] calculated the amount of carbon needed to deactivate the MCD catalyst based on the two models. Their results showed that it needs only 10 mg and 250 mg carbon, respectively in the two models to completely deactivate 1 g catalyst. However, at 823 K they completely deactivated 0.2 g catalyst with 0.59 g carbon, indicating deposition of 2700 carbon atoms on each surface nickel atom.

The rate of methane dissociation, carbon diffusion and CNF growth should be equal at the steady state in MCD reaction. Only at this condition, carbon does not accumulate on the exposing face of metal particle which adsorbs and dissociates methane. However, if this balance breaks, carbon forms a covering layer on the active surface for methane, the catalyst deactivates and the CNF growth stops. This deactivation mechanism was confirmed by many experiments. For instance, it was observed with TEM that the metal particles at the tips of the CNFs are coated with non-reactive carbon layer [137,154,280]. Ruckenstein and Hu [281] confirmed this observation also with XPS method. Takenaka et al. [282] proposed that catalyst deactivation is related to the change of Ni structure. They also detected the presence of a nickel carbide (not Ni_3C, but with Ni–C bonds) on deactivated Ni catalyst with XANES and EXAFS. Another deactivation mechanism states that the metal particles are fragmented and encapsulated within the hollows of fibers [283]. This phenomenon occurs usually at high temperatures, and when the metal particles are in quasi-liquid state [147,254]. Salmones et al. [284] compared the lifetimes of a Ni–Mg–Al catalyst with different Ni content, i.e. 15 wt.% Ni, 25 wt.% Ni, and 50 wt.% Ni. They found the catalyst with a higher Ni content deactivates faster than that with a lower Ni content and postulated that this phenomenon is related to the low accessibility of the active Ni particles locating inside the ink-bottle pores, which are easily embedded by the produced carbon materials in a short time period of reaction. While, the Ni particles in the catalyst with low Ni content are mainly located in the opening pores or situated on the tips of the produced CNTs, remaining its high accessibility for continuous reaction.

3. Catalyst for the reaction

3.1. General remarks

Due to its very strong C–H bond (440 kJ/mol) and high symmetry of the molecular structure, methane is the most inactive

hydrocarbon, and its decomposition can only take place efficiently at a temperature higher than 1473 K in the absence of a catalyst. In order to realize the MCD process with a moderate condition, various metal catalysts [114–116,167] and different supports have been studied extensively [285–287].

The general reaction mechanism on different metal catalysts has been supposed to be similar. However, the chemical composition and preparation method, the support and promoter influence the activity and stability and determine the structure and morphology of the carbon formed. Table 3 summarizes the performances of different catalysts for MCD reaction reported in the literature.

3.2. The active component

In general, Ni-based and Co-based catalysts have sufficient activity for MCD reaction in the temperature range 723–1073 K. However, for Fe-based catalysts, the activation temperature is generally over 973 K.

Fig. 25 summarizes the available literature data on the catalysts, preferred reaction temperature range and carbon products of MCD reaction [56]. Zhang and Smith [288] reported that the Ni-based catalysts are more active and stable than Co-based ones under the same reaction conditions. Chen et al. [289] found that the activity order for Fe/Al_2O_3, Co/Al_2O_3 and Ni/Al_2O_3 catalysts is a reverse of that of their melting points and is also a reverse of that of their initial temperatures for the deactivation.

Metallic Ni has been used intensively as the active component of catalysts for hydrogenation and dehydrogenation of hydrocarbons [290]. In the commercial processes concerning methane, such as steam reforming, methanation and Fischer–Tropsch processes, Ni catalysts have been used [114–116]. For MCD reaction, Ni is also the most intensively investigated catalytic component, and exhibits high activity and carbon yield. However, a gradual deactivation takes place inevitably during the reaction. The catalyst consumption during the reaction and its activity profile influence eventually the product cost. Therefore, the important parameters for the MCD catalyst are the yields of carbon and hydrogen per unit mass of active component until its deactivation [283].

Besides Ni, several other transition metals have activity for MCD reaction [291,292], as summarized in Fig. 26. Compared to nickel-based ones, Co and Fe catalysts have lower activity and lower carbon yield [293–295]. However, the CNMs formed with those catalysts have different property and morphology.

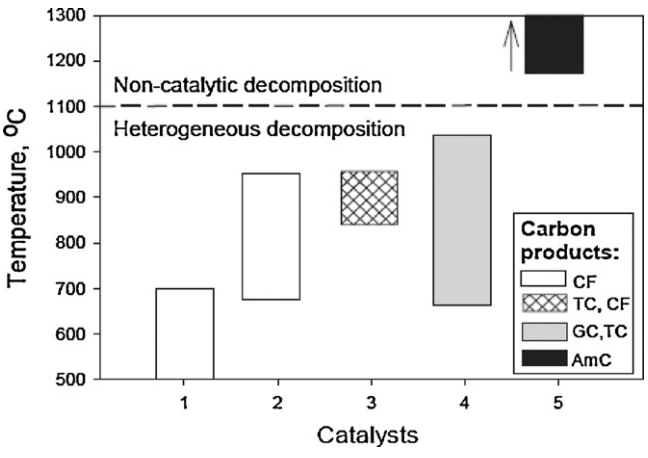

Fig. 25. Graphical representation of the bulk of literature data on catalysts, preferred temperature range and carbon products related to catalytic methane decomposition reaction. Catalysts: 1 – Ni-based, 2 – Fe-based, 3 – carbon-based, 4 – summary of data related to Co, Ni, Fe, Pd, Pt, Cr, Ru, Mo, W catalysts, 5 – non-catalytic decomposition. Carbon products: CF – carbon filaments, TC – turbostratic carbon, GC – graphitic carbon, AmC – amorphous carbon.
Reprinted from [56] with permission of Elsevier Science Publishers, B.V.

Zarabadi-Poor et al. [296] examined the morphology of the CNMs formed over a Fe/alumina catalysts with different iron content. They showed that MWCNTs with good length and narrow diameter are obtained with the low iron loading catalysts during the MCD reaction, while with the catalyst with increased Fe loadings, there is a higher probability to grow carbon nanoribbons rather than CNTs. Ermakova et al. [293] investigated Fe and Ni catalysts for MCD reaction and found that the preparation method and the composition of catalyst have important influence on the activity and the amount of carbon finally formed. They suggested that Fe is in α-Fe structure in the working state. In their experiment, MWCNTs were obtained, while CNFs were produced usually on Ni-based catalysts. Avdeeva et al. [297] also examined Co-based catalyst in the temperature range of 748–873 K and compared the catalytic performance with the amount of carbon accumulated before deactivation as a measure. They showed that the performance of Co catalyst is very similar to that of Ni-based ones. A catalyst prepared with a coprecipitation technique with 60–75 wt.% Co supported on Al_2O_3 show good performance at 773 K. Colomer et al. [141] investigated Fe, Co and Ni supported catalysts for SWCNT production from MCD reaction in a horizontal quartz boat reactor at 1273 K. Among the catalysts tested, Co/MgO (2.5 wt.%) catalyst shows the best performance for the SWCNTs growth. Govindaraj et al. [268] examined Fe, Co and Ni catalysts derived from the reduction of $Mg_{1-x}M_xAl_2O_4$ for the growth of CNTs. They showed that the nature of the transition metal strongly affects the conversion of CH_4 into carbon species. Fe provides the highest yield of carbon and Ni the lowest, while Co giving an intermediate value. Fonseca et al. [298] summarized their experimental results and proposed that iron is more active than cobalt, but the quality of the CNMs obtained, in terms of graphitization and structure, is not as good as with cobalt as catalyst.

It is well known that, Fe, Co and Ni have partially filled 3*d* orbitals which facilitate the dissociation of the hydrocarbon molecules through partially accepting electrons. This interaction along with "back-donation" from the metal into the unoccupied orbital in the hydrocarbon molecule changes the electronic structure of the adsorbed molecule so that the dissociation of the molecule occurs [178]. Copper, a non-transition metal with its 3*d* shell completely filled, was observed to yield only amorphous carbon. However, MgO supported Cu catalyst doped with Mo or W, shows activity for growth of the bamboo-shaped CNF [172,173]. DFT calculations show that Cu/W and Cu/Mo composite particles have binding energies in the same range as Fe, Co and Ni. The addition of a dopant to Cu in an appropriate ratio modifies the binding energy into a certain range suitable for carbon species formation.

3.3. The promoter

MCD reaction is endothermic, and a comparatively high reaction temperature is favorable for getting both high methane conversion and hydrogen purity. Li et al. [53] proposed that 1073 K or higher is the favorable reaction temperature range. However, Ni/Al_2O_3 catalyst has likely an optimum reaction temperature irrespective to the composition at which only limited conversion can be achieved (see Fig. 27). In order to improve the high temperature activity and stability, the doping effect of Cu on Ni/Al_2O_3 catalysts has been investigated [51,53,299]. Li et al. [146,299] used a catalyst with high metal loading and prepared from coprecipitation via Feitknecht Compound (FC, or Hydrotalcite-like compound (HTLC) as it is often called also. We prefer FC because it reflects the history of the discovery) precursor. Their results show that the addition of copper into Ni/Al_2O_3 catalyst promoted the production of CNFs and hydrogen by shifting the optimum reaction temperature to a higher range

Group	1	2		3	4	5	6	7	8	9	10	11	12	13	14	15	16	17	18
Period																			
1	1 H																		2 He
2	3 Li	4 Be												5 B	6 C	7 N	8 O	9 F	10 Ne
3	11 Na	12 Mg												13 Al	14 Si	15 P	16 S	17 Cl	18 Ar
4	19 K	20 Ca		21 Sc	22 Ti	23 V	24 Cr	25 **Mn**	26 **Fe**	27 **Co**	28 **Ni**	29 **Cu**	30 Zn	31 Ga	32 Ge	33 As	34 Se	35 Br	36 Kr
5	37 Rb	38 Sr		39 Y	40 Zr	41 Nb	42 **Mo**	43 Tc	44 **Ru**	45 **Rh**	46 **Pd**	47 Ag	48 Cd	49 In	50 Sn	51 Sb	52 Te	53 I	54 Xe
6	55 Cs	56 Ba	*	71 Lu	72 Hf	73 Ta	74 W	75 Re	76 Os	77 **Ir**	78 **Pt**	79 Au	80 Hg	81 Tl	82 Pb	83 Bi	84 Po	85 At	86 Rn
7	87 Fr	88 Ra	**	103 Lr	104 Rf	105 Db	106 Sg	107 Bh	108 Hs	109 Mt	110 Ds	111 Rg	112 Uub	113 Uut	114 Uuq	115 Uup	116 Uuh	117 Uus	118 Uuo

*Lanthanoids	*	57 La	58 Ce	59 Pr	60 Nd	61 Pm	62 Sm	63 Eu	64 Gd	65 Tb	66 Dy	67 Ho	68 Er	69 Tm	70 Yb
**Actinoids	**	89 Ac	90 Th	91 Pa	92 U	93 Np	94 Pu	95 Am	96 Cm	97 Bk	98 Cf	99 Es	100 Fm	101 Md	102 No

Fig. 26. Summary of metals used for MCD reaction. "M" : used as active component or secondary component; "M" : used as active component; M : used as secondary component [53,54,143,152,167,289,291,293,295,297,312,313].

[51,299]. They postulated that this promotion effect is actually achieved by lowering the intrinsic activity of nickel, thus moderating the deactivation rate and shifting the optimum temperature [51]. The conversion of methane on a catalyst with a composition of Ni:Cu:Al = 2:1:1 reached 70% at 1023 K and maintained for 13 h, meanwhile, almost 200 g carbon was accumulated on 1 g catalyst (nickel base). The catalyst with a composition of Ni:Cu:Al = 15:3:2 (mole ratio) was then used for the reaction with undiluted methane at 873 K. A longer stable time with a lower conversion but a much larger amount of carbon accumulation was observed, as plotted in Fig. 28 [51]. Suelves et al. [300,301] studied Ni–Al and Ni–Cu–Al catalysts prepared by co-precipitation, fusion and impregnation

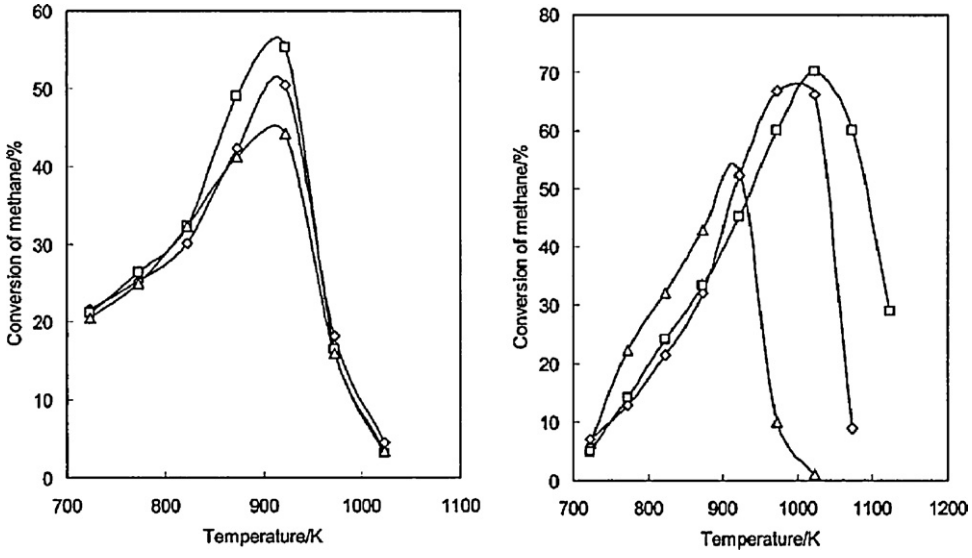

Fig. 27. Conversion of methane on alumina supported Ni–Cu catalyst with stepwise heating, CH_4:N_2 = 0.37:0.63 (vol). Left: Ni catalysts without Cu doping; △: Ni:Al = 2:1; ◇: Ni:Al = 3:1; □: Ni:Al = 9:1. Right: Ni catalysts with Cu; △: Ni:Cu:Al = 75:2:23; ◇: Ni:Cu:Al = 15:3:2; □: Ni:Cu:Al = 2:1:1. This figure tells that for the catalyst without Cu, the optimum reaction temperature does not change with the Ni content, while, for the Cu doped catalyst, as the increase of the amount of Cu doped into the catalyst, the optimum reaction temperature for the MCD reaction shifts to higher temperature range.
Reprinted from [51] with permission of the American Chemical Society.

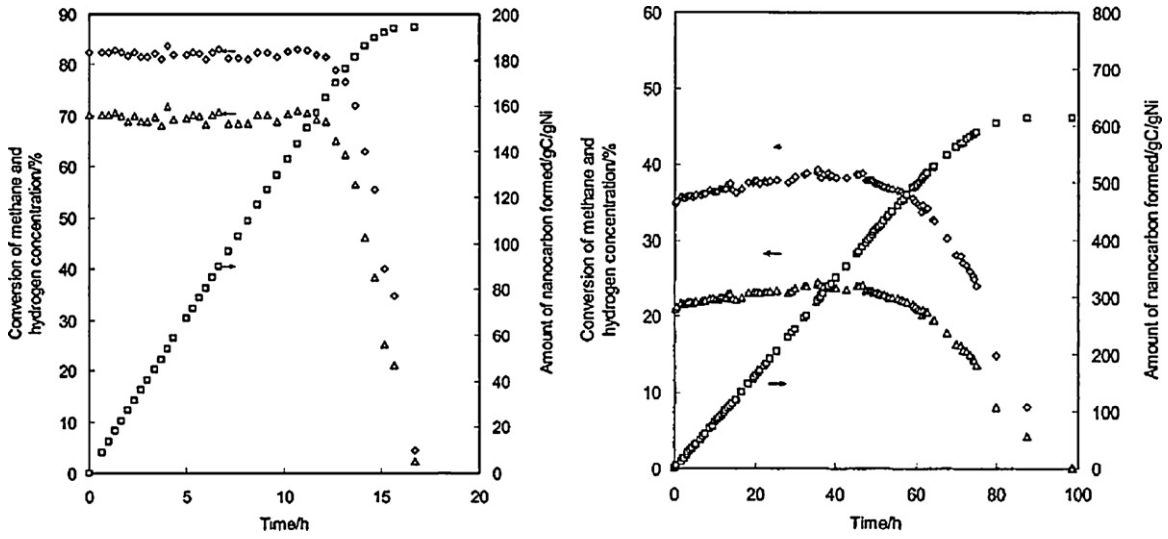

Fig. 28. Decomposition of methane on Ni–Cu–alumina catalysts. Left: at 1023 K. Catalyst composition Ni:Cu:Al = 2:1:1 (mol); feed composition CH_4:N_2 = 0.37:0.63 (vol); △: conversion of methane; ◊: concentration of hydrogen; □: amount of nanocarbon formed. Right: 873 K with a feed of pure methane; catalyst composition Ni:Cu:Al = 15:3:2 (mol); △: conversion of methane; ◊: concentration of hydrogen in product; □: amount of nanocarbon formed. The life time of the catalyst in this work is sufficient for an application in a fluidised bed reactor.
Reprinted from [51] with permission of the American Chemical Society.

techniques and concluded that doping of Cu has a strong influence on Ni dispersion and enhances the catalytic activity of MCD reaction at 973 K.

Cunha et al. [302] tested Raney-type Ni catalyst and showed that the doping with Cu improves the catalyst stability due to the formation of Ni–Cu alloy and stimulates the formation of an ensemble effect, decreasing the rate of encapsulating carbon formation. They proposed that Cu plays the same role in Raney-type Fe catalyst doped with Cu [303]. Ashok et al. [304] examined the effect of Cu content in a Ni–Cu–SiO_2 catalyst and revealed that Cu significantly influences the activity of Ni for methane decomposition. They got carbon accumulation of 801 g/g Ni at 923 K with a Ni–Cu–SiO_2 (mole ratio of 60:25:15) catalyst. Monzon et al. [305] investigated the effect of the Cu addition in a Ni–Mg–Al catalyst and their results also showed that a low Cu content doping improves the activity and stability of the catalyst. Lazaro et al. [306] found that the presence of Cu results in the formation of a more ordered graphitic carbon.

Ni and Cu form alloy over a wide range of composition at temperatures higher than 627 K [307]. The formation of Ni–Cu alloy in a Ni–Cu–alumina catalyst was confirmed with an Auger imaging method, in which nickel and copper locate at the same position [308,309]. Cu in nickel-based catalysts has several effects. Cu is much easier for reduction than Ni. The reduced Cu in low temperature acts as the center of hydrogen molecule activation and facilitates the reduction of Ni from oxide phase, so as to help the release of Ni from the mixed oxide, even the spinel like phases. Cu is rich with *d* electrons, which may exert electronic effect on Ni. Metallic Ni diluted by Cu is less active than pure Ni for methane dissociation so that it retards the accumulation of carbon atoms. Furthermore, Cu affects the affinity of specific metal surface with graphite. Gonzalez et al. [310] studied the promotion effect of Cu to unsupported nickel nanoparticles. Their results suggested that copper induced the disaggregation of nickel particles during the course of the reaction, resulting in the formation of CNT with a narrow diameter distribution. However, their results did not show that Cu has an effective improvement of the quantity of the CNTs produced.

Chesnokov and Chichkan [311] found that the modification of a Ni–Cu/Al_2O_3 catalyst with iron improves the stability, which is due to the formation of finely dispersed Ni–Cu–Fe alloy particles. They think that the diffusion coefficiency of carbon atoms through iron is three orders of magnitude higher than that through nickel, so that doping with iron moderates the gradient of carbon concentration in the metal particles. Iron may also decrease the methane decomposition rate and accelerate the carbon removal rate on the metal surface. Takenaka et al. [312] investigated the doping effect of Cu, Rh, Pd, Ir and Pt on the Ni-based catalyst and found that doping with Pd slowed down the deactivation of a Ni/SiO_2 catalyst, while the addition of the other metals all reduced the yield of carbon product. The formation of Pd–Ni alloy is detected by XRD measurement, which accounts for the increase of carbon yield and the improvement of the CNF morphology. Shah et al. [313] compared the activity of 0.5% Fe–Al_2O_3 catalyst with that of 0.5%M–4.5%Fe/Al_2O_3 (M = Mo, Ni, or Pd), and showed that the bimetallic catalysts have better performance in the reaction. Ogihara et al. [314] tested the activity of M/Al_2O_3 (M = Fe, Co, Ni, and Pd) and Pd–M/Al_2O_3 (M = Fe, Co, Ni) catalysts. Pd–Co/Al_2O_3 shows the highest carbon yield at 1013 K among the tested catalysts.

Chen et al. [315] found that doping ZnO into a Ni–Al_2O_3 catalyst enhances both the activity and stability. A strong interaction between Ni–Al_2O_3 and ZnO was observed, which is likely resulted in the formation of $ZnAl_2O_4$ spinel-like structure. They assumed that ZnO also delays the appearance of the quasi-liquid state of the metal particles during the reaction and weakens the interfacial wetting effect of metal particles on the growing carbon layer thus delays the encapsulation of metal particles. Gonzalez et al. [316] investigated MCD reaction on a Ce-doped Ni/SiO_2 catalyst and observed that the addition of Ce brings about a significant increase in catalyst stability. The nickel reduction extent decreases even with a small amount of Ce doping. A Ni/SiO_2 catalyst deactivates completely after reaction for 20 h at 853 K, while the catalyst doped with Ce has higher initial methane conversion and the conversion changes only from 50% to 40% after 150 h of reaction under the same condition. They showed further that CeO_2 enhances the dispersion of the Ni particles. Zapata et al. [317] also confirmed the positive effect of Ce in Ni/SiO_2. They believed that the Ce addition prevents the sintering of nickel particles during reduction process and maintaining a random distribution between the silica and cerium oxide.

Alkali metal oxides such as Na_2O and K_2O have been proved to be harmful to the transition metal catalysts both for MCD and methanation reactions [233,318,319]. The addition of 4 wt.% of Na to Ni/Al_2O_3 lowers the nickel surface area of a reduced catalyst from 29 to 7 m^2/g and increases the mean metal particle size from 11 to 43 nm [319]. Qian et al. [318] observed a decrease of carbon yield for the catalyst doped with Na_2O. Hussain et al. [320] also found that the addition of K restricts the formation of graphitic carbon. Another work showed also that the rate of MCD reaction on an iron catalyst doped with K_2O is six times lower than a catalyst without K_2O [233], and Zapata et al. [317] showed that the addition of K_2O in Ni/SiO_2 results in a lower stability.

Italiano et al. [321] investigated Ni based thin layer catalyst for MCD reactions and evaluated the effect of basic and acidic dopants, e.g. Mg, K, La and Cl, on the activity and stability of the catalyst. They found that CNFs form on Mg, La and Cl doped samples, while only the encapsulating types of carbon form on a K doped sample.

Other metals, such as molybdenum, platinum and ruthenium have been used in combination with active metals to achieve better activity and selectivity for the growth of SWCNTs. Cassell et al. [176] discovered a synergetic effect between iron and molybdenum. They used Fe–Mo supported catalyst in MCD reaction at 1173 K. The product consists SWCNT bundles (SWCNT diameter: 0.7–5 nm) and a little amount of DWCNT, free of amorphous carbon. They attributed the high yield of SWCNTs to the roles played by Mo species in promoting the aromatization of methane at elevated temperatures. Ago et al. [322] employed a Fe–Mo/MgO catalyst for the SWCNTs growth and suggested that the carbonization of Mo yields graphite through the formation of Mo_2C compound. Therefore, it is likely that Mo suppresses the formation of excess amorphous carbon on the surface of Fe nanoparticles through the enhancement of the nanotubes precipitation, thus preventing the rapid deactivation of the catalyst. A synergetic effect between cobalt and molybdenum was also discovered by Tang et al. [323]. They found that the addition of molybdenum to Co/MgO catalyst remarkably increases the yield and also improved the quality of SWCNTs. The generation rate of SWCNTs was increased at least 10 times and the formation of amorphous carbon was suppressed. Ni et al. [324] found that Co–Mo/MgO has a more stable activity than Co/MgO catalyst, it may be due to the formation of Mo_2C, reducing the rate of CH_4 dissociation, and balancing the rate of CH_4 dissociation with the rate of carbon migration. Yoon et al. [325] employed a Co–Mo film catalyst for the growth of SWCNTs. They believed that the addition of Mo in the Co catalyst provides effective nucleation sites for SWCNTs formation.

Bimetallic catalysts such as Fe–Ru and Fe–Pt with a particle size range of 0.5–3 nm were prepared by accomplishing the chemical reduction under microwave irradiation and with poly(N-vinyl-2-pyrrolidone) as a protective agent [326]. The use of bimetallic catalysts Fe–Pt and Fe–Ru improved the production of SWCNTs by at least 200%. Possible reasons for the synergetic effect were attributed to three effects, i.e. the enhanced ability of bimetallic nanoparticles in the decomposition of methane and in the dissolution of carbon atoms; the improved wetting ability of bimetallic nanoparticles on SiO_2 surface; and the stronger binding energy between bimetallic nanoparticles and graphene sheets for the formation of graphene caps.

3.4. Support

The support plays an important role in every catalyst. Li et al. [146] reported Ni/Al_2O_3 catalyst is active and stable while pure NiO is inactive under certain conditions. Both the samples were prepared by a coprecipitation method. In good agreement, Toebes et al. [327] also noticed that negligible amount of CNF formed on an unsupported Ni catalyst. However, they reported in the same work, the unsupported catalyst is very stable and active for C_2H_4 decomposition. They think that CH_4 dissociation has a higher activity demand than C_2H_4 decomposition.

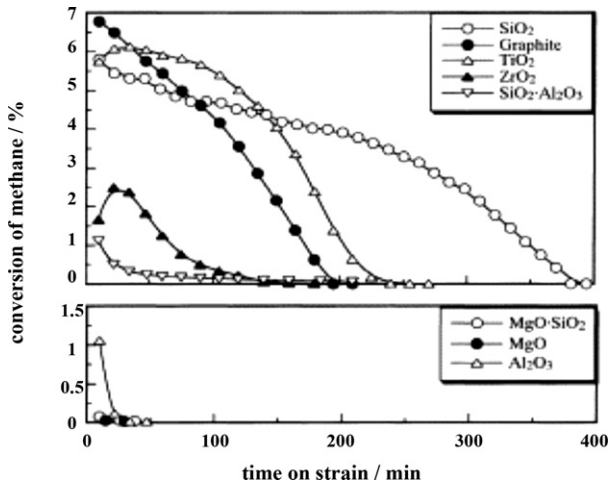

Fig. 29. Methane conversion over Ni catalysts supported on different supports at 773 K.
Reprinted from [287] with permission of Elsevier Science Publishers B.V.

Takenaka et al. [287] compared the performance of Ni catalyst supported on different supports, i.e. SiO_2, TiO_2, ZrO_2, MgO/SiO_2, MgO, SiO_2/Al_2O_3, Al_2O_3 and graphite. The supports such as SiO_2, TiO_2 and graphite catalysts are highly activity and stable, while Al_2O_3, MgO and SiO_2–MgO catalysts are inactive under the same conditions, as shown in Fig. 29. They proved further with XRD and Ni K-edge XANES/EXAFS that in the active catalysts Ni presents in the metallic state, whereas in the inactive catalysts Ni forms oxide compounds (–O–Ni–O–M–; M = Mg, Al and Si) with the components of the support. In another work of the same group [167], Co-based catalysts supported on different supports, i.e. MgO, Al_2O_3, SiO_2 and TiO_2 were examined, and the results (Fig. 30) show that Co/Al_2O_3 and Co/MgO have higher activity than Co/TiO_2 and Co/SiO_2. They

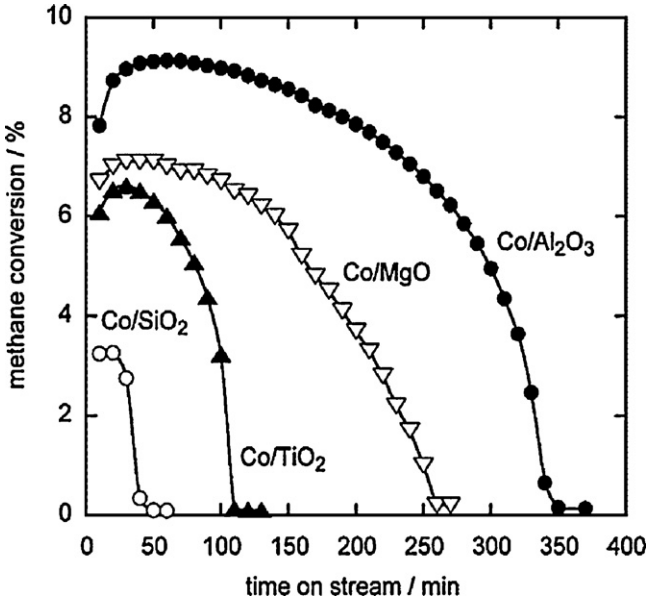

Fig. 30. Change of the methane conversion as a function of time on a stream of methane in methane decomposition at 773 K over Co catalysts supported on different supports. Catalysts: 0.060 g, loading of Co: 20 wt.%, $P(CH_4)$: 101 kPa, and flow rate: 50 ml/min.
Reprinted from [167] with permission of the American Chemical Society.

found that Co in Co/Al_2O_3 and Co/MgO have smaller particle sizes, and that Co particles with diameters in 10–30 nm grow CNFs more easily, while Co particles over 30 nm have no activity. Their results obtained with Co K-edge XANES and EXAFS techniques confirmed that Co always presents as metal during the reaction, irrespective to the kinds of catalyst support and the reaction temperature. Bonura et al. [328] employed a temperature programmed catalytic reaction (TPCR) technique to evaluate the activity of the supported Ni catalyst. Their results showed that the nature of the supports slightly affects the onset temperature of the MCD reaction.

It has been proved that a nickel catalyst obtained through the reduction of the solid solution of NiO and MgO has very small nickel particle size [329]. A recent work [330] reconfirms this concept and proves that the small nickel crystallite has a strong interaction with magnesia and has a very high initial MCD reaction rate. Ismagilov et al. [331] prepared CNFs through MCD reaction over a Ni catalyst which was loaded on the surface of a silica glass fiber support. They prepared samples of CNF with different carbon contents (6.5–55 wt.%) with MCD reaction, and found that the catalyst prepared with washcoat method forms CNFs with diameters 20–50 nm and with high carbon capacity *ca.* 55 g C/g Ni.

Perovskite structured oxides have been recently investigated as the precursor of MCD catalyst [332–335]. The reduction of a perovskite precursor leads to the formation of small metal particles and strong interaction between metal and support, thus enhancing the activity of the catalyst and improving the structure of the carbon formed. Liu et al. [336] obtained SWCNTs with a narrow distribution of diameters (0.8–1.8 nm) over Fe nanoparticles prepared *in situ* by the reduction of $LaFeO_3$. They believed that very fine iron nanoparticles are uniformly and closely distributed on $LaFeO_{3-x}$ which is responsible for the growth of SWCNTs. Chen et al. [332] studied MCD reaction over a $Ni–Co/La_2O_3$ catalyst and obtained good activity and carbon yield without pre-reduction. Kuras et al. [333] also tested Ni based catalyst from perovskite precursor and got very good stability at high temperatures. They found also that the reduction and the reaction temperatures excert a little influence on the nickel particle size. $LaNiO_3$ type perovskite was prepared by the "self-combustion" method and was used as catalyst precursor for MCD reaction at 873 and 973 K [334]. The results are very attractive for the simultaneous production of CNTs and hydrogen, showing still active after 22 h of reaction at 973 K. Rivas et al. [335] suggested that the good stability of the catalyst derived upon activation of $LaNiO_3$ precursor is mainly due to the ability to stabilize the NiO crystallites in a high dispersion degree on a La_2O_3 matrix, thus limiting the extent of sintering of metallic particles. Besides, La_2O_3 is a good textural promoter or support for the nickel catalysts, which increases the BET surface area and also acts as an electronic promoter [337,338]. The activity and stability of a Raney Fe catalyst is improved by adequate doping of La_2O_3.

CNF as a material itself has also been explored as the support of the MCD catalyst. CNFs are normally mesoporous with a large surface area varying from 100 to 300 m^2/g [281]. Ni supported on various CNFs prepared by MCD over metal catalysts, such as Ni, Ni–Cu, Ni–Fe, Co and Fe–Co on alumina have been applied in the MCD reaction [339–341]. The yield of secondary carbon reached 224 g/g Ni on a Ni/CNF(Ni–Cu) catalyst and 268.5 g/g Ni on a Ni/CNF(Fe–Ni) catalyst, respectively.

Zeolites have been used as the support of the catalyst of MCD reaction [342–345]. Ashok et al. [342] examined the performance of nickel catalyst supported on HY, USY, SiO_2 and SBA-15. The 30 wt.% Ni/HY catalyst showed superior activity and longer life time. The authors attributed the difference to the Ni metal particle size and the acidity of the support. Guevara et al. [343] synthesized mesoporous Ce-MCM-41 catalyst by surfactant-assisted method and showed that the sample is very stable in the MCD reaction. Ziebro et al. [344] employed a Ni/ZSM-5 catalyst for the production of MWCNTs in the relatively low temperature range (673–823 K). The TEM characterization results suggest that at 673 K methane decomposition took place mainly in the channels of the zeolite. However, above 673 K, carbon deposits also on the surface of the catalyst. Jehng et al. [345] investigated the formation of MWCNTs over a Ni/MCM-41 catalyst and discussed the formation mechanism of MWCNTs which follows a tip-growth mode with a nanoscale catalyst particle encapsulated at the tips of the CNTs. Choudhary et al. [54,346] found that the support has a great influence on the morphology of the carbon formed and the CO content in the produced hydrogen stream. No CNFs form on a Ni/H-ZSM-5 catalyst in the tested temperature range, while CNFs grow on a Ni/HY catalyst at 723–873 K.

CeO_2 has been paid attention in MCD reaction because of its ability to promote MSI and metal dispersion. Li et al. [273] tested Ni/CeO_2 catalysts prepared by different methods. Tang et al. [347] employed Fe/CeO_2 for MCD reaction and a catalyst composed of 60 wt.% Fe_2O_3 and 40 wt.% CeO_2 shows the best catalytic activity. However, CO_x is detected in the product from MCD reaction on the CeO_2 supported catalyst which is attributed to the reaction between the lattice oxygen of CeO_2 and carbon deposits. Odier et al. [348] employed a Pt/CeO_2 catalyst for MCD reaction and they attributed the improvement of H_2 production to the spillover of carbonyls from noble metal particles towards the basic hydroxyls groups existing on the partially reduced Ce sites and the reverse spillover of oxygen towards the metal sites to oxidize the carbon formed from MCD. As a consequence, CO_x was detected in the hydrogen stream.

Different substrates, typically Al_2O_3, MgO, or SiO_2, are used as the catalyst support to provide a highly dispersed catalyst surface for SWCNT growth [176,322–324]. Compared to SiO_2 and Al_2O_3, MgO has received much attention. MgO-supported catalysts have been demonstrated to be efficient for SWCNT and DWCNT synthesis and MgO can be easily removed from the carbon product by acid solution without damaging the structure of the CNMs, while removing SiO_2 or Al_2O_3 support materials from carbon product is a laborious task. Li et al. [349] found that porous MgO prepared by thermal decomposition of its salts ($Mg(NO_3)_2$ and $MgCO_3$) is an excellent support material for CVD growth of SWCNTs. After calcination at 1173 K for 12 h, a Fe/MgO catalyst is found to have a uniform $MgFe_2O_4$/MgO solid solution structure which provides numerous active sites after reduction with a diameter of about 4 nm for the growth of SWCNTs and DWCNTs [270]. Ning et al. [350] found a simple approach to achieve a high yield of DWCNT growth by preparing porous and lamella-like Fe/MgO catalysts through hydrothermal treatment. The method reported in their work is also promising in application to the preparation of other metal catalysts supported by hydrophilic oxides. A porous Fe/MgO catalyst was prepared by an ethanol-thermal treatment [351]. This catalyst with sufficiently large pores (50 nm to 5 μm) produces very high quality SWCNTs compared to the previously reported catalysts.

For the applications in the micro-electronics, or the research on the physico-chemical properties at the nanometer level, direct growth of SWCNT on a flat substrate, e.g. on SiO_2/Si wafer, has been reported [352]. Wang et al. [326] prepared bimetallic catalysts such as Fe/Ru and Fe/Pt in the size range of 0.5–3 nm through chemical reduction associated with microwave irradiation on a SiO_2 flat surface. Li et al. [262] prepared Fe–Mo nanoparticles from decomposition of carbonyl complexes. The sizes of the nanoparticles can be varied from 3 to 14 nm by using different protective agents, as shown in Fig. 31. These nanoparticles are precipitated from propanol and redispersed in n-heptane. This solution is dropped or spin coated onto Al_2O_3/Si or SiO_2/Si substrates for SWCNTs growth. Kong et al. [353] reported a strategy for making high-quality individual SWCNTs on silicon wafers patterned with micron-scale islands of catalytic material. The synthesized CNTs are perfect, indi-

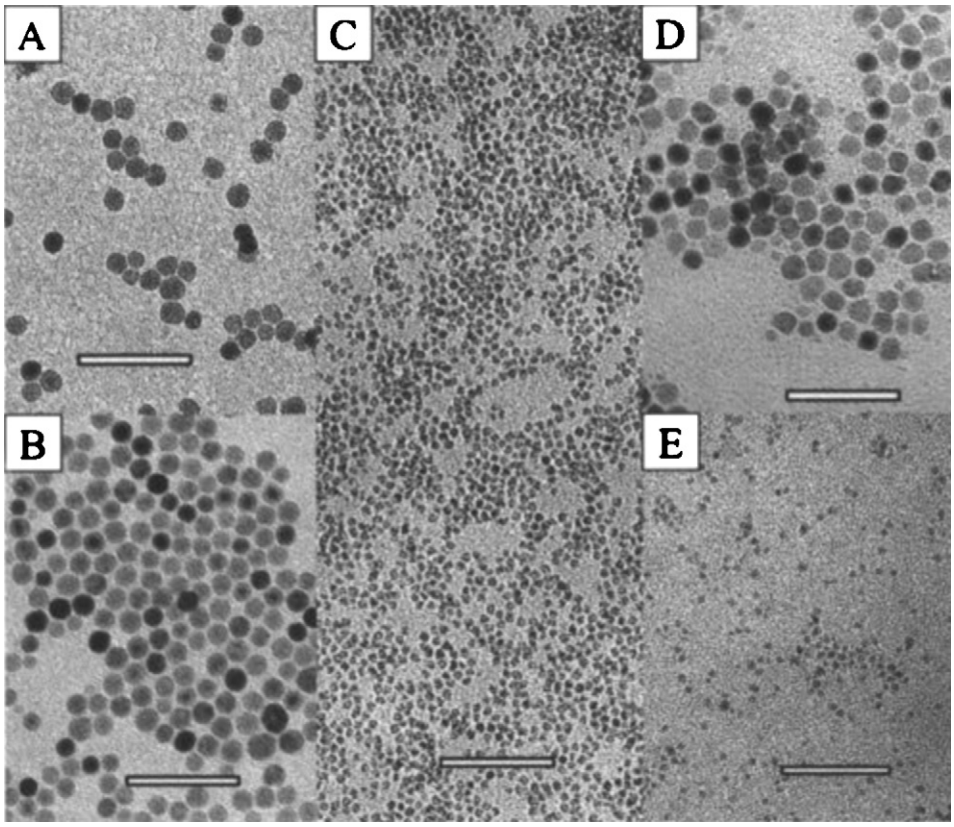

Fig. 31. Fe–Mo nanoparticles synthesized with different protective agents. (A) 1 mmol of octanoic acid. (B) 2.5 mmol of octanoic acid. (C) 1 mmol of octanoic acid and 1 mmol of bis(2-ethylhexyl) amine. (D) 1 mmol of bis(2-ethylhexyl) amine. (E) 2.5 mmol of bis(2-ethylhexyl) amine. The scale bars in all the figures are 100 nm.
Reprinted from [262] with permission of the American Chemical Society.

vidual SWCNTs with diameters of 1–3 nm and lengths up to tens of microns. Some of the SWCNTs bridge two metallic islands, as shown in Fig. 32, providing the prospect of using this approach to develop an ultrafine electrical interconnect and other devices.

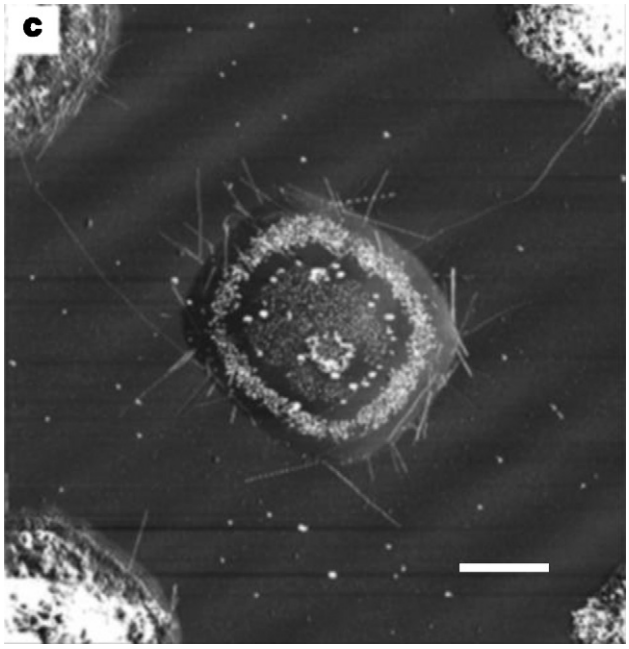

Fig. 32. Carbon nanotubes grown from the patterned islands and bridging between islands (AFM image, scale bar: 2 μm).
Reprinted from [353] with permission of Macmillan Publishers Ltd.

3.5. Catalyst preparation

Catalysts prepared by different methods have different particle size, phase distribution, MSI and therefore exhibit also different catalytic performance. Various preparation methods, such as deposition–precipitation [273,354], impregnation [273,355], reverse impregnation [254,300,356–358], sol–gel [142,359–362], coprecipitation [146,300,356,358,363], mechano-chemical activation [311] and fusion [225,256,300,306,356,358,364,365] techniques have been examined for producing active and stable catalysts for MCD reaction.

In general, catalysts prepared by impregnation and deposition–precipitation have weak interaction between metal and support, and these methods are suitable for the preparation of low metal loading catalysts (e.g. <20 wt.%). Li et al. [273] examined the Ni/CeO_2 catalyst with loading 10 wt.% Ni prepared with different techniques, and showed that at 773 K, the catalysts prepared by impregnation and deposition–precipitation exhibit much higher hydrogen formation rate than that prepared by a coprecipitation method. Further characterization revealed that the catalyst from coprecipitation has a strong MSI due to the formation of Ni–O–Ce solid solution.

Sol–gel technique also has been employed to prepare low metal loading catalyst, especially for the works aimed at synthesizing thin diameter MWCNTs and SWCNTs [142,359,360]. This method also facilitates a strong MSI. For example, Ni–Al and Co–Al catalysts prepared by sol–gel method are difficult to reduce and composed of spinel-like phases [142,360]. Piao et al. [142] prepared an alumina supported nickel aerogel catalyst, which has a large surface area, a high porosity and ultra-low-density, with a sol–gel and subsequent supercritical drying method. After reduction, metal particles

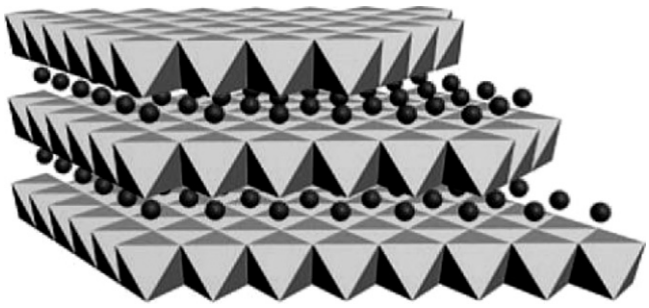

Fig. 33. Schematic diagram of the three-dimensional structure of hydrotalcite-like compounds. The gray blocks represent the brucite layer, which composes densely packed double layer of hydroxyl anions and metal cations locating in the octahedral sites of the double layers. The black balls illustrate the compensation anions and water molecules. This structure allows a uniform distribution of the metal cations. Reprinted from [375] with permission of Wiley-VCH Verlag GmbH&Co.

smaller than 10 nm were obtained. The carbon formed with this catalyst has a curved, hollow, and tubular conformation, with diameters in the range of 10–20 nm.

High metal loading catalyst is favorable for the purpose of hydrogen and CNFs production, on which high methane conversion can be achieved and low CO_x concentration in the hydrogen stream can be obtained, due to a tracer amount of oxygen brought in by the catalyst [51,53]. These catalysts have often been prepared with coprecipitation, reverse impregnation, and fusion techniques [146,254,300,301,356,363].

The preparation of Ni-based catalyst with the coprecipitation method has been practiced since 1910s [366]. Feitknecht compound (FC) has been recognized as a good precursor for many catalyst preparations since 1970s, which can be obtained from a coprecipitation process with an extent of purity [319,367–373]. FC is a category of synthesized or natural compound with anionic clay-like layered structure, expressing in a general formula as [374]:

$$[Me_{1-x}{}^{2+}Me_x{}^{3+}(OH)_2]^{x+}(A_{x/n}{}^{n-})\cdot mH_2O \quad (2)$$

In which

$Me^{2+} = Mg^{2+}, Mn^{2+}, Fe^{2+}, Co^{2+}, Ni^{2+}, Cu^{2+}, Zn^{2+}$;

$Me^{3+} = Al^{3+}, Fe^{3+}, Cr^{3+}$;

$A^{2-} = CO_3{}^{2-}, SO_4{}^{2-}, 2(NO_3{}^-, Cl^-, Br^-)$;

Its general structure is shown in Fig. 33 and is composed of the one by one stack of two kinds of layers. One is so called brucite layer composed of densely packed double layers of oxygen and hydroxide ions with metal cations locating at the octahedral sites formed between the double layers. The other is called anionic interlayer composed of anions and water molecules. This structure if well crystallized, allows a random and uniform distribution of bivalent and trivalent metallic ions, sure, following some rules for charge and crystal field balance in a same crystal lattice. The interlayer is highly disordered and the amount of water is a complex function of temperature, water vapor pressure and the nature of the anions present [375].

It also has been long recognized that for a mixed oxide catalyst or a metal catalyst derived from the reduction of a mixed metal oxide, the uniformity of the oxide precursor is crucial for getting a good catalyst performance [376]. The catalyst preparation via FC structured precursor enables the strongest MSI in the reduced catalyst, and this precursor facilitates the formation of precipitate with the maximum uniformity, the manipulation of the composition of the mixed oxide with a high uniformity, and the formation of the large total and metal surface area. Several excellent reviews and books on the application of FCs in catalyst preparation have been published [374,377–382].

FC starts to decompose and loses molecular water from the interlayers in a temperature range of 403–503 K. Then the structure loses hydroxide and carbonate ions as water and CO_2. The brucite-like layers are not destroyed completely even at above 623 K and well-mixed oxides are formed. Alzamora et al. [370] suggested that the mixed oxide thus formed is composed of a nickel oxide phase containing dissolved aluminum ions and an alumina phase containing dissolved nickel ions if the calcination temperature is low (~600 K), while, if the calcination temperature is high (~1000 K), a pure nickel oxide phase plus a $NiAl_2O_4$ phase are formed. Puxley et al. [383] proposed a continuous phase transformation model for the carefully calcined sample which takes the mixed oxide phase as a uniform mixture of NiO and Al_2O_3. They suggested that the phase structure changes from NiO-like to γ-Al_2O_3-like along with the variation of the composition via the gradually filling process of the tetrahedral and the octahedral sites in between the two densely packed oxygen ion layers. The material formed during low temperature calcination shows a substituted nickel oxide structure in which all aluminum ions may occupy octahedral sites and do not form a separate alumina-rich phase. As the increase of the temperature, aluminum ions move gradually into tetrahedral positions in the lattice and finally a true nickel aluminate phase forms. Furthermore, if the aluminum content is high, a separate alumina phase forms. Clause et al. [384] observed that the nickel–aluminum mixed oxide obtained from the decomposition of FC phase was composed of nickel oxides, Ni-doped alumina, and the spinal-like phases. They proposed that a strong interaction exists between these phases, and that the spinal-like phase is responsible for the good dispersion and thermal stability of the nickel oxide.

For the reduction of low temperature calcined samples, Alzamora et al. [370] observed that Ni particle nucleates on the surface of the nickel oxide rich crystallite, meanwhile, aluminum ions diffuse and form an alumina phase. Puxley et al. [383] adopted a structure model for the reduced high metal content catalyst. During reduction, ions in solid media are difficult to diffuse, while, in the formed metal phase, irreducible Al_2O_3 domains distribute randomly in the Ni particle, which leads to a lattice distortion of the metal and the formation of a paracrystalline metal phase, as presented in Fig. 34. The concept of paracrystallinity of metal catalyst was proposed by Hosemann et al. [385] to account for the structure of the α-Fe catalyst for ammonia synthesis, explaining the strain in the metal crystallites and the high activity of them. Time-of-flight neutron diffraction technique confirmed the presence of paracrystallinity in the reduced catalyst [386]. Doesburg et al. [387] proposed a different model for the reduced nickel–alumina catalyst derived from FCs, in which the catalyst is consisted of a paracrystalline nickel phase supported on a porous alumina support. The alumina phase is highly porous because of the moving away of nickel ions from the mixed oxide phase during the reduction.

In Ni/Al_2O_3 catalysts derived from FCs, a strong interaction exists between Ni and a hard-to-reduce Al_2O_3. The Ni phase is paracrystalline and small equivalent particle size are suitable for MCD reaction [146,216,254,388]. Ni/Al_2O_3 and $Ni–Cu/Al_2O_3$ catalysts prepared by this method show good activity for the reaction in a temperature range of 773–1023 K [146,299]. Li et al. [146] examined Ni–Al catalyst prepared from FC precursors and postulated that the strong interaction between nickel and alumina enhances the activity for the reaction at relatively low temperatures. They noticed that for the well prepared catalyst a linear relationship exists between the yield of CNFs and the nickel content in catalyst, suggesting nickel existing at a same energetic state in different samples.

The calcination of the FC precursor of a Ni/Al_2O_3 catalyst is one of the key steps for getting a good catalyst. Chen et al. [389] recently

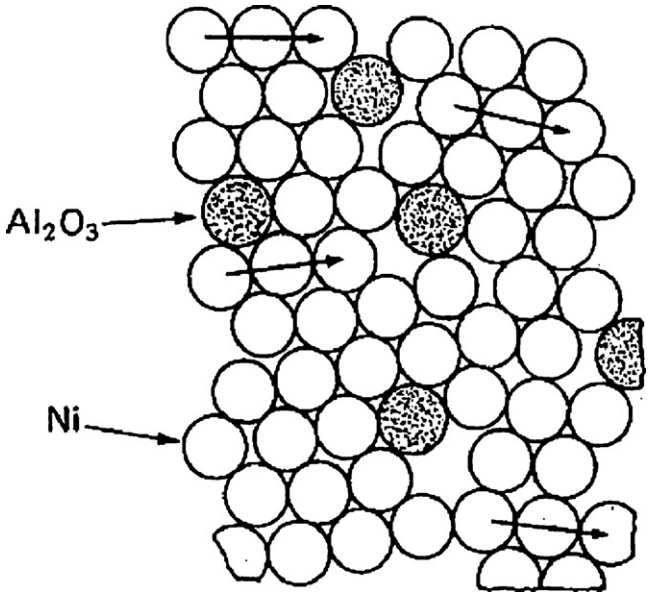

Fig. 34. The illustration of the Ni paracrystallinity. Distortion of Ni lattice cells by the inclusion of irreducible aluminate groups. This distorted structure can be prepared by the reduction of mixed oxide precursors. The model was proposed originally to account for the structure of the α-Fe catalyst for ammonia synthesis.
Reprinted from [383] with permission of Elsevier Science Publishes B.V.

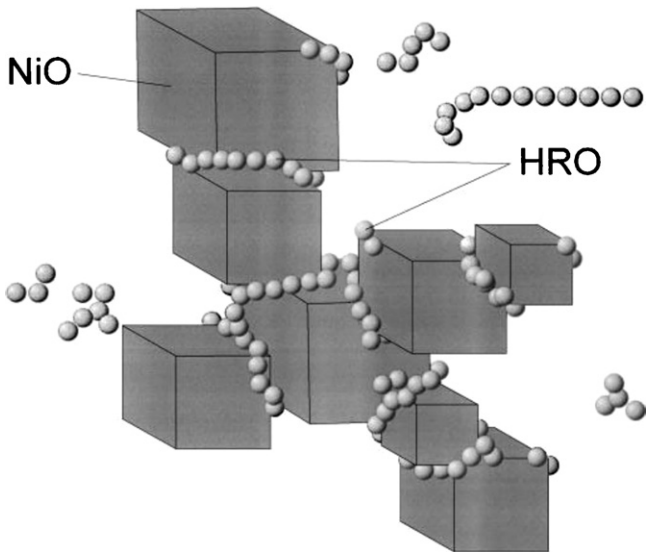

Fig. 35. Hard-to-reduce oxide (HRO) arrangement in the structure of NiO matrix. This model accounts for the stabilization of high metal content catalyst stabilized by a support like alumina.
Reprinted from [356] with permission of Elsevier Science Publishes B.V.

showed that calcination at 573–873 K gives a mixed oxide with only the structural characteristics of the NiO phase, while at 1023 K the calcination results in a segregation of the mixed oxide into NiO and $NiAl_2O_4$ spinel phases. They proposed that Al_2O_3 acts as the diffusion barrier of nickel ion to form NiO crystallites and observed that the average size of NiO crystallite increases with the calcination temperature. The interaction of NiO with Al_2O_3 in NiO–Al_2O_3 and the structure of Ni in Ni–Al_2O_3 become more complex for the samples calcined at high temperatures.

Benito et al. [390] studied the effect of microwave-hydrothermal treatment on the properties of the Co–Zn–Al catalyst obtained by calcination of FC. The results show that the treatment affects the distribution of the cations within the layers of the precursor and also improves the activity and the stability of the Co–Zn–Al catalyst.

Me (Fe, Co, Ni)–MgO–Al_2O_3 catalysts derived from FC compound were employed for the growth of CNTs [391,392]. DWCNTs were prepared by MCD on a Fe/Al/Mg/O catalyst with a iron loading of 1.5 wt.% [391]. Zhao et al. [392] showed that Co/Mg/Al catalyst is selective for the growth of SWCNTs in a fluidized bed reactor. They also prepared a three-dimensional hierarchical nanocomposite consisting of one dimensional CNTs and two-dimensional lamellar flakes (Me–Mg–Al FC compound) [393]. Both the wall thickness and diameter of the CNTs and the composition of the flakes can be easily tuned by changing the proportion of the transition metal in the FC flakes. The obtained nanocomposite was used as a novel structural platform. Zhang et al. [394] prepared CNT array double helices on FC flakes through a novel self organization process during *in situ* CVD growth. The CNTs structure and growth direction are controllable. It was said a novel facile route for building a 3D doublehelix nanoarchitectures by bottom-up self-organization from 1D nanowires/nanotubes and 2D flakes/films.

Ermakova et al. [356] employed a reverse impregnation method to prepare a high Ni loading catalyst. They synthesized NiO first by precipitation followed with drying and calcining. Then Ni^{2+} was impregnated onto the precursor together with ions which form a textural promoter, such as SiO_2, Al_2O_3 and TiO_2. They postulated that with this method, desired particle size of NiO is obtained by treating the material under different conditions and the Ni loading is varied easily. Their structure model of catalyst is illustrated as in Fig. 35. They supposed that the alumina domains distribute in energetically favorable interstice of NiO uniformly and exert a stabilization effect on the NiO particle. With this catalyst, they reported that the yield of carbon increases with the increase of Ni content and reaches the maximum at 90–96 wt.% nickel.

Direct fusion of nitrate salts and subsequent calcination have been employed for preparing high-metal-loading catalyst. This technique avoids the filtration and washing steps. Suelves et al. [300,301,364] compared the Ni–Al and Ni–Cu–Al catalysts prepared by coprecipitation and fusion methods, and showed that the catalyst prepared by fusion is as good as that prepared by coprecipitation.

Bulk catalysts have been also used in MCD reaction. Raney-type catalysts were prepared from Me (Fe, Co or Ni)–Al alloys by leaching out aluminum with a NaOH solution at room temperature, and were used in MCD reaction [302,303,338,395]. The results show that these catalysts are quite good for MCD reaction. Ni and Co catalysts perform better than Fe-base ones and the best results are obtained with Ni and a 30 wt.% ratio in Ni–Al alloy. In [302], Cu doped Raney Ni was investigated and excellent result was obtained when Cu–Ni Raney-metal was thermally treated *in situ* at 873 K. Li et al. [396] prepared nickel oxide with controlled crystallite size and fibrous morphology through precipitation of nickel oxide from nickel acetate with the mediation of ethylene glycol. The morphology of the NiO prepared with this method can be controlled to be spherical, fibrous, or nanorodic. In particular, the nickel hydroxide precipitated in ethylene glycol at 393 K is α-$Ni(OH)_2$ with a FC structure. This precipitate was further calcined and reduced at 773 K. The catalyst showed a good performance with an activity and carbon yield comparable to that of the supported nickel catalysts. Zhang et al. [397] investigated the effect of the rinsing solvent for the precipitate on the Ni catalyst in MCD reaction. Nickel hydroxide precipitates rinsed by ethanol leads to the formation of nanosheet and needle-like NiO, while those rinsed by deionized water leads to the formation of pure nanosheet NiO. The Ni catalysts generated from nanosheet-NiO exhibited relatively higher catalytic activity towards MCD reaction, whereas the catalyst obtained from needle-like-NiO showed very low activity in the same reaction. Jana et al. [398] prepared an unsupported cobalt catalyst by using the Pechini

method. Their results showed that the increase of the Co:citric ratio results in a larger size of Co_3O_4 crystallite, which needs a slightly higher temperature to reach total reduction under H_2.

In general, impregnation, reverse impregnation, and deposition–precipitation lead to a weak MSI, while sol–gel, coprecipitation and fusion methods facilitate a strong MSI. Anyhow, each method has optimum condition and does not guarantee repeatability by itself. However, it has been proved that MSI has strong effects on the activity and stability of the catalyst, and a strong interaction favors the formation of small metal particles even for high reduction temperatures. On the other hand, a catalyst with a weak MSI is easy to reduce and can be a good catalyst under specific conditions.

4. Reaction kinetics and reactor design

4.1. Reaction kinetics

The kinetics of MCD reaction has been studied extensively over the past four decades. Major works have been summarized in Table 4 [186,229,399–406].

Demicheli et al. [399] supposed that the active site is an ensemble of adjacent nickel atoms, and used the following mechanism to describe the MCD reaction on the active site S:

$$CH_4 + nS \Leftrightarrow CH_4S_n \tag{3}$$

$$CH_4S_n \Leftrightarrow CH_3S_n + HS \Leftrightarrow \cdots \Leftrightarrow CS_{n-4} + 4HS \tag{4}$$

$$CS_{n-4} \Leftrightarrow C + (n-4)S \tag{5}$$

$$HS \Leftrightarrow \frac{1}{2}H_2 + S \tag{6}$$

with assuming the adsorption of methane as the rate-determining step, Langmuir–Hinshelwood type rate equation was obtained as:

$$r = \left(\frac{k(p_{CH_4} - p_{H_2}^2)/K_e}{(1 + K_H p_{H_2}^{0.5})^n} \right) \tag{7}$$

where r is the reaction rate, k the rate constant of CNF growth, K_e the thermodynamic equilibrium constant of the overall reaction, K_H the equilibrium constant of hydrogen adsorption, p_{CH_4} the partial pressure of CH_4 and p_{H_2} the partial pressure of H_2. When n equals to 7, this model fits the experimental data well and results in an activation energy of 88.2 kJ/mol. The authors also constructed a deactivation kinetic model considering the effect of reaction condition on the decay of the activity. They found that the deactivation rate increases as the increase of the reaction temperature, and is proportional to $p_{CH_4}/p_{H_2}(p_{CH_4} > 4\,\text{kPa})$. They obtained a deactivation energy of 234 kJ/mol by plotting $\ln k_d$ against $1/T$ (k_d is specific constant for the rate of deactivation reaction).

Kuvshinov et al. [407] applied the model proposed by Demicheli et al. [399], and found that it matches with the experimental data well if takes $n = 7$. The applicability of the Langmuir–Hinshelwood equation suggests them to propose that the competition between the dissociative adsorption of H_2 and methane are the rate-determining steps for CNFs formation if the catalyst deactivation is negligible. For the deactivation kinetics, they proposed that the decrease rate of the active site portion which is active for methane dissociation on the growth surface center is proportional to the production of CNFs and the square power of the maximum formation rate of CNFs. They defined a deactivation rate constant and derived a deactivation energy value of 99 kJ/mol.

Snoeck et al. [186] investigated the kinetics of MCD reaction on a commercial steam reforming catalyst. They examined the possible reaction pathways, the rate-determining steps, and built 80 different rate equations. However, only one equation fits the experimental data well and satisfies the kinetic criteria. The mechanism adopted is as:

Surface reactions:

$$CH_4 + S \Leftrightarrow CH_4 - S, \quad K_{CH_4} \tag{8}$$

$$CH_4 - S + S \Leftrightarrow CH_3 - S + H - S, \quad \text{rds}/k_M^+ \text{ and } k_M^- \tag{9}$$

$$CH_3 - S + S \Leftrightarrow CH_2 - S + H - S, \quad K_3 \tag{10}$$

$$CH_2 - S + S \Leftrightarrow CH - S + H - S, \quad K_4 \tag{11}$$

$$CH - S + S \Leftrightarrow C - S + H - S, \quad K_5 \tag{12}$$

$$2H - S \Leftrightarrow H_2 + 2S, \quad \frac{1}{K_H} \tag{13}$$

Dissolution/segregation

$$C - S \Leftrightarrow C_{Ni,f} + S \quad \frac{1}{K_c} \tag{14}$$

Diffusion of carbon through nickel

$$C_{Ni,f} \Leftrightarrow C_{Ni,r} \tag{15}$$

Precipitation/dissolution of carbon

$$C_{Ni,r} \Leftrightarrow C_w, \quad K_w \tag{16}$$

The rate-determining step in this model is the abstraction of the first hydrogen atom and the formation of a methyl group, i.e. Eq. (9), as a consequence, the rate is expressed as

$$r = \frac{k_M^+ \cdot K_{CH_4} \cdot p_{CH_4} - (k_M^{-'}/K_r'') \cdot p_{H_2}^2}{\left(1 + (1/K_r'') \cdot p_{H_2}^{3/2} + K_{CH_4} \cdot p_{CH_4}\right)^2} \tag{17}$$

in which,

$$k_M^{-'} = k_M^- \cdot k_M^{1/2} \tag{18}$$

$$K_r'' = \frac{K_3 K_4 K_5}{K_H^{3/2} K_c c_{C,(Ni,f)}} \tag{19}$$

In these equations, $c_{C,(Ni,f)}$ (mol C/m^3 Ni) is the concentration of carbon dissolved in nickel at the front of the particle, just below the selvedge (gas side), k_M^- and k_M^- are the rate constants of the forward and the reverse reactions of the rate-determining step, K is a symbol used for equilibrium coefficients, and p_i is the partial pressure of component i.

Latorre et al. [408] employed a phenomenological kinetic model to analyze the experimental results obtained with a Ni–Mg–Al catalyst during MCD reaction. This model takes into account the main stages involved: methane decomposition, metal surface carburization, carbon diffusion, CNT nucleation and growth, and fits well with the data obtained at several operating conditions.

Otsuka et al. [187] performed a hydrogen–deuterium exchange experiment over a Ni/SiO_2 catalyst, with CH_4 and CD_4 as reactants. They found that the reaction rate of CH_4 is higher than that of CD_4 due to the isotopic effect. When the temperature is below 773 K, no CH_3D, CH_2D_2, and CHD_3 are formed with a feed of CH_4 and CD_4 in a ratio of 1:1. Only a small amount of CH_3D, CH_2D_2, CHD_3 are produced with a CH_4 and CD_4 feed ratio of 1:3 and above 773 K. This indicates that the dissociations of CH_3, CH_2, or CH could not be the rate controlling steps. Otherwise, considerable amount of CH_3, CH_2, or CH groups would stick on the catalyst surface. Because the regrouping of CH_{4-n} and D and CD_{4-n} and H are very fast, high concentrations of CH_3D, CH_2D_2, and CHD_3 should consequently be produced. As a result the first C–H bond dissociation of methane is assumed as the rate-determining step [186,399].

Different from the above mentioned works, Zein et al. [401] studied the kinetics of MCD reaction on a Ni/TiO_2 catalyst and suggested that the adsorption of methane on the surface of catalyst

Table 4
Summary of reported mechanism and kinetics research results on supported metal catalysts.

References	Experimental conditions		Mechanism and rate equation	Conclusive remarks of the authors
Demicheli et al [399]	Catalysts	$Ni/CaO–Al_2O_3$	$CH_4 + nS \Leftrightarrow CH_4 \cdot S_n$ $CH_4 \cdot S_n \Leftrightarrow CH_3 \cdot S_{n-1} + H \cdot S$ $\Leftrightarrow \ldots \Leftrightarrow C \cdot S_{n-4} + 4H \cdot S$ $C \cdot S_{n-4} \Leftrightarrow C + (n-4) \cdot H$ $\frac{1}{2}H_2 + S \Leftrightarrow H \cdot S$ $r = k(p_{CH_4} - p_{H_2}^2/K_e)/(1 + K_H p_{H_2}{}^{0.5})^n$	1. The adsorption of CH_4 on an ensemble of nickel atoms is rate-determining step 2. Proved that $n = 7$ is the best estimate 3. The results show that the deposited carbon has a poisoning effect on the carbon formation reaction. The deactivation rate depends on the operating conditions. It increases when the temperature increases and there is a linear relationship with the ratio p_{CH_4}/p_{H_2}
	Particle size	Smaller than 0.8 mm		
	Temperature	838–938 K		
	Pressure	Atmospheric pressure		
	Reactor	Thermo gravimetric		
	Velocity	0.43–1 mol h^{-1}		
	Feedstock	CH_4–H_2 mixture diluted with N_2		
	Method	NA (data not available)		
Alstrup and Taveres 1993 [229,400]	Catalyst	Ni/SiO_2 (20 wt.% Ni) Ni–Cu/SiO_2 1% Cu + 99% Ni 10% Cu + 90% Ni	$H_2 + 2S \Leftrightarrow 2H \cdot S$ $CH_4 + 2S \Leftrightarrow CH_3 \cdot S + H \cdot S$ $CH_3 \cdot S + S \Leftrightarrow CH_2 \cdot S + H \cdot S$ $CH_2 \cdot S + S \Leftrightarrow CH \cdot S + H \cdot S$ $CH \cdot S + S \Leftrightarrow C \cdot S + H \cdot S$ $CS + ss1 \Leftrightarrow C_{b1} + S$ $C_{b1} + ss2 \Leftrightarrow C_{b2} + ss1$ $C_{b2} + ws \Leftrightarrow C_w + ss2$ $r = k_2(p_{CH_4}\theta*^2 - \frac{1}{K_2}\theta_{CH_3}\theta_H)$ $\theta_{CH_3} = \frac{a_H{}^3}{K_3K_4K_5}\theta_C$ or $r = k_3(\theta_{CH_3}\theta* - \frac{1}{K_3}\theta_{CH_2}\theta_H)$ $\theta_{CH_3} = \frac{K_2}{a_H}p_{CH_4}\theta*$ $a_H = K_1^{1/2}p_{H_2}{}^{1/2}$	1. A Grabke-type model based on a rate-limiting dissociative chemisorption step and stepwise dehydrogenation of the chemisorbed methyl gives good agreement with the experimental rates for the Ni/SiO_2 catalyst 2. The rate of carbon formation on the NiCu catalyst with 1% Cu is higher than the rate on the Ni catalyst 3. The rates for the 10% Cu catalyst is much lower than the rate on the Ni catalyst
	Particle size	Small cylindrical pellets with 4 mm diameter and 4 mm length		
	Temperature	723–863 K		
	Pressure	The partial pressures of CH_4 and H_2 were varied independently in the ranges 20–80 kPa and 5–15 kPa, respectively		
	Reactor	Microbalance		
	Velocity	0.9 mol/h		
	Feedstock	CH_4–H_2 mixtures		
	Method	NA		
Snoeck et al. [166]	Catalyst	ICI 46-9P steam reforming catalyst 15 mg	$CH_4 + S \Leftrightarrow CH_4 \cdot S$ $CH_4 \cdot S + S \Leftrightarrow CH_3 \cdot S + H \cdot S$ $CH_3 \cdot S + S \Leftrightarrow CH_2 \cdot S + H \cdot S$ $CH_2 \cdot S + S \Leftrightarrow CH \cdot S + H \cdot S$ $CH \cdot S + S \Leftrightarrow C \cdot S + H \cdot S$ $H_2 + 2S \Leftrightarrow 2H \cdot S$ $CS \Leftrightarrow C_{Ni,f} + S$ $C_{Ni,f} \Leftrightarrow C_{Ni,r}$ $C_{Ni,r} \Leftrightarrow C_w$ $r = \frac{k_M^+ K_{CH_4} p_{CH_4} - (k_M^{'}/K_r^{''}) p_{H_2}^2}{(1 + (1/K'') p_{H_2}^{3/2} + K_{CH_4} p_{CH_4})^2}$	1. The rate-determining step is the abstraction of the first hydrogen atom from molecularly adsorbed methane with the formation of an adsorbed methyl group 2. Formation of filamentous carbon involves the dissolution of adsorbed surface carbon atoms into the nickel particles, diffusion to the rear, and finally precipitation at the support side. The difference in chemical potentials between the gas phase and carbon filament, results in different solubility at both sides of the nickel particle, and creates a driving force for the diffusion of carbon through the metal
	Particle size	NA		
	Temperature	773–823 K		
	Pressure	The partial pressure of CH_4 is in 1.5–10 bar The partial pressure of H_2 is in 0–1.65 bar		
	Reactor	Electro balance		
	Velocity	2.5 mol/h		
	Feedstock	CH_4–H_2 mixtures		
	Method	Differential method		
Kuvshinov et al. [407]	Catalyst	$Ni–Al_2O_3$(90 wt.%Ni)	$CH_4 + nS \Leftrightarrow CH_4 \cdot S_n$ $CH_4 \cdot S_n \Leftrightarrow CH_3 \cdot S_{n-1} + H \cdot S$ $\Leftrightarrow \ldots \Leftrightarrow C \cdot S_{n-4} + 4H \cdot S$ $C \cdot S_{n-4} \Leftrightarrow C + (n-4) \cdot H$ $\frac{1}{2}H_2 + S \Leftrightarrow H \cdot S$	1. Rate of CNF formation in the absence of catalyst deactivation is limited by the dissociative adsorption of methane and can be described by the Langmuir–Hinshelwood equation which accounts for the competitive dissociative adsorption of H_2 2. For the particular composition and reaction temperature, rate of decrease of the active site portion on the growth center surface is proportional to the amount of CNF formed per unit mass catalyst and the square power of the maximal rate of CNF formation with time under these conditions 3. Maximum amount of CNF, formed for the particular feed composition and reaction temperature, is inversely related to the maximum rate of CNF formation under these conditions
	Particle size	NA		
	Temperature	763–863 K		
	Pressure	Atmospheric pressure partial pressures of CH_4 0–40%		
	Reactor	A flow vibrofluidized bed catalyst micro reactor		
	Velocity	NA		
	Feedstock	CH_4–H_2 mixtures		
	Method	NA		
Wang et al. [404]	Catalyst	$Ni_{0.5}Mg_{0.5}O$ 0.25 g	$CH_4 + 2S \Leftrightarrow CH_3 \cdot S + H \cdot S$ $CH_3 \cdot S + S \Leftrightarrow CH_2 \cdot S + H \cdot S$ $CH_2 \cdot S + S \Leftrightarrow CH \cdot S + H \cdot S$ $CH \cdot S + S \Leftrightarrow C \cdot S + H \cdot S$ $2H \cdot S \Leftrightarrow H_2 + 2S$ $r = k_M^+ \left(p_{CH_4}\theta*^2 - \frac{p_{H_2}^2 \theta_C \theta*}{K_1K_2K_3K_4K_5^2} \right)$	1. The rate-determining step is the abstraction of the first hydrogen atom from adsorbed methane 2. By using least square method, the reaction rate was calculated, and a model of powder function for the reaction kinetic equation was established, and through calculations based upon this equation, it was acquired that the reaction order of CH_4 and H_2 was 1.32 and -1.41, respectively, and the activation energy E_a was 172 kJ/mol
	Particle size	0.3–0.45 mm		
	Temperature	813–913 K		
	Pressure	NA		
	Reactor	Fixed-bed reactor		
	Velocity	$2.0–9.0 \times 10^4$ ml/h		
	Feedstock	CH_4–H_2 mixtures		
	Method	Least square method		

Table 4 (*Continued*)

References	Experimental conditions		Mechanism and rate equation	Conclusive remarks of the authors
Zein et al. [401]	Catalyst	Ni/TiO_2 (13 wt.%Ni)	$CH_4 + S \underset{k_{-1}}{\overset{k_{+1}}{\Leftrightarrow}} CH_4 \cdot S$ $CH_4 \cdot S + S \underset{k_{-2}}{\overset{k_{+2}}{\Leftrightarrow}} CH_3 \cdot S + H \cdot S$ $CH_3 \cdot S + S \underset{k_{-3}}{\overset{k_{+3}}{\Leftrightarrow}} CH_2 \cdot S + H \cdot S$ $CH_2 \cdot S + S \underset{k_{-4}}{\overset{k_{+4}}{\Leftrightarrow}} CH \cdot S + H \cdot S$ $CH \cdot S + S \underset{k_{-5}}{\overset{k_{+5}}{\Leftrightarrow}} C \cdot S + H \cdot S$	1. The adsorption of methane on the surface is the rate-controlling step 2. The decomposition reaction is of first order with an activation energy of 60 kJ/mol 3. The model developed indicates the volumetric flow rate, catalyst weight, and temperature to be decisive parameters in scale-up considerations and in the extrapolation of laboratory-scale experimental results
	Particle size	0.4–0.5 mm		
	Temperature	823–1173 K		
	Pressure	Atmospheric pressure		
	Reactor	Fixed-bed reactor		
	Velocity	100–450 ml/min		
	Feedstock	CH4–Ar mixtures		
	Method	Integral method		
Narkiewicz et al. [233]	Catalyst	$Fe–Al_2O_3–K_2O–CaO$ 1 g $Fe–Al_2O_3–CaO$ 1 g	$r = k_o \exp\left(\frac{-E_0}{RT}\right) p_{CH_4}$ $C \cdot S \underset{k_{-6}}{\overset{k_{+6}}{\Leftrightarrow}} C_{Ni} + S$ $2H \cdot S \underset{k_{-7}}{\overset{k_{+7}}{\Leftrightarrow}} H_2 + 2S$ $r = \frac{C_T K_1 p_{CH_4}}{1 + K_7^{1/2} p_{H_2}^{1/2}}$	1. The dissociative adsorption of methane is the rate-determining step. In this case, the rate depends on methane pressure, surface area, and surface chemical composition 2. The rate of carbon formation is proportional to that of methane decomposition on the nanocrystalline iron carbide and is proportional to the methane partial pressure.
	Particle size	1.2–1.5 mm		
	Temperature	NA		
	Pressure	NA		
	Reactor	Thermo balance		
	Velocity	NA		
	Feedstock	NA		
	Method	NA		
Zhang and Smith [405]	Catalyst	Co/SiO_2 0.2 g	$CH_4 + 2S \Leftrightarrow CH_3 \cdot S + H \cdot S$ $CH_3 \cdot S + S \Leftrightarrow CH_2 \cdot S + H \cdot S$ $CH_2 \cdot S + S \Leftrightarrow CH \cdot S + H \cdot S$ $CH \cdot S + S \Leftrightarrow C \cdot S + H \cdot S$ $2H \cdot S \Leftrightarrow H_2 + 2S$ $6C \cdot S \rightarrow 6Cp \cdot S$ $r = \frac{k_M^+ \cdot K_{CH_4} \cdot p_{CH_4} - (k_M^{-'}/K'') \cdot p_{H_2}^2}{(1 + (1/K'') \cdot p_{H_2}^{3/2} + K_{CH_4} \cdot p_{CH_4})^2}$	1. A kinetic model of CH_4 decomposition is described by the cluster nucleation model 2. Catalyst deactivation is associated with the competition between encapsulating carbon formation and carbon dissolution/diffusion on the leading face of particle
	Particle size	NA		
	Temperature	773 K		
	Pressure	Atmospheric pressure		
	Reactor	Fixed-bed micro reactor		
	Velocity	185 ml/min		
	Feedstock	$CH_4–H_2–Ar$ mixture		
	Method	Differential method		
Kvande et al. [409]	Catalyst	Ni/Al_2O_3 2–10 mg	NA	1. TEOM is an excellent tool in kinetic studies of the highly dynamic process of CNF growth due to its sensitivity, small gate time, good mass and heat transfer. 2. The activation energy of CNF growth on fresh Ni surfaces is 64.6 kJ/mol, which is similar to carbon diffusion on Ni (1 1 1) surface estimated by DFT method. For the steady-state growth period, activation energy of 92.4 kJ/mol was measured, which is close to the carbon bulk diffusion barrier obtained by DFT calculations
	Particle size	100–145 μm		
	Temperature	773–893 K		
	Pressure	0.34, 0.9, and 3.78 bar		
	Reactor	Tapered-element oscillating microbalance (TEOM)		
	Velocity	100 ml/min (CH_4)		
	Feedstock	CH_4 and Ar mixture		
	Method	Differential operation		
Borghei et al. [406]	Catalyst	Ni-Cu/MgO 15 mg	$CH_4 + 2S \Leftrightarrow CH_3 \cdot S + H \cdot S$ $CH_3 \cdot S + S \Leftrightarrow CH_2 \cdot S + H \cdot S$ $CH_2 \cdot S + S \Leftrightarrow CH \cdot S + H \cdot S$ $CH \cdot S + S \Leftrightarrow C \cdot S + H \cdot S$ $C \cdot S \Leftrightarrow C + S$ $H_2 + 2S \Leftrightarrow 2H \cdot S$ $r = \frac{k_M^+ p_{CH_4} - (k_M^-/K_r) p_{H_2}^2}{(1 + (1/K_r) p_{H_2}^{3/2})^2}$	1. The kinetics study resulted in a model related to the mechanism with the dissociative adsorption of methane in competition with dissociative adsorption of hydrogen 2. The rate-determining step is the adsorption of methane and the activation energy is estimated to be around 50.4 kJ/mol 3. The rate of catalyst deactivation is of second order and it depends upon temperature and partial pressure of methane and hydrogen
	Particle size	50 μm		
	Temperature	823–923 K		
	Pressure	Atmospheric pressure partial pressures of CH_4 6–10% partial pressures of H_2 5–8%		
	Reactor	Fixed-bed micro reactor		
	Velocity	200 ml/min		
	Feedstock	CH_4, H_2 and N_2 mixture		
	Method	Differential operation		

is the rate-determining step. Helveg et al. [154] performed DFT calculation of the activation energy of each step, and found that the carbon atom diffusion on the surface of nickel particles has the largest activation energy, 154 kJ/mol, which is close to the previously measured values 125–145 kJ/mol. Thus, they concluded that the carbon atom diffusion on the surface of nickel particle is the rate-determining step.

Kvande et al. [409] employed a tapered-element oscillating microbalance (TEOM) to investigate the MCD reaction kinetics on a FC-derived Ni catalyst. Based on the deactivation behavior, initial reaction rate and steady state reaction rate are identified, and two consequent activation energy values are obtained. On the fresh Ni surface, the activation energy is 64.6 kJ/mol, which is similar to carbon diffusion on the Ni (1 1 1) surface estimated by a DFT method [223]. For the steady-state growth period, the activation energy is 92.4 kJ/mol, and is close to the carbon bulk diffusion barrier obtained also with the DFT method [410,411]. These authors suggested that the diffusion of carbon atoms on the surface dominates in the initial period, while their diffusion on the reconstructed Ni (1 0 0) subsurface or through supersaturated Ni bulk dominates at the steady state. Table 5 summarizes the activation energy values of MCD reaction obtained in different laboratories. In general, for metal catalysts the values are between 60 and 100 kJ/mol.

Table 5
Some reported activation energy data of methane decomposition on Nickel based catalysts.

Reference	Catalysts	Activation energy
Gilliland and Harriott [403]	Ni/SiO_2	96.1 kJ/mol
Demicheli et al. [399]	Ni/Al_2O_3–CaO	88.2 kJ/mol
Alstrup and Taveres [229]	$Ni_{0.9}Cu_{0.1}/SiO_2$	90 kJ/mol
Snoeck et al. [166]	the ICI 46-9P steam reforming catalyst (Ni-based)	59 kJ/mol
Kuvshinov et al. [407]	High loaded Ni catalysts	97 kJ/mol
Alstrup et al. [402]	Ni/SiO_2	120 kJ/mol
Zein et al. [401]	13 wt.%Ni/TiO_2	60 kJ/mol
Kvande et al. [409]	Ni/Al_2O_3	64.6 kJ/mol (fresh Ni surface); 92.4 kJ/mol (steady-state)
Borghei et al. [406]	Ni–Cu/MgO	50.4 kJ/mol

4.2. Reactors and process operation

Process parameter optimization and reactor design are very important to the commercialization of the MCD reaction [412,413]. Fixed-bed reactor (FBR) has been used extensively for MCD and other hydrocarbon decomposition reactions in laboratory research. Based on the established kinetic models, several researchers analyzed and modeled MCD reaction with a FBR. Kvande et al. [409] analyzed the kinetic data, including initial CNF growth rate, deactivation rate, and carbon yield, as a function of the reaction temperature, total pressure, H_2 partial pressure and residence time, obtained with a TEOM technique. They modeled two kinds of FBRs, i.e. plug flow reactor (PFR) and continuous stirred tank reactor (CSTR) and defined that the most important parameter for process scale-up is the methane residence time. They claimed achieving a successful scale-up of 10,000 times.

The endothermicity of the MCD reaction and the volume expansion of catalyst during reaction make the FBR as an unsuitable choice due to its limited space and insufficient heat transfer. Fluidized bed reactor (FLBR) has sufficient growing space, good mass and heat transfer and is facile for handling the solid particles. Liu et al. [414] are among the earliest ones who used FLBR for the production of CNTs. Since then, FLBR has been used to develop the process in several works [365,415–417]. Recently, several excellent reviews covered the topic of the mass production of CNTs in FLBRs [418–420]. Wang et al. [421,422] used a nano-agglomerated FLBR (NAFLBR) for the production of nanoparticles. They then applied this reactor to the mass production of CNTs in FLBR [422]. The agglomerates of CNTs have a low bulk density and broad size distribution with mean values smaller than 100 μm and can be fluidized when the superficial gas velocity is higher than 0.005 m/s. Yu et al. [423] found that CNTs particles produced in the NAFLBR are sub-agglomerates entangled with each other. Their formation involves the steps like initial fragmentation of catalyst support, sub-agglomerate formation and the expansion of the agglomerates. Fig. 36 shows a sketch of a NAFLBR setup. Pinilla et al. [365] studied the MCD reaction using a NiCuAl catalyst in a pilot scale FLBR. They optimized the gas velocity for the maximization of the reaction rate and facilitation of the fluidization quality. They built up a semi-continuous FLBR producing 60 l h^{-1} of hydrogen and 15 g h^{-1} of CNFs. They found that, high temperature results in a quick catalyst deactivation due to the mismatch of the rates of the carbon atom generation and the diffusion in the metal particles. See et al. [417] investigated the effects of parametric interactions on the CNT yield in FLBR, achieved by using a full factorial design method. Besides the major factors as reaction temperature and time, and the catalyst, the interactions between temperature–time and temperature–catalyst are important both for CNT and carbon yields. Qian et al. [57] employed a two-stage fluidized bed reactor operating with two temperature zones, as illustrated in Fig. 37. During operation, the temperatures at the bottom and the upper stages

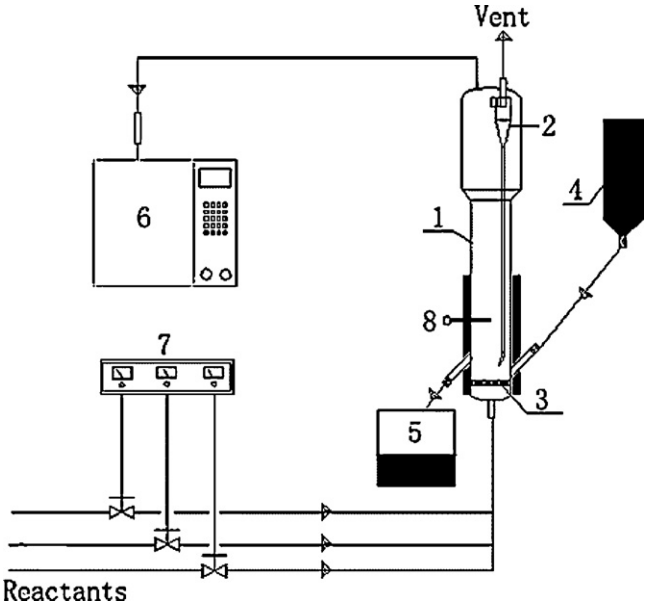

Fig. 36. Schematic diagram of the NAFBR system. 1, reactor; 2, cyclone; 3, gas distributor; 4, catalysts; 5, products; 6, gas chromatography; 7, mass flow controller; 8, thermocouple. The fluidized bed reactor is made of stainless steel, has an I.D. of 196 mm and a height of 1500 mm. A gas distributor inside the reactor is used to achieve a uniform gas flux. With an appropriate gas flow rate, the catalysts can be fluidized.
Reprinted from [423] with permission of permission of Elsevier Science Publishes B.V.

were 773 K and 1123 K, respectively. They found that the catalyst activity and stability are improved significantly over the one stage FLBR.

Ammendola et al. [424] investigated the MCD reaction in a laboratory scale bubbling FLBR. The relative importance of the interparticle and the interphase diffusion processes and that of the intrinsic kinetics of the reaction were assessed. They think that under their operating conditions methane conversion rate is controlled by the intrinsic reaction kinetics. CNFs production in the range of hundreds of grams per day was reported in another work with a FLBR in MCD reaction using a nickel based catalyst [425]. The FLBR can be envisaged as a promising reactor for MCD reaction, allowing the production of large quantity of CNFs with desired structural and textural properties.

The relevance of attrition phenomenon in FLBR has been proposed to be employed as a method to regenerate mechanically the catalyst by removing the carbon deposited on the external surface of the catalytic particles. A model taking into account of the occurrence of different competitive processes, i.e. methane catalytic decomposition, catalyst deactivation due to carbon deposition and

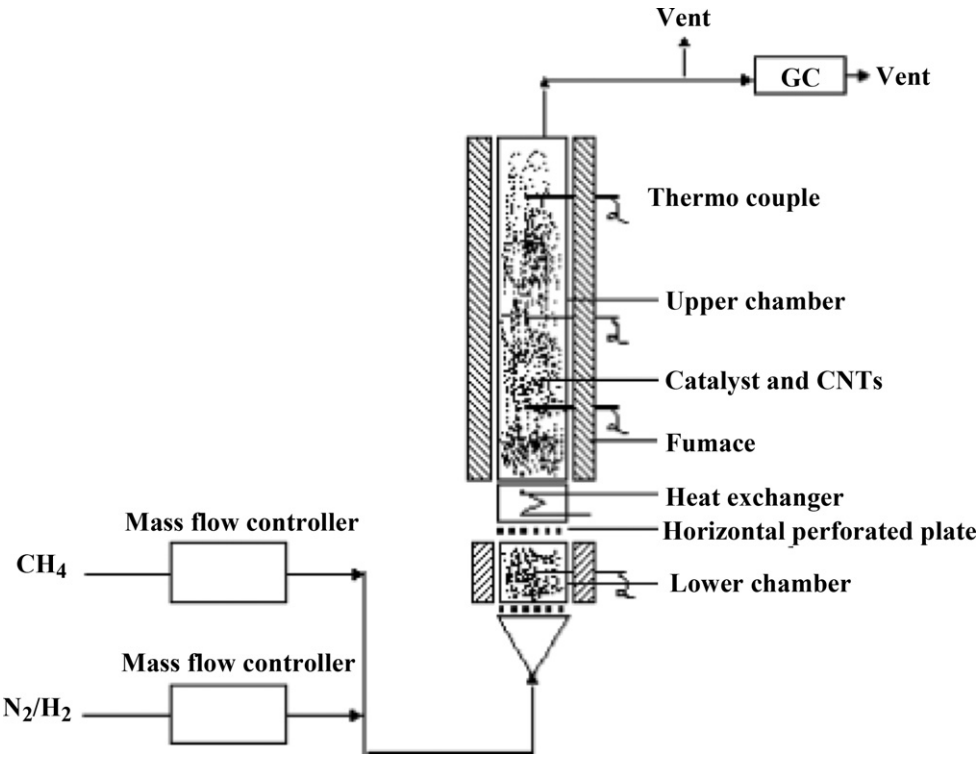

Fig. 37. A schematic diagram of the two-stage fluidized bed reactor for methane decomposition. The reactor is made of stainless steel, with an inner diameter of 40 mm and a height of 1000 mm. A horizontal perforated plate with 10% holes is used to divide the reactor into two stages. This separation prevents the backmixing of gases between stages, but allows the fluidized solid materials to move easily between stages. The height of the lower and upper stage is 150 and 800 mm, respectively. A heat exchanger is adopted (about 50 mm high) between two stages. Thus the temperature of two stages can each be controlled accurately. The temperature of the low stage is fixed at 773 K, while the temperature of the high stage can be controlled from 773 to 1123 K.
Reprinted from [57] with permission of the Elsevier Science Publishers B.V.

the catalyst reactivation due to abrasion of the carbon was built by Ammendola et al. [426]. Their simulation result showed that the attrition phenomenon is helpful to the regeneration of the catalyst. This phenomenon was reconfirmed by the experimental results in other publications [424,427]. However, Shah et al. [416] found that the attrition stimulated regeneration does not exist in their own FLBR experiment.

Qian et al. [415] carried out MCD reaction without pre-reduction of their catalyst, i.e. the reduction was realized after switching on the feed, and observed a good performance of the reaction. They postulated that the simultaneous catalyst reduction provides energy for the endothermic MCD and consumes a part of the hydrogen and carbon formed. Higher conversion of methane was observed in such a process, and the yield of CNTs was about 3–4 times higher than the process carried out with a complete catalyst pre-reduction. While this approach was reported to improve the reaction rate, the CO content in the product hydrogen was also increased. Another group investigated a similar process and detected only trace amount of CO_x during the initial stage of the reaction, and no CO_x at the steady state operation stage was detected [428]. These results may vary with the change of the composition and the amount of the catalyst used. Nevertheless, careful examinations on these processes with different catalyst are necessary.

Kuvshinov and coworkers [283,429–431] examined the production of CNFs from MCD reaction over a 90 wt.% Ni–Al_2O_3 catalyst with various types of reactors. Plug flow FBR, vibrating FLBR with perfect mixing, and moving bed reactor were tested and simulated [429–431]. They also proposed a kinetic model considering catalyst deactivation for MCD reaction, predicting the carbon formation rate and the carbon yield [283,407]. Their results showed that the vibrating FLBR is superior to the other reactor types for the production of CNF. Carbon yield achieves 159 g C/gcat in the vibrating FLBR, which is 1.6 times as high as that in the FBR, and the methane consumption rate reaches 120 l/(h g) at 823 K in the vibrating FLBR [429].

Ishibara et al. [432–434] investigated MCD on a Ni/SiO_2 catalyst in a membrane reactor with 90Pd10Ag (wt.%) alloy tubular membrane, as drawn in Fig. 38. They showed that CH_4 conversion exceeds the equilibrium conversion in a closed system. In particular, the enhancement of CH_4 conversion becomes more significant with the increase of the reaction temperature, since the H_2 permeability through the membrane increases with temperature. The conversion of CH_4 exceeded the equilibrium conversion at 700 K and methane was decomposed completely above 823 K.

Frusteri and coworkers [321,435,436] examined MCD reaction under a quasi-isothermal regime in a reactor with a negligible pressure drop by using a new structured multilayer reactor (MLR) in which Ni or Co thin layer catalysts are installed, as presented in Fig. 39. Chesnokov and Chichkan [311] presented an installation with a rotating reactor for MCD reaction employing an electric motor to rotate the reactor around its axis. Their results show an effective moderation of the CNMs agglomeration and an enhancement of the stability of the catalyst. A Ni–Cu–Fe/Al_2O_3 catalyst was used in this reactor for a prolonged period of time and the concentration of hydrogen at the reactor outlet exceeded 70 mol.%. Pinilla et al. [437] also employed a rotary reactor for MCD reaction. They showed that a rotary bed reactor is a feasible alternative to a FLBR for MCD reaction, giving a higher methane conversion than that in a FLBR and a similar CNF material with textural and structural properties as that obtained in a FLBR.

MCD reaction has been also used in microreactor technology. Martinez-Latorre et al. [438,439] took the advantage of MCD reac-

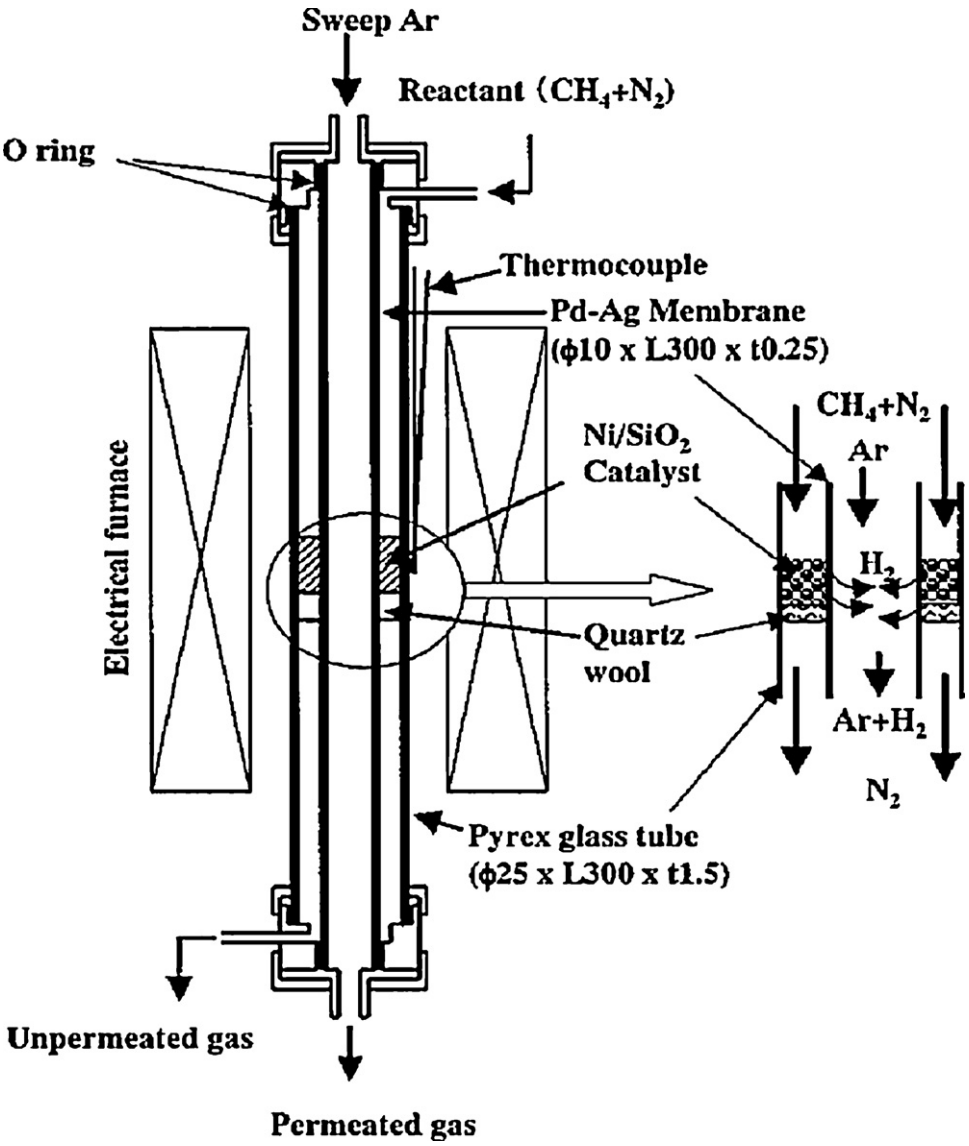

Fig. 38. Schematic view of a membrane reactor used in [434]. CH_4 decomposition was performed in the double tubular reactor. A 25 mm diameter Pyrex glass tube was used as the outside tube, and Pd–Ag alloy (10 mm outer diameter and 250 μm thickness) was used as the inner tube. The catalyst was fixed between the Pyrex glass outside tube and the Pd–Ag alloy inside tube with quartz wool. For the hydrogen permeating membrane, commercial Pd–Ag alloy tubes of compositions Pd/Ag 90:10 and 77:23 (wt.%) (Tanaka Kikinzoku Co. Ltd.) were used without any pretreatment. The Pd–Ag alloy tubes and the outside Pyrex glass tube were fixed in the reactor with nitrile rubber O-rings as shown.
Reprinted from [434] with permission of the American Chemical Society.

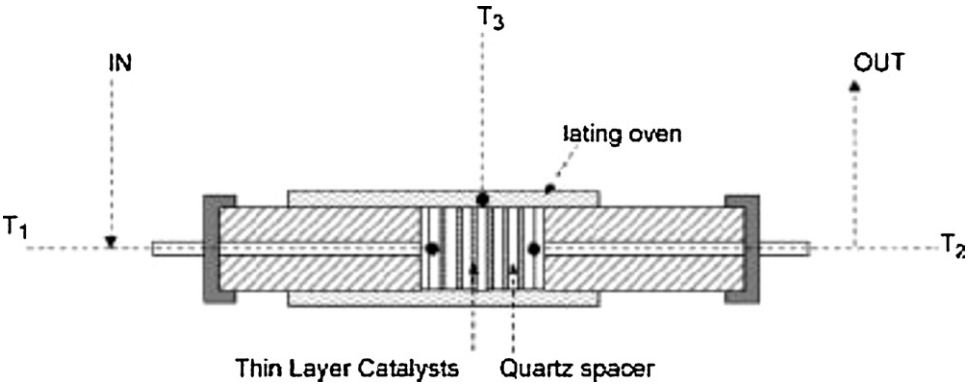

Fig. 39. Sketch of a multilayer reactor (MLR). The reactor consists of a quartz tube (Fint, 39 mm; length, 600 mm) at the ends of which is a metal disc sealed by an O-ring to the quartz tube. Six discs of TLC samples were sandwiched between quartz "spacers" (Fext, 37 mm; thickness, 4 mm) and packed into the reactor. Experiments were carried out at 773, 823 and 873 K, with atmospheric pressure and GHSV ranging from 1900 to 9500 h^{-1} using a 10% CH_4/5% N_2/85% Ar (v/v) reaction mixture flowing in the range of 125–625 stp ml/min.
Reprinted from [435] with permission of Elsevier Science Publishers B.V.

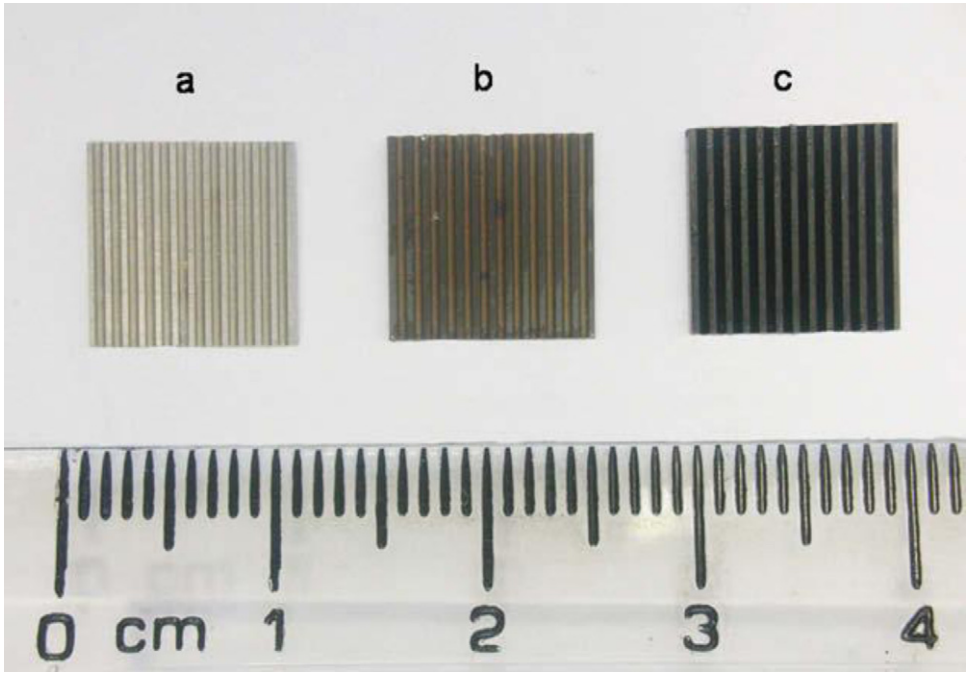

Fig. 40. Microreactor platelets at different stages: (a) blank platelet; (b) platelet after alumina coating and thermal treatment and (c) platelet after CNFs growth. Microreactor is coated with alumina by a wet chemical sol–gel method. Nickel is deposited by ion-exchange from a pH-neutral nickel solution. Subsequently, the coated microreactor is calcined in air at 873 K for 2 h. CNFs are grown on the as-prepared microreactors platelets via MCD reaction.
Reprinted from [439] with permission of Elsevier Science Publishers B.V.

tion in the fabrication of a microreactor. They grew a well attached layer of entangled CNF from MCD reaction on a stainless steel microreactor previously coated with a layer of Ni supported on alumina and believed that the prepared CNF-coated microreactor has good perspectives to be used in an application that is suitable to show the advantages of the association of CNFs as catalyst support in a microreactor (see Fig. 40). Agiral et al. [440] made a microreactor with Ni/Al_2O_3 and nickel thin film catalysts coated inside the closed channels of silica substrate. They obtained a uniform and thin layer of highly porous and mechanically stable CNF-alumina composite with a high surface area (160 m^2/g). They postulated that the microstructured multiphase reactor with high surface area CNFs on the walls is ideal for several critical reactions in some specialty chemicals production.

It is no doubt that fluidized and moving bed reactors are the suitable solutions for large scale production of CNMs from MCD reaction, because the facility of solid particle operation is a necessity [441]. Muradov and Veziroglu [56] discussed the advantages of a FLBR in the aspect of the heat supply and mass transfer, and proposed that if a hydrogen permeation membrane is incorporated with the FLBR reaction system, high-purity hydrogen and facile operation may be achieved for MCD reaction.

5. Methane decomposition as a process

5.1. The purity of hydrogen

The formation of a small amount of CO has been noticed during MCD reaction [346,442]. Since PEMFCs are very sensitive to CO in H_2, the knowledge of CO amount in the product stream and its origin is then crucial. The oxygen may be brought in via the following routes: (a) oxygenic impurities (O_2, H_2O, etc.) in the feed; (b) incomplete metal reduction and partial reduction of the support; and (c) the surface OH groups on the oxide support [442]. By purifying the feed and completing the pre-reduction of metal, Ferreira-Aparicio et al. [442] excluded (a) and (b) but attributed the CO formation to the reforming reaction between methane and the hydroxyl groups on the surface of the support.

The contribution of oxygen on the support to the CO content in hydrogen stream was examined by Choudhary et al. [54,346]. They measured the CO content quantitatively with transforming CO to CH_4 and then using a FID detector. CO content in the hydrogen stream is around 50, 100 and 250 ppm after stabilized for Ni/SiO_2, $Ni/SiO_2/Al_2O_3$ and Ni/HY catalysts, respectively, at 823 K, as shown in Fig. 41. They observed that CO formation rate is high in the initial

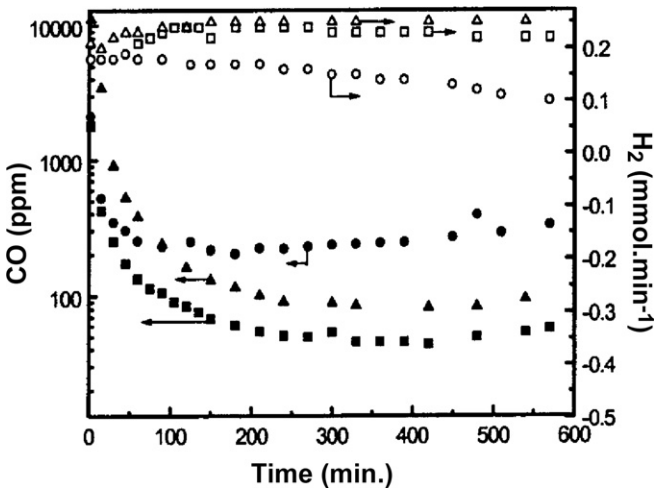

Fig. 41. CO content (solid symbols) and H_2 formation rates (open symbols) on Ni/HY (●, ○), $Ni/Al_2O_3/SiO_2$(■, □) and Ni/SiO_2(▲, △). The effect of the support on the CO content and the rate of hydrogen production is important. The amount of CO in the hydrogen stream is high initially for all the catalysts, but rapidly decreases with time and finally stabilized. The CO content in the hydrogen stream was *ca.* 50 ppm, 100 ppm and 250 ppm for Ni/SiO_2, $Ni/SiO_2/Al_3O_3$ and Ni/HY, respectively, after the CO formation rate is stabilized. The support dependence of the CO content is likely related to the amount/stability of hydroxyl groups present on the support.
Reprinted from [346] with permission of Elsevier Science Publishers B.V.

stage and then decreases rapidly with time and finally stabilizes at a low level. The rate of CO formation increases with the increase of the reaction temperature, reconfirming the result of a previous work [442]. However, the CO content decreases with the increase of the gas space velocity.

Chen et al. [53] estimated the amount of CO formed on a high metal loading Ni–Cu–Al catalyst. By assuming the weight loss of catalyst all due to the dehydration of hydroxyl groups on the surface of alumina, they calculated that the average CO concentration in the hydrogen product is around 9.5 and 6.8 ppm at 873 and 973 K, respectively. It is reasonable that most of CO comes from the interaction between methane and the lattice oxygen or surface OH^- of the oxide support. With this respect, high loading metal catalyst is superior for the production of CO_x-free hydrogen due to its comparably small amount of oxygen content.

5.2. Effect of the feed composition

In a number of reported experimental work, to keep the stability of catalyst or to ease the operation, the process was carried out with diluted methane by Ar, N_2 or He [54,146,279]. The effect of hydrogen in the feed has been also investigated. Li and coworkers [146,147,299] introduced 0.6 vol.% of hydrogen to the reaction feed, and found that hydrogen in the feed prevents the formation of any "carbon nucleus" and fibers growing in the induction stage and lowers considerably the rate of formation of CNFs in the subsequent time period. It is interesting to note that hydrogen is a product of methane decomposition, the strong effect of hydrogen in the feed can only be attributed to its effect during the initiation period of reaction, which prolongs the induction time and increases the activation temperature of catalytic growth of carbon from methane. Their result showed also that the ratio of CH_4/H_2 in the feed has a strong effect on the morphology of carbon formed. There is apparently a shift from filament-like carbon to bamboo-like carbon as the increase of the amount of hydrogen in the feed. Zhang and Smith [443] investigated the effect of the presence of H_2 and CO in the feed, and suggested that the presence of H_2 or CO reduced the net rate of carbon deposition and increased the net rate of carbon removal. Hence, more stable CH_4 decomposition activity was observed on the supported Co catalyst with a low metal loading in the presence of H_2 or CO.

Several groups found that the addition of some unsaturated and aromatic hydrocarbons in the feed have a significant enhancement for the MCD reaction. Qian et al. [444] investigate the decomposition of CH_4 in the presence of C_2H_4 or C_2H_2 using a nanosized iron or nickel based catalyst. They found that the presence of C_2H_4 or C_2H_2 increased the conversion of CH_4 compared to that without C_2H_4 or C_2H_2. They attributed the effect to the facile prior adsorption of C_2H_4 or C_2H_2 and the formation of intermediate products of aromatics or poly aromatics. This enhancement exists with different catalysts, and provides a new alternative for the low temperature activation and decomposition of CH_4. Muradov et al. [87,445] conducted experiments on methane decomposition in binary mixtures with saturated and unsaturated hydrocarbons over inert supports, viz. activated alumina and quartz wool. They found that the addition of small amount of unsaturated hydrocarbon, e.g. ethylene, to methane increases the steady-state concentration of hydrogen in the effluent gas, as present in Fig. 42. They found that the carbon produced from unsaturated hydrocarbons is catalytically more active for MCD reaction as a catalyst than that produced from methane.

Asia et al. [446] investigated MCD reaction in the presence of CO_2 over a Ni catalyst. In the reaction with an 1:1 mixture of CH_4 and CO_2, the formation of CNTs stops because of the small driving force of the reaction (i.e. low gas-phase carbon potential). Dry reforming reaction was observed to proceed which indicates that

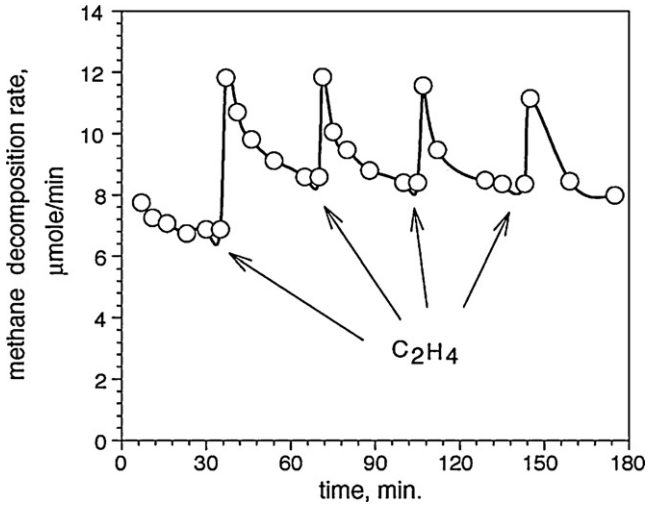

Fig. 42. Effect of ethylene pulses on methane decomposition rate. (Time of purging the reactor with Ar after C_2H_4 pulses is not included in the plot.) This chart demonstrates the accelerating effect of the ethylene-derived carbon on methane decomposition rate. Methane was thermally decomposed (1123 K) over the surface of the activated alumina over a period of 1 h until a quasi-steady state was established. A pulse of ethylene was introduced into the reactor (at the same temperature), followed by rapid and thorough purging of the reactor with an inert gas (for removing gaseous products of ethylene decomposition). Methane was introduced into the reactor, and a sharp increase (spike) in methane decomposition rate was observed, followed by its gradual decline over a period of about half an hour. This procedure was repeated several times, and the effect was almost the same. This experiment indicates that carbon produced from ethylene is catalytically more active towards methane decomposition reaction than carbon produced from methane.
Reprinted from [87] with permission of Elsevier Science Publishers B.V.

the metal particles are not encapsulated by the graphite layers. Therefore, when the mixed feed gas is replaced by pure CH_4, the nickel catalysts still show activity for MCD reaction.

5.3. Comparison with other hydrogen production processes

MCD is a moderately endothermic reaction, and its energy requirement for H_2 production is 37.8 kJ/mol H_2, which is considerably less than that 63.3 kJ/mol H_2 for methane steam reforming process. Hydrogen production from MCD reaction does not emit CO_2, saving extra cost for CO_2 sequestration. The capture and sequestration of CO_2 add about 25–30% to the cost of hydrogen production for the methane steam reforming process. Moreover, MCD reaction is suitable for the production of CO_x-free hydrogen directly usable for low temperature fuel cells.

Stepwise reforming was proposed as an alternative process to simplify the coking suppression effort. The process is composed of two steps, the first is MCD reaction and the second is the regeneration of catalyst with oxidative gases, such as O_2, H_2O and CO_2. Cao et al. [447] compared the processes of stepwise reforming, steam reforming, partial oxidation and autothermal reforming of methane. Stepwise reforming is the most thermal efficient one among those processes. Meanwhile, stepwise reforming process produces the lowest amount of CO_2 per mol of H_2 and has the smallest gas flux per mole CH_4 reformed. These make it a more environmentally benign and energy efficient process.

Muradov and Veziroglu [56,448] performed a techno-economical evaluation of MCD process, and demonstrated that the process economics depends on the price of the carbon product. They proposed that the selling of carbon should make up about 69% of all the cost [37]. The MCD reaction becomes competitive over steam reforming if the carbon-selling price is over $350/ton as shown in Fig. 43. They thought that for the carbon generated from

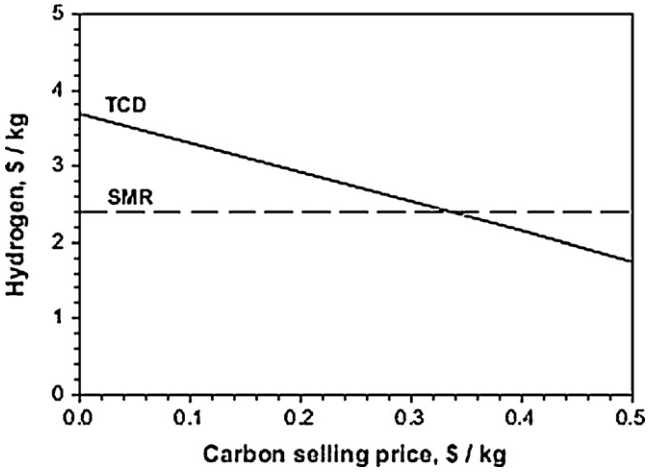

Fig. 43. Hydrogen selling price as a function of carbon-selling price. The carbon produced in the carbon-catalyzed methane decomposition process is a sulfur and ash-free product that could be marketed at high selling price. For example, as a high quality substitute for petroleum coke it could potentially be sold for $310–460/ton (for manufacturing of electrodes in aluminum and ferro-alloy industries. Other forms of carbon, e.g. pyrolytic carbon, carbon black, and carbon nano-fibers) currently are of much greater value.
Reprinted from [448] with permission of Elsevier Science Publishers B.V.

MCD on a carbon catalyst, it is easy to be sold for $310–460/ton. If metal catalysts are used, CNF and CNT can be produced.

van der Lee et al. [449] employed a Ni/SiO_2 catalyst for the production of macroscopic CNF particles (as present in Fig. 44A). The result showed that the bulk density of the CNF particles depends on the metal loading on the catalyst used. Over a 5 wt.% Ni/SiO_2 catalyst low density particles (0.4 g/ml) are obtained, while a 20 wt.% Ni/SiO_2 catalyst leads to a bulk density up to 0.9 g/ml with a bulk crushing strength of 1.2 MPa. The high metal loading catalyst grows CNFs with diameters of 22 nm, and a great irregularity in structure, resulting in a higher entanglement and a concomitant higher density and strength as compared to the thinner fibers (12 nm) grown on the low metal loading catalyst. Chen et al. [450] obtained directly macroscopic CNF particles with a high yield from MCD reaction. The material has good pore size distribution and mechanical strength and is obviously superior to activated carbon if using as catalyst support and adsorbent, as shown in Fig. 44B. Compared to carbon black and activated carbon, CNFs and CNTs are of greater value also as advanced material composite [451–453].

From the data of a recent report [454], the production cost of CNT is about $150/kg for semi-industrial scale production, and is estimated with a mid-term cost target of $45/kg. The market price of activated carbon at the present time is much higher than the target price set by Muradov and Veziroglu. However, the market for the catalytic carbon materials is still very small compared to the demand of hydrogen. This is likely the most important obstacle for MCD to become a commercially important process in near future.

5.4. Processes based on MCD

Stepwise reforming of methane as a process based on MCD attracts the attention of many researchers [75,77,78,455–458]. It involves two distinct steps: (1) methane decomposition on a catalyst and (2) regeneration of catalyst with H_2O, O_2, or CO_2. The process is:

$$(1)\ CH_4 \rightarrow C + 2H_2 \quad (20)$$

$$(2)\ C + H_2O \rightarrow CO_x + H_2 \quad (21)$$

or

$$C + O_2 \rightarrow CO_x \quad (22)$$

or

$$C + CO_2 \rightarrow CO \quad (23)$$

The advantage of regeneration with oxygen or air is the autothermal balance of the MCD and catalyst regeneration reactions. Otsuka et al. [456] investigated the catalytic performance of Ni/SiO_2, Ni/TiO_2, Ni/Al_2O_3 and $Pd–Ni/SiO_2$ catalysts for the cyclic MCD reaction and the partial oxidation of the formed CNFs with O_2.

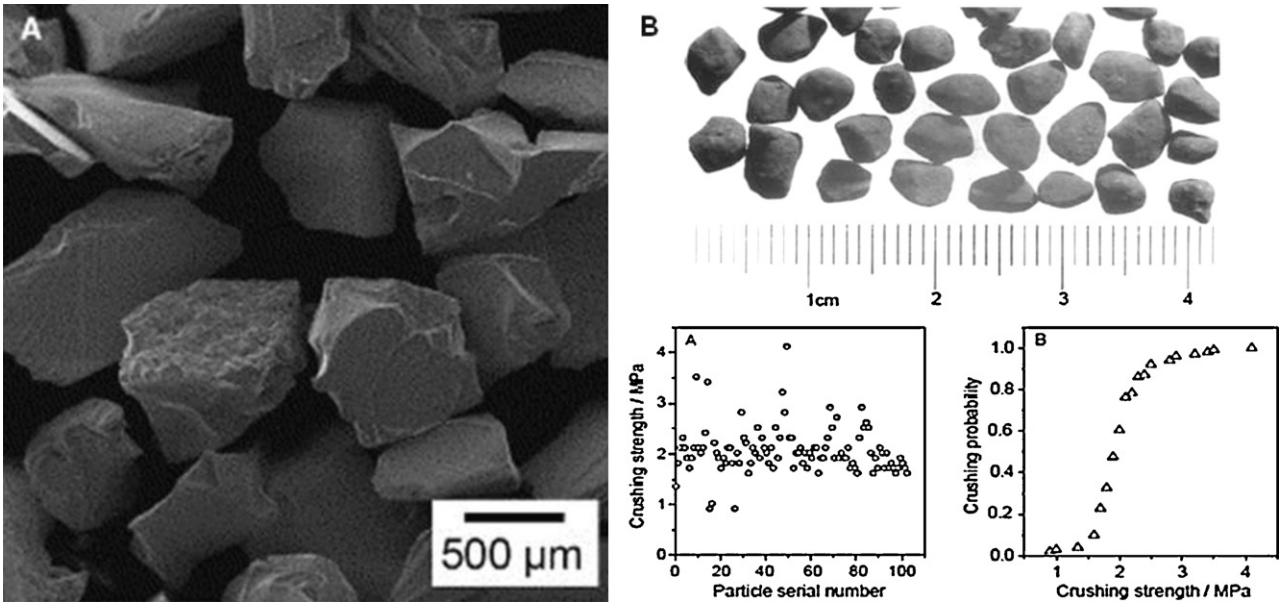

Fig. 44. (A) Low magnification SEM images of CNF grown over 5 wt.% Ni/SiO_2 which was prepared by deposition precipitation method. The catalyst with particle size of 425–850 μm was used for CO disproportionation at 823 K. (B) Photo of millimeter-sized carbon nanofiber granules self-formed during MCD reaction (up) and crushing strength data of the single pellets and crushing probability distribution of the CNF particles (bottom). The mechanical strength and its reliability are better than activated carbon particles derived from wood resources.
Reprinted from [449,450] with permission of Elsevier Science Publishers B.V.

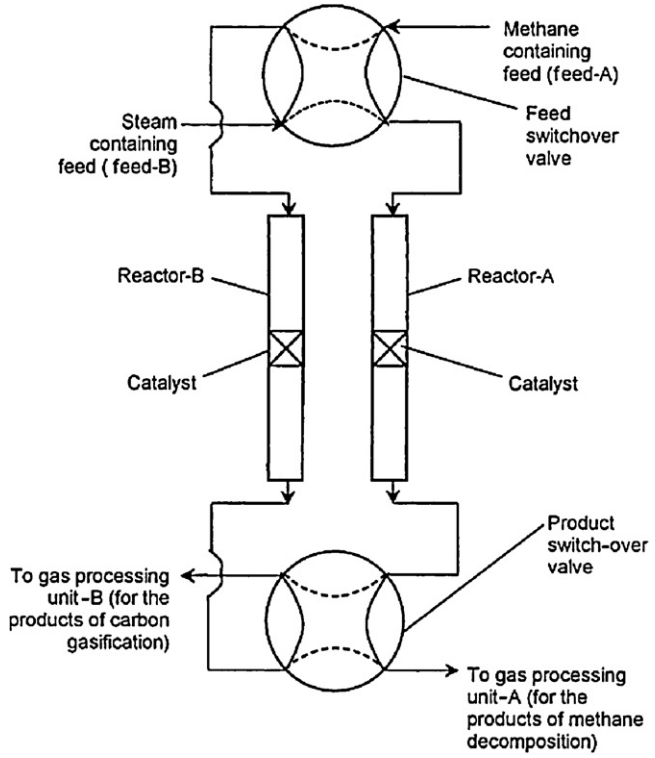

Fig. 45. Schematic presentation of the cyclic process for carrying out the catalytic methane decomposition and carbon gasification reactions simultaneously, in two separate parallel reactors in a cyclic manner by switching two different feeds (feed-A and -B) between the two reactors and also simultaneously switching the two different product streams (between the two separate gas processing units after an interval of time for producing CO-free hydrogen continuously from the decomposition of undiluted methane at higher temperatures (>873 K)).
Reprinted from [77] with permission of Elsevier Science Publishers B.V.

Ni/TiO_2, Ni/Al_2O_3 and $Pd–Ni(1:3)/SiO_2$ catalysts are found promising because their completely lost activity during the precedent MCD reaction can be restored with good repeatability by the oxidation of the formed CNFs with O_2. However, this regeneration method may result in a rapid temperature increase (>60 K), which is very harmful to the operation and the catalyst.

The regeneration of catalyst with steam was examined carefully on purpose to produce CO_2 and H_2 selectively instead of CO and H_2. Choudhary et al. [75,457] investigated this process with a Ni/ZrO_2 catalyst. Their results showed that although high temperature regeneration favors MCD reaction, it is detrimental to carbon gasification by steam. An increase of the surface carbon coverage has a negative effect on the removal of surface carbon. The overall process run optimally in 648–673 K and under this condition the catalyst regains surface carbon coverage. The process was operated in cycles to obtain CO-free hydrogen in step I, with CO < 20 ppm, and also hydrogen in step II containing <0.5% CO. In another work, CO_x-free H_2 close to stoichiometric amount was produced continuously at a constant H_2 production rate by stepwise steam reforming of methane at low temperature in two parallel catalytic reactors operated in cyclic mode [77,78]. Both reactors contained the same Ni catalyst and operated in cyclic manner by switching a methane-containing feed and a steam-containing feed at a prescribed interval of time, as presented in Fig. 45. It showed an optimum value of the feed switchover time exists. Among the different Ni catalyst with different supports including metal oxides ZrO_2, MgO, ThO_2, CeO_2, UO_3, B_2O_3 and MoO_3, and zeolites HZSM-5, HY, HM, NaY, Ce(72)NaY, and Si-MCM-41; Ni/ZrO_2 and Ni/Ce(72)NaY show the best performance in the cyclic process.

Takenaka et al. [458] investigated the cyclic process of coupling MCD reaction and CO_2 gasification of CNFs on a Ni-based catalyst. TiO_2 and Al_2O_3 are excellent supports for the process because the favorable Ni particle size in a range of 60–100 nm for MCD can be obtained. However, because of its highly endothermic nature, regeneration of the catalyst with CO_2 turned out unfortunately to be a very energy intensive process. Li et al. [459] showed that a Ni catalyst is more stable than a Co catalyst during cyclic MCD decomposition-carbon oxidation reactions. Furthermore, removal of the carbon deposited by reaction with CO_2 rather than O_2 significantly decreased the CO contamination of the produced H_2 on the $Ni/Al_2O_3/CeO_2/MgO$ catalyst. However, the carbon removal rate was slower with CO_2 compared to O_2.

Otsuka et al. [460] presented a hydrogen production and storage concept. The first step is MCD on a Ni/SiO_2 catalyst to produce hydrogen, and the hydrogen is used to reduce metal oxides, such as $In_2O_3–Fe_2O_3$ to a stable metal at a certain temperature. When hydrogen is needed, steam is employed to react with the reduced metal. This process produces hydrogen pure enough for low temperature fuel cells. Since metal is easy for carry and transport, this method can be used to produce and store hydrogen for fuel cells.

5.5. Applications of CNMs

The bulk utilization of the CNMs should be crucial for the MCD reaction to become a process of commercial interest, because hydrogen has been consumed in very large volume and is targeted to be consumed in hydrogen energy system with an extremely large volume. If the hydrogen is produced partly with this process, the produced carbon should be consumed with almost the same scale. Actually, high temperature pyrolysis of natural gas has been employed to produce hydrogen and carbon black for quite a long time [280]. Nonetheless, the carbon black has already an appreciably large amount of application in various industries. The application of CNMs as catalyst and catalyst support have been a hot topic, however, the consumption of those materials in such a specialized field cannot make up such a volume [461–464]. When we proposed the idea of simultaneous production of CO_x-free hydrogen and nano-carbon materials [51], the exciting application hypotheses of CNTs as the hydrogen storage material for hydrogen fueled vehicles [53] and the components of high performance composite materials [465] were actively explored. The hydrogen storage dream with SWCNTs failed no sooner after it was proved incorrect both theoretically and experimentally [466–469].

The addition of CNTs into polymers to make high quality composite materials seems successful, and may become a process consuming CNMs with a large enough volume comparable to the volume of hydrogen consumed in chemical industries [63,65]. CNFs and CNTs provide solutions to many challenging problems in composite material applications. Unlike glass fibers, they are electrically conductive and thus are suitable for applications that require the ability to discharge electrostatic potentials, providing sufficient conductivity for electrostatic painting, or even shielding from radio frequency interference or lightening strike [470]. Moreover, thermal conductivity and mechanical strength of the composite materials made with CNFs are excellent.

Tibbettes et al. [470] reviewed the field of CNF/composite material. With careful preparation techniques, tensile strength and modulus of the composite material can be more than triple times that of the neat resin, which was achieved with 15 vol.% CNFs. Electrical conductivity was largely improved with <0.5 vol.% CNFs, while above 15 vol.% CNF loading, a resistivity close to 0.1 Ω cm was achieved. Al-Saleh and Sundararaj [471] focused on the development in CNF/polymer conductive composites. These composites exhibit superior electrical, electromagnetic interference shielding effect and thermal property compared to conventional conductive polymer composites. Breuer and Sundararaj [63] discussed various processing methods for producing nanocomposites such as

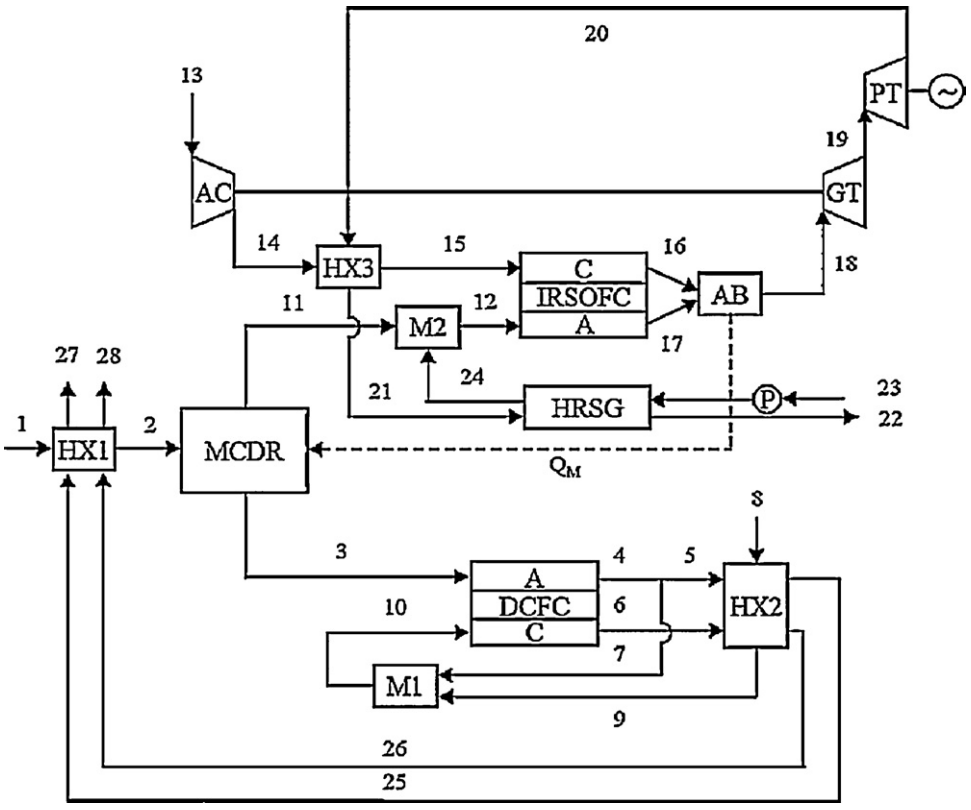

Fig. 46. The flow sheet for an energy conversion system with numbered streams. The major components include a MCDR, a IRSOFC, a DCFC with molten carbonate electrolytes, a catalytic afterburner (AB), an air compressor (AC), a heat recovery steam generator (HRSG), two gas turbines (one (GT) is used to drive the air compressor, and the other one (PT) is used to generate power), a carbon dioxide–air mixer (M1), a steam–gaseous fuel mixer (M2), a methane–DCFC exhaust heat exchanger (HX1), an air–DCFC exhaust heat exchanger (HX2), a gaseous fuel-AB exhaust heat exchanger (HX3), and a pump (P).
Reprinted from [74] with permission of Elsevier Science B.V.

particular melt mixing, solution processing and *in situ* polymerization techniques. They also summarized the important properties of the composite, including mechanical, electrical, thermal, optical and surface properties. Harris [472] reviewed the progress within the field of CNT/ceramic and CNT/metal composite materials. They thought that the quality of the CNTs and the nature of the interface have a strong influence on the properties of the composites.

Steinberg [473] proposed to utilize the carbon from hydrocarbon pyrolysis as the fuel of a DCFC. We think this is an idea which can make both of the products of the MCD reaction meaningful to the energy processes. Liu et al. [74,474] constructed recently an energy conversion system which is composed of a MCD reactor, an IRSOFC and a DCFC, as shown as Fig. 46, and built models to calculate the energy efficiencies of the three major components and

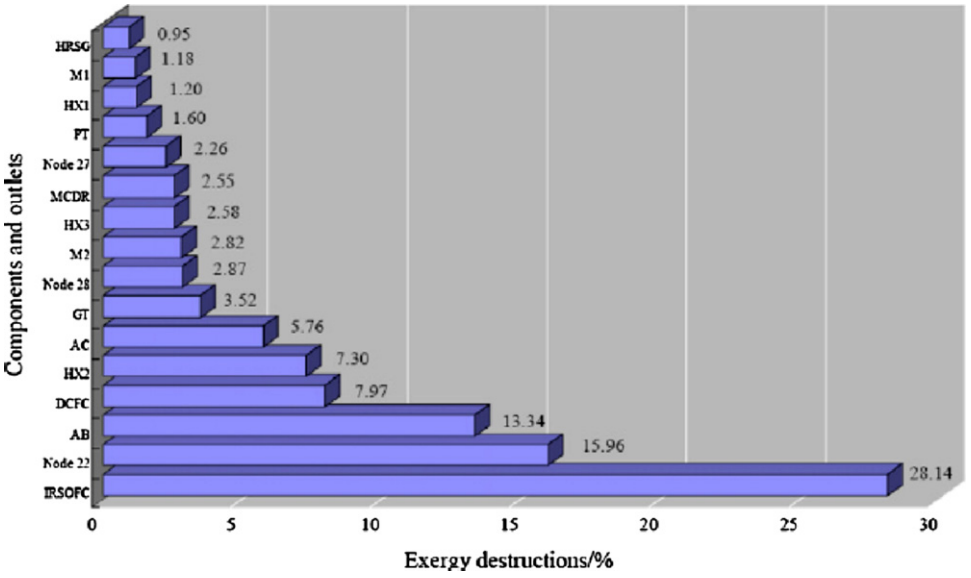

Fig. 47. Exergy destructions in each component and outlet corresponding to those marked in Fig. 45.
Reprinted from [474] with permission of Elsevier Science Publishers B.V.

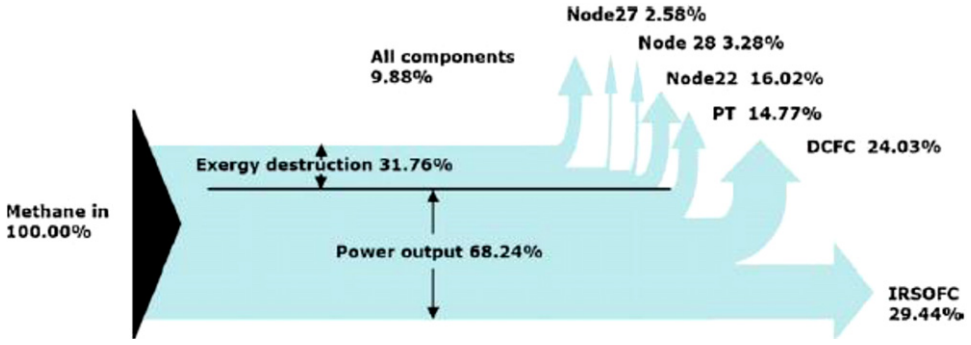

Fig. 48. Exergy flow for the proposed system.
Reprinted from [474] with permission of Elsevier Science Publishers B.V.

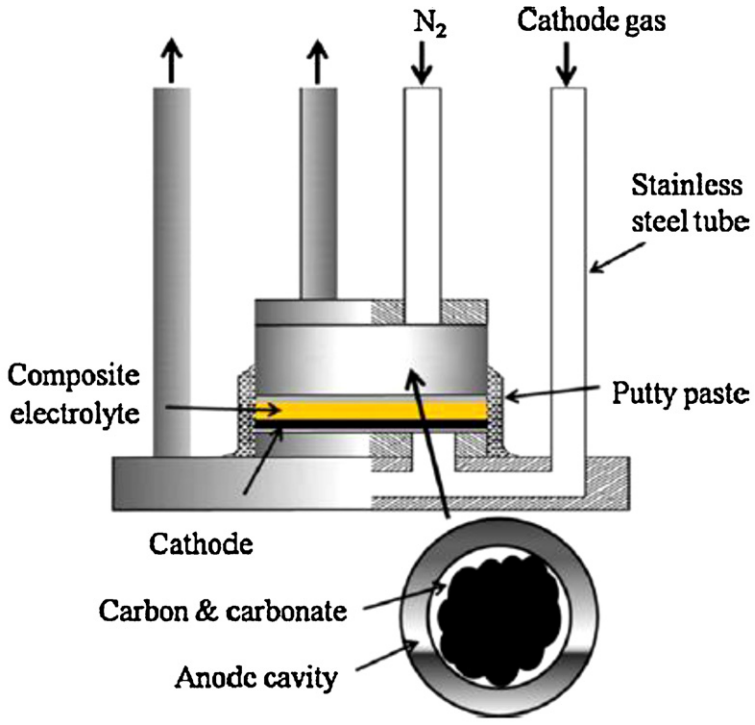

The schematic diagram of the DCFC single cell

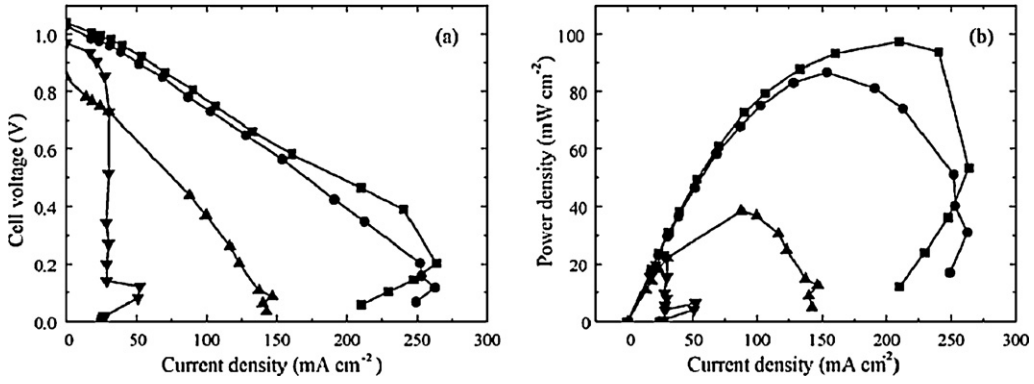

Fig. 49. The single DCFC cell (up) and the performance of the cell with variation of the cathode gas composition (bottom), indicating the effect of the CO_2 and the CO_3^{2-} transfer in the electrolyte.
Reprinted from [482] with permission of Elsevier Science Publishers B.V.

the other components for making up the system. The basic idea is based on the recent development of fuel cell technologies and the endothermic nature of the MCD reaction. MCD reaction absorbs heat which then is stored as the exergy of the two product streams, i.e. a hydrogen rich gas stream and a high purity carbon stream. The hydrogen rich gas stream is used directly as the feed of the IRSOFC. Because the stream contains only a limited amount of methane so that it can be expected to moderate effectively the problem of coking happened if feed the pure methane directly into the IRSOFC [115,116]. The carbon stream is used directly as the fuel of a DCFC [475,476]. The overall reaction in the DCFC is the oxidation of carbon to pure CO_2, which is beneficial and reduces the effort of CO_2 capture [477]. Furthermore, the release of heat in the DCFC due to the energy loses is at high temperature so that it can be used to heat the MCD reactor [51]. They calculated the exergy destruction in the devices/components of the system and gave a diagram as Fig. 47 [474]. Surprisingly to note, the exergy destruction at the IRSOFC is the largest among all the units in the system and the exergy destruction in the DCFC is moderately small. Their model and calculations prove that the system is highly efficient with an overall exergy to electricity efficiency as high as 68.24%, as illustrated in Fig. 48 [474].

DCFC is a device utilizing carbon as the fuel and converting the chemical energy to electricity with a high efficiency. The research on this device can be traced back to 1896 [478]. The theoretical thermal efficiency of a DCFC is almost 100% due to the fact that the entropy change of the carbon to CO_2 reaction is close to zero [475]. Excellent work has been done in a number of labs on the development of DCFCs [479–481]. Recently, Jia et al. [482] designed a new structure of DCFC and obtained a very promising performance with activated carbon as the fuel, see Fig. 49. The major advancement is the effective lowering of the reaction temperature and the increasing of the power density, which is due to the introduction of an intermediate temperature composite electrolyte [483–486]. In the previous works, it has been proved that the reactivity of the carbon used as the fuel of the DCFC is crucial to the performance and the efficiency of the DCFC [487,488]. The CNFs and CNTs from MCD reaction have a much higher and more tunable reaction activity than the other carbon forms and are conductive or semi-conductive to electricity. These carbon materials are likely the suitable feed for the DCFC.

6. Perspectives

MCD has become an attractive field for intensive fundamental research. It is a potential route for production of CO_x-free hydrogen and CNMs. The hydrogen produced can be consumed directly by PEMFC, while the carbon can be used as the components of advanced materials and the fuel of a DCFC. Compared to the other technologies for obtaining CO_x-free hydrogen, MCD reaction is conceptually promising due to its environmentally benign, energy efficiency and process simplicity. The co-produced CNTs or CNFs have been investigated extensively because of their excellent properties and great potential for many utilization purposes. In recent years, great cumulative effort has been made to commercialize the process and many aspects such as mechanism, kinetics, catalyst, reactor and process, have been investigated intensively. However, several challenges have to be overcome:

1. There are many important concepts have been reported, but still the reaction mechanism remains unclear. Simulation techniques become helpful. However, experimental techniques especially those *on-operando* dynamic methods are highly demanded.
2. High purity hydrogen stream is favorable for many utilization purposes, thus high methane conversion is needed. From the thermodynamic equilibrium data, high conversion needs high temperature, which is always detrimental to catalyst stability. Another approach to reach high methane conversion is to employ a membrane reactor. However, the membrane makes the reactor to be complex and difficult for scaling up. A lot of work should be done with this aspect.
3. A great effort has been paid on the evolvement and control of carbon morphology, which decide the process economics. Production of SWCNTs via MCD reaction has been a hot topic for investigation for many years. Nevertheless, the yield is still low and much more insight is still needed.
4. The reactor design has been explored. Fluidized and moving bed reactors have been considered suitable for the process. The novel concept, such as two-stage fluidized bed, is promising and makes the process more practical. Anyway, a smart design for the handling of the carbon and the continuous operation of the process is still called for.
5. For co-production of CO_x-free hydrogen and CNMs, the catalyst design is very much demanding. The life or the quasi-stable time is responsible for the amount of carbon retainable on the catalyst, which decides in turn the catalyst consumption, the operation mode and the reactor design. The support is responsible for the CO generation. Thus, a high metal loading catalyst is favorable to decrease the CO concentration. Fe catalysts have seemingly several advantages over nickel catalyst, such as lower cost and more environmentally friendly; more stable at high temperatures; and more value added MWCNTs formation. However, Fe catalyst has been less understood than Ni catalyst and the amount of carbon accumulated on a Fe catalyst is much less than on a Ni catalyst.
6. A number of new processes based on MCD reaction have been proposed. Fundamental research topics for realizing such processes are recognized at the same time, which should be worked out with a great effort.
7. Finally, the development of the market and application of the carbon materials is the final limiting factor for the commercialization of the process, because the demand for hydrogen is in an extremely large volume and the carbon co-produced should be consumed simultaneously as the hydrogen is consumed.

It should be remarked that, the efficient conversion and utilization of the limited fossil-fuel resources are one of the key routes to a sustainable future. MCD reaction and the proposed processes based on this reaction may be a help to achieve such a purpose.

Acknowledgements

The financial support of NSF of China under contract numbers 20736007 and 21076150 are gratefully acknowledged. The work has been also supported by the Program of Introducing Talents to the University Disciplines under file number B06006, and the Program for Changjiang Scholars and Innovative Research Teams in Universities under file number IRT 0641.

References

[1] T.N. Veziroglu, Hydrogen technology for energy needs of human settlements, Int. J. Hydrogen Energy 12 (1987) 99–129.
[2] D.J. Wuebbles, A.K. Jain, Concerns about climate change and the role of fossil fuel use, Fuel Process. Technol. 71 (2001) 99–119.
[3] T.J. Crowley, Causes of climate change over the past 1000 years, Science 289 (2000) 270–277.
[4] T.R. Karl, K.E. Trenberth, Modern global climate change, Science 302 (2003) 1719–1723.
[5] J.T. Overpeck, J.E. Cole, Abrupt change in earth's climate system, Annu. Rev. Environ. Resour. 31 (2006) 1–31.
[6] C.S. Song, Fuel processing for low-temperature and high-temperature fuel cells: challenges, and opportunities for sustainable development in the 21st century, Catal. Today 77 (2002) 17–49.
[7] S. Abraham, The Bush administration's approach to climate change, Science 305 (2004) 616–617.

[8] J.R. Rostrup-Nielsen, Fuels and energy for the future: the role of catalysis, Catal. Rev. Sci. Eng. 46 (2004) 247–270.
[9] Committee on Alternatives and Strategies for Future Hydrogen Production and Use, National Research Council, National Academy of Engineering, The hydrogen economy: opportunities, costs, barriers, and R&D needs, National Academy Press, Washington, 2004.
[10] S. Dunn, Hydrogen futures: toward a sustainable energy system, Int. J. Hydrogen Energy 27 (2002) 235–264.
[11] R.M. Navarro, M.A. Pena, J.L.G. Fierro, Hydrogen production reactions from carbon feedstock's: fossil fuels and biomass, Chem. Rev. 107 (2007) 3952–3991.
[12] J.N. Armor, Catalysis and the hydrogen economy, Catal. Lett. 101 (2005) 131–135.
[13] M. Ricci, P. Bellaby, R. Flynn, What do we know about public perceptions and acceptance of hydrogen? A critical review and new case study evidence, Int. J. Hydrogen Energy 33 (2008) 5868–5880.
[14] G.W. Crabtree, M.S. Dresselhaus, M.V. Buchanan, The hydrogen economy, Phys. Today December (2004) 39–45.
[15] L. Barretoa, A. Makihira, K. Riahi, The hydrogen economy in the 21st century: a sustainable development scenario, Int. J. Hydrogen Energy 28 (2003) 267–284.
[16] G.D. Berry, A.D. Pasternak, G.D. Rambach, J.R. Smith, R.N. Schock, Hydrogen as a future transportation fuel, Energy 21 (1996) 289–303.
[17] W. Lubitz, W. Tumas, Hydrogen: an overview, Chem. Rev. 107 (2007) 3900–3903.
[18] M. Momirlan, T.N. Veziroglu, Current status of hydrogen energy, Renew. Sustain. Energy Rev. 6 (2002) 141–179.
[19] K. Hassmann, H.M. Kuhne, Primary energy sources for hydrogen production, Int. J. Hydrogen Energy 18 (1993) 635–640.
[20] R. Kothari, D. Buddhi, R.L. Sawhney, Comparison of environmental and economic aspects of various hydrogen production methods, Renew. Sustain. Energy Rev. 12 (2008) 553–563.
[21] J.D. Holladay, J. Hu, D.L. King, Y. Wang, An overview of hydrogen production technologies, Catal. Today 139 (2009) 244–260.
[22] M. Balat, Possible methods for hydrogen production, Energy Sources. Part A 31 (2009) 39–50.
[23] J.N. Armor, The multiple roles for catalysis in the production of H_2, Appl. Catal. A: Gen. 176 (1999) 159–176.
[24] M.A. Pena, J.P. Gomez, J.L.G. Fierro, New catalytic routes for syngas and hydrogen production, Appl. Catal. A: Gen. 144 (1996) 7–57.
[25] J.N. Armor, Catalysis and opportunities for the production of H_2, Div. Fuel Chem. 45 (2000) 165–167.
[26] D.L. Trimm, Z.I. Onsan, Onboard fuel conversion for hydrogen-fuel-cell-driven vehicles, Catal. Rev. Sci. Eng. 43 (2001) 31–84.
[27] S. Holloway, Underground sequestration of carbon dioxide – a viable greenhouse gas mitigation option, Energy 30 (2005) 2318–2333.
[28] K. Riahi, E.S. Rubin, M.R. Taylor, L. Schrattenholzer, D. Hounshell, Technological learning for carbon capture and sequestration technologies, Energy Econ. 26 (2004) 539–564.
[29] D. Day, R.J. Evans, J.W. Lee, D. Reicosky, Economical CO_2, SO_x, and NO_x capture from fossil-fuel utilization with combined renewable hydrogen production and large-scale carbon sequestration, Energy 30 (2005) 2558–2579.
[30] S. Anderson, R. Newell, Prospects for carbon capture and storage technologies, Annu. Rev. Environ. Resour. 29 (2004) 109–142.
[31] H. Arakawa, M. Aresta, J.N. Armor, M.A. Barteau, E.J. Beckman, A.T. Bell, J.E. Bercaw, X.C. Creutz, O.E. Dinjus, D.A. Dixon, K. Domen, D.L. DuBois, J. Eckert, E. Fujita, D.H. Gibson, W.A. Goddard, D.W. Goodman, J. Keller, G.J. Kubas, H.H. Kung, J.E. Lyons, L.E. Manzer, T.J. Marks, K. Morokuma, K.M. Nicholas, R. Periana, L. Que, J. Rostrup-Nielson, W.M.H. Sachtler, L.D. Schmidt, A. Sen, G.A. Somorjai, P.C. Stair, B.R. Stults, W. Tumas, Catalysis research of relevance to carbon management: progress, challenges, and opportunities, Chem. Rev. 101 (2001) 953–996.
[32] M. Kara, S. Syri, A. Lehtila, S. Helynen, M. Ruska, J. Forsstrom, The impacts of EU CO_2 emissions trading on electricity markets and electricity consumers in Finland, Energy Econ. 30 (2008) 193–211.
[33] J.H. Lunsford, Catalytic conversion of methane to more useful chemicals and fuels: a challenge for the 21st century, Catal. Today 63 (2000) 165–174.
[34] A. Holmen, Direct conversion of methane to fuels and chemicals, Catal. Today 142 (2009) 2–8.
[35] J.R. Rostrup-Nielsen, Catalysis and large-scale conversion of natural gas, Catal. Today 21 (1994) 257–267.
[36] J.H. Wee, K.Y. Lee, Overview of the development of CO-tolerant anode electrocatalysts for proton-exchange membrane fuel cells, J. Power Sources 157 (2006) 128–135.
[37] M. Steinberg, H.C. Cheng, Modern and prospective technologies for hydrogen production from fossil fuels, Int. J. Hydrogen Energy 14 (1989) 797–820.
[38] R. Metkemeijer, P. Achard, Comparison of ammonia and methanol applied indirectly in a hydrogen fuel cell, Int. J. Hydrogen Energy 19 (1994) 535–542.
[39] R. Metkemeijer, P. Achard, Ammonia as a feedstock for a hydrogen fuel cell; reformer and fuel cell behaviour, J. Power Sources 49 (1994) 271–282.
[40] T.V. Choudhary, C. Sivadinarayana, D.W. Goodman, Catalytic ammonia decomposition: CO_x-free hydrogen production for fuel cell applications, Catal. Lett. 72 (2001) 197–201.
[41] A.S. Chellappa, C.M. Fischer, W.J. Thomson, Ammonia decomposition kinetics over Ni–Pt/Al_2O_3 for PEM fuel cell applications, Appl. Catal. A: Gen. 227 (2002) 231–240.
[42] H.C. Liu, H. Wang, J.H. Shen, Y. Sun, Z.M. Liu, Preparation, characterization and activities of the nano-sized Ni/SBA-15 catalyst for producing CO_x-free hydrogen from ammonia, Appl. Catal. A: Gen. 337 (2008) 138–147.
[43] H.C. Liu, H. Wang, J.H. Shen, Y. Sun, Z.M. Liu, Promotion effect of cerium and lanthanum oxides on Ni/SBA-15 catalyst for ammonia decomposition, Catal. Today 131 (2008) 444–449.
[44] F.R. Garcia-Garcia, Y.H. Ma, I. Rodriguez-Ramos, A. Guerrero-Ruiz, High purity hydrogen production by low temperature catalytic ammonia decomposition in a multifunctional membrane reactor, Catal. Commun. 9 (2008) 482–486.
[45] M. Momirlan, T. Veziroglu, Recent directions of world hydrogen production, Renew. Sustain. Energy Rev. 3 (1999) 219–231.
[46] L.H. Yao, Y.X. Li, J. Zhao, W.J. Ji, C.T. Au, Core–shell structured nanoparticles (M@SiO_2, Al_2O_3, MgO; M = Fe, Co, Ni, Ru) and their application in CO_x-free H_2 production via NH_3 decomposition, Catal. Today (2010), doi:10.1016/j.cattod.2010.05.009.
[47] Y.X. Li, L.H. Yao, S.Q. Liu, J. Zhao, W.J. Ji, C.T. Au, Cs-modified iron nanoparticles encapsulated in microporous and mesoporous SiO_2 for CO_x-free H_2 production via ammonia decomposition, Catal. Today (2010), doi:10.1016/j.cattod.2010.02.066.
[48] F.A. Uribe, T.A. Zawodzinski Jr., S. Gottesfeld, Effect of ammonia as possible fuel impurity on PEM fuel cell performance, Electrochem. Soc. Meet. Abstr. 98 (1998) 1103.
[49] F.A. Uribe, T.A. Zawodzinski Jr., A. Thomas, Effect of ammonia as potential fuel impurity on proton exchange membrane fuel cell performance, J. Electrochem. Soc. 149 (2002) A293–A296.
[50] R. Halseid, P.J.S. Vie, R. Tunold, Effect of ammonia on the performance of polymer electrolyte membrane fuel cells, J. Power Sources 154 (2006) 343–350.
[51] Y.D. Li, J.L. Chen, Y.N. Qin, L. Chang, Simultaneous production of hydrogen and nanocarbon from decomposition of methane on a nickel-based catalyst, Energy Fuels 14 (2000) 1188–1194.
[52] M. Steinberg, Fossil fuel decarbonization technology for mitigating global warming, Int. J. Hydrogen Energy 24 (1999) 771–777.
[53] J.L. Chen, Y.D. Li, Z.Q. Li, X.X. Zhang, Production of CO_x-free hydrogen and nanocarbon by direct decomposition of undiluted methane on Ni–Cu–alumina catalysts, Appl. Catal. A: Gen. 269 (2004) 179–186.
[54] T.V. Choudhary, C. Sivadinarayana, C.C. Chusuei, A. Klinghoffer, D.W. Goodman, Hydrogen production via catalytic decomposition of methane, J. Catal. 199 (2001) 9–18.
[55] T.V. Choudhary, D.W. Goodman, CO-free fuel processing for fuel cell applications, Catal. Today 77 (2002) 65–78.
[56] N.Z. Muradov, T.N. Veziroglu, From hydrocarbon to hydrogen–carbon to hydrogen economy, Int. J. Hydrogen Energy 30 (2005) 225–237.
[57] W.Z. Qian, T. Liu, Z.W. Wang, F. Wei, Z.F. Li, G.H. Luo, Y.D. Li, Production of hydrogen and carbon nanotubes from methane decomposition in a two-stage fluidized bed reactor, Appl. Catal. A: Gen. 260 (2004) 223–228.
[58] S. Iijima, Helical microtubules of graphitic carbon, Nature 354 (1991) 56–58.
[59] A.C. Dillon, K.M. Jones, T.A. Bekkedahl, C.H. Kiang, D.S. Bethune, M.J. Heben, Storage of hydrogen in single-walled carbon nanotubes, Nature 386 (1997) 377–379.
[60] K.P. de Jong, J.W. Geus, Carbon nanofibers: catalytic synthesis and applications, Catal. Rev. Sci. Eng. 42 (2000) 481–510.
[61] D. Qian, G.J. Wagner, W.K. Liu, M.F. Yu, R.S. Ruoff, Mechanics of carbon nanotubes, Appl. Mech. Rev. 55 (2002) 495–533.
[62] R.H. Baughman, A.A. Zakhidov, W.A. de Heer, Carbon nanotubes – the route toward applications, Science 297 (2003) 787–792.
[63] O. Breuer, U.J. Sundararaj, Big returns from small fibers: a review of polymer/carbon nanotube composites, Polym. Compos. 25 (2004) 630–645.
[64] K. Balasubramanian, M. Burghard, Biosensors based on carbon nanotubes, Anal. Bioanal. Chem. 385 (2006) 452–468.
[65] P.M. Ajayan, J.M. Tour, Nanotube composites, Nature 447 (2007) 1066–1068.
[66] P.R. Bandaru, Electrical properties and applications of carbon nanotube structures, J. Nanosci. Nanotechnol. 7 (2007) 1239–1267.
[67] V.V. Shinkarev, A.M. Glushenkov, D.G. Kuvshinov, G.G. Kuvshinov, Nanofibrous carbon with herringbone structure as an effective catalyst of the H_2S selective oxidation, Carbon 48 (2010) 2004–2012.
[68] X.F. Guo, J.H. Kim, G.J. Kim, Dehydrogenation of ethylbenzene to styreneona direct synthesized Co,Ni/carbon nanotubes catalysts, Catal. Today (2010), doi:10.1016/j.cattod.2010.10.004.
[69] X.M. Wang, N. Li, L.D. Pfefferle, G.L. Haller, Pt–Co bimetallic catalyst supported on single walled carbon nanotube: XAS and aqueous phase reforming activity studies, Catal. Today 146 (2009) 160–165.
[70] S. Ahmed, A. Aitani, F. Rahman, A. Al-Dawood, F. Al-Muhaish, Decomposition of hydrocarbons to hydrogen and carbon, Appl. Catal. A: Gen. 359 (2009) 1–7.
[71] H.F. Abbas, W.M.A. Wan Daud, Hydrogen production by methane decomposition: a review, Int. J. Hydrogen Energy 35 (2010) 1160–1190.
[72] Y.D. Li, R. Zhang, J.L. Chen, X.M. Li, A highly efficient power generation process from natural gas: an exergy analysis, in: 2nd European Hydrogen Energy Conference, November, Zaragoza, Spain, 2005, p. 518.
[73] M. Steinberg, An innovative highly efficient combined cycle fossil and biomass fuel power generation and hydrogen production plant with zero CO_2 emission, in: Abstracts of Papers, 226th ACS National Meeting, New York, NY, United States, September 7–11, 2003.
[74] Q.H. Liu, Y. Tian, H.J. Li, L.J. Jia, C. Xia, L.T. Thompsonb, Y.D. Li, High efficiency chemical energy conversion system based on methane catalytic decomposition reaction and two fuel cells. Part I. Process modeling and validation, J. Power Sources 195 (2010) 6539–6548.

[75] T.V. Choudhary, D.W. Goodman, Stepwise methane steam reforming: a route to CO-free hydrogen, Catal. Lett. 59 (1999) 93–94.
[76] T.V. Choudhary, C. Sivadinarayana, D.W. Goodman, Production of CO_x-free hydrogen for fuel cells via step-wise hydrocarbon reforming and catalytic dehydrogenation of ammonia, Chem. Eng. J. 93 (2003) 69–80.
[77] V.R. Choudhary, S. Banerjee, A.M. Rajput, Hydrogen from step-wise steam reforming of methane over Ni/ZrO_2: factors affecting catalytic methane decomposition and gasification by steam of carbon formed on the catalyst, Appl. Catal. A: Gen. 234 (2002) 259–270.
[78] V.R. Choudhary, S. Banerjee, A.M. Rajput, Continuous production of H_2 at low temperature from methane decomposition over Ni-containing catalyst followed by gasification by steam of the carbon on the catalyst in two parallel reactors operated in cyclic manner, J. Catal. 198 (2001) 136–141.
[79] J.B. Zhao, Y.D. Li, L. Chang, Thermodynamic analysis of combining methane decomposition and CO_2 gasification to produce syngas, J. Nat. Gas Chem. Technol. (China) 22 (1997) 48–51.
[80] M.H. Kim, E.K. Lee, J.H. Jun, G.Y. Han, S.J. Kong, B.K. Lee, T.J. Lee, K.J. Yoon, Hydrogen production by catalytic decomposition of methane over activated carbons: deactivation study, Korean J. Chem. Eng. 20 (2003) 835–839.
[81] A.M. Dunker, S. Kumar, P.A. Mulawa, Production of hydrogen by thermal decomposition of methane in a fluidized-bed reactor – effects of catalyst, temperature, and residence time, Int. J. Hydrogen Energy 31 (2006) 473–484.
[82] B.H. Ryu, S.Y. Lee, D.H. Lee, G.Y. Han, T.J. Lee, K.J. Yoon, Catalytic characteristics of various rubber-reinforcing carbon blacks in decomposition of methane for hydrogen production, Catal. Today 123 (2007) 303–309.
[83] E.K. Lee, S.Y. Lee, G.Y. Han, B.K. Lee, T.J. Lee, J.H. Jun, K.J. Yoon, Catalytic decomposition of methane over carbon blacks for CO_2-free hydrogen production, Carbon 42 (2004) 2641–2648.
[84] S.Y. Lee, J.H. Kwak, G.Y. Han, T.J. Lee, K.J. Yoon, Characterization of active sites for methane decomposition on carbon black through acetylene chemisorption, Carbon 46 (2008) 342–348.
[85] J.L. Chen, M. He, G.W. Wang, Y.D. Li, Z.H.J. Zhu, Production of hydrogen from methane decomposition using nanosized carbon black as catalyst in a fluidized-bed reactor, Int. J. Hydrogen Energy 34 (2009) 9730–9736.
[86] M.H. Kim, E.K. Lee, J.H. Jun, S.J. Kong, G.Y. Han, B.K. Lee, T.J. Lee, K.J. Yoon, Hydrogen production by catalytic decomposition of methane over activated carbons: kinetic study, Int. J. Hydrogen Energy 29 (2004) 187–193.
[87] N. Muradov, F. Smith, A. T-Raissi, Catalytic activity of carbons for methane decomposition reaction, Catal. Today 102–103 (2005) 225–233.
[88] A. Dufour, A. Celzard, B. Ouartassi, F. Broust, V. Fierro, A. Zoulalian, Effect of micropores diffusion on kinetics of CH_4 decomposition over a wood-derived carbon catalyst, Appl. Catal. A: Gen. 360 (2009) 120–125.
[89] D.P. Serrano, J.A. Botasa, R. Guil-Lopeza, H_2 production from methane pyrolysis over commercial carbon catalysts: kinetic and deactivation study, Int. J. Hydrogen Energy 34 (2009) 4488–4494.
[90] D.P. Serrano, J.A. Botas, P. Pizarro, R. Guil-Lopez, G. Gomez, Ordered mesoporous carbons as highly active catalysts for hydrogen production by CH_4 decomposition, Chem. Commun. (2008) 6585–6587.
[91] K.K. Lee, G.Y. Han, K.J. Yoon, B.K. Lee, Thermocatalytic hydrogen production from the methane in a fluidized bed with activated carbon catalyst, Catal. Today 93–95 (2004) 81–86.
[92] D.P. Serrano, J.A. Botas, J.L.G. Fierro, R. Guil-Lopez, P. Pizarro, G. Gomez, Hydrogen production by methane decomposition: origin of the catalytic activity of carbon materials, Fuel 89 (2010) 1241–1248.
[93] T.V. Hughes, C.R. Chambers, Manufacture of carbon filaments, US Patent 405480, 1889.
[94] P. Schutzenberger, L. Schutzenberger, Sur quelques faits relatives a l'histoire du carbone, C. R. Acad. Sci. Paris 111 (1890) 774.
[95] L.V. Radushkevich, V.M. Lukyanovich, O strukture ugleroda, obrazujucegosja pri termiceskom razlozenii okisi ugleroda na zeleznom kontakte, Zhurn. Fisic. Chim. 26 (1952) 88–95.
[96] M. Monthioux, V.L. Kuznetsov, Who should be given the credit for the discovery of carbon nanotubes? Carbon 44 (2006) 1621–1623.
[97] C. Herring, J.K. Galt, Elastic and plastic properties of very small metal specimens, Phys. Rev. 85 (1952) 1060.
[98] M. Hillert, N. Lang, The structure of graphite filaments, Zeit. Krist. 111 (1958) 24–29.
[99] T. Koyama, Formation of carbon fibers from benzene, Carbon 10 (1972) 757–758.
[100] T. Koyama, M. Endo, Y. Onuma, Carbon fibers obtained by thermal decomposition of vaporized hydrocarbon, Jpn. J. Appl. Phys. 11 (1972) 445–449.
[101] I. Ziegler, R. Fournet, P.M. Marquaire, Influence of surface on chemical kinetic of pyrocarbon deposition obtained by propane pyrolysis, J. Anal. Appl. Pyrol. 73 (2005) 107–115.
[102] I. Ziegler, R. Fournet, P.M. Marquaire, Pyrolysis of propane for CVI of pyrocarbon. Part I. Experimental and modeling study of the formation of toluene and aliphatic species, J. Anal. Appl. Pyrol. 73 (2005) 212–230.
[103] I. Ziegler, R. Fournet, P.M. Marquaire, Pyrolysis of propane for CVI of pyrocarbon. Part II. Experimental and modeling study of polyaromatic species, J. Anal. Appl. Pyrol. 73 (2005) 231–247.
[104] Z.D. Isabelle, R. Fournet, P.M. Marquaire, Pyrolysis of propane for CVI of pyrocarbon. Part III. Experimental and modeling study of the formation of pyrocarbon, J. Anal. Appl. Pyrol. 79 (2007) 268–277.
[105] T. Baird, J.R. Fryer, B. Grant, Structure of fibrous carbon, Nature 233 (1971) 329–330.
[106] M. Endo, T. Koyama, Y. Hishiyama, Structural improvement of carbon fibers prepared from benzene, Jpn. J. Appl. Phys. 15 (1976) 2073–2076.
[107] A. Oberlin, M. Endo, T. Koyama, Filamentous growth of carbon through benzene decomposition, J. Cryst. Growth 32 (1976) 335–349.
[108] J.S. Speck, M. Endo, M.S. Dresselhaus, Structure and intercalation of thin benzene derived carbon fibers, J. Cryst. Growth 94 (1989) 834–848.
[109] N.M. Rodriguez, A. Chamers, R.T.K. Baker, Catalytic engineering of carbon nanostructures, Langmuir 11 (1995) 3862–3866.
[110] P. Chen, H.B. Zhang, G.D. Lin, Q. Hong, K.R. Tsai, Growth of carbon nanotubes by catalytic decomposition of methane or CO on a Ni–MgO Catalyst, Carbon 35 (1997) 1495–1501.
[111] G.P. Daumit, Summary of panel discussion, "carbon fiber industry: current and future", Carbon 27 (1989) 759–764.
[112] R.T.K. Baker, In situ electron microscopy studies of catalyst deactivation, Stud. Surf. Sci. Catal. 68 (1991) 1–27.
[113] G.F. Froment, The modeling of catalyst deactivation by coke formation, Stud. Surf. Sci. Catal. 68 (1991) 53–83.
[114] J.R. Rostrup-Nielsen, Coking on nickel catalysts for steam reforming of hydrocarbons, J. Catal. 33 (1974) 184–201.
[115] D.L. Trimm, The formation and removal of coke from nickel catalyst, Catal. Rev. Sci. Eng. 16 (1977) 155–189.
[116] C.H. Bartholomew, Carbon deposition in steam reforming and methanation, Catal. Rev. Sci. Eng. 24 (1982) 67–112.
[117] Y. Nishiyama, Y. Tamai, Deposition of carbon and its hydrogenation catalyzed by nickel, Carbon 14 (1976) 13–17.
[118] C.A. Bernardo, L.S. Lobo, Evidence that carbon formation from acetylene on nickel involves bulk diffusion, Carbon 14 (1976) 287–288.
[119] A. Tomita, Y. Tamai, Hydrogenation of carbon catalyzed by transition metals, J. Catal. 27 (1972) 293–300.
[120] E.G.M. Kuijpers, J.W. Jansen, A.J. van Dillen, J.W. Geus, The reversible decomposition of methane on a Ni/SiO_2 catalyst, J. Catal. 72 (1981) 75–82.
[121] G.F. Froment, Kinetic modeling of hydrocarbon processing and the effect of catalyst deactivation by coke formation, Catal. Rev. Sci. Eng. 50 (2008) 1–18.
[122] D.L. Trimm, Catalysts for the control of coking during steam reforming, Catal. Today 49 (1999) 3.
[123] J.R. Rostrup-Nielsen, Industrial relevance of coking, Catal. Today 37 (1997) 225–232.
[124] B.M. Vogelaar, S. Eijsbouts, J.A. Bergwerff, J.J. Heiszwolf, Hydroprocessing catalyst deactivation in commercial practice, Catal. Today 154 (2010) 256–263.
[125] R. Iley, H.L. Riley, The deposition of carbon on vitreous silica, J. Chem. Soc. London 2 (1948) 1362–1366.
[126] V.J. Kehrer Jr., H. Leidheiser Jr., The catalytic decomposition of carbon monoxide on large metallic single crystals, J. Phys. Chem. 58 (1954) 550–555.
[127] W.R. Davis, R.J. Slawson, G.R. Rigby, An unusual form of carbon, Nature 171 (1953) 756–1756.
[128] J.R. Rostrup-Nielsen, Equilibria of decomposition reactions of carbon monoxide and methane over nickel catalysts, J. Catal. 27 (1972) 343–356.
[129] R.T.K. Baker, Catalytic growth of carbon filaments, Carbon 27 (1989) 315–323.
[130] M. Endo, Grow carbon fibers in the vapor phase, Chemtech September (1988) 568.
[131] G.S. Hoogenraad, The growth and utilization of carbon fibrils (thesis), Universiteit Utrecht, The Netherlands, 1995.
[132] G.G. Tibbetts, M. Endo, C.P. Beetz Jr., Carbon fibers grown from the vapor phase: a novel material, SAMPE J. 22 (1986) 30–35.
[133] S. Iijima, T. Ichihashi, Single-shell carbon nanotubes of 1-nm diameter, Nature 363 (1993) 603–605.
[134] D.S. Bethune, C.H. Klang, M.S. de Vries, G. Gorman, R. Savoy, J. Vazquez, R. Beyers, Cobalt-catalysed growth of carbon nanotubes with single-atomic-layer walls, Nature 363 (1993) 605–607.
[135] P. Avouris, Z.H. Chen, V. Perebeinos, Carbon-based electronics, Nat. Nanotechnol. 2 (2007) 605–615.
[136] A. Bachtold, P. Hadley, T. Nakanishi, C. Dekker, Logic circuits with carbon nanotube transistors, Science 294 (2001) 1317–1320.
[137] R.T.K. Baker, M.A. Barber, P.S. Harris, F.S. Feates, R.J. Waite, Nucleation and growth of carbon deposits from the nickel catalyzed decomposition of acetylene, J. Catal. 26 (1972) 51–62.
[138] R.T.K. Baker, P.S. Harris, R.B. Thomas, R.J. Waite, Formation of filamentous carbon from iron, cobalt and chromium catalyzed decomposition of acetylene, J. Catal. 30 (1973) 86–95.
[139] J. Rostrup-Nielsen, D.L. Trimm, Mechanisms of carbon formation on nickel-containing catalysts, J. Catal. 48 (1977) 155–165.
[140] T.V. Choudhary, E. Aksoylu, D.W. Goodman, Nonoxidative activation of methane, Catal. Rev. Sci. Eng. 45 (2003) 151–203.
[141] J.F. Colomer, C. Stephan, S. Lefrant, G.V. Tendeloo, I. Willems, Z. Konya, A. Fonseca, C. Laurent, J.B. Nagy, Large-scale synthesis of single-wall carbon nanotubes by catalytic chemical vapor deposition (CCVD) method, Chem. Phys. Lett. 317 (2000) 83–89.
[142] L.Y. Piao, Y.D. Li, J.L. Chen, L. Chang, J.Y.S. Lin, Methane decomposition to carbon nanotubes and hydrogen on an alumina supported nickel aerogel catalyst, Catal. Today 74 (2002) 145–155.
[143] A.R. Biris, Z.R. Li, E. Dervishi, D. Lupu, Y. Xu, V. Saini, F. Watanabe, A.S. Biris, Effect of hydrogen on the growth and morphology of single wall carbon nanotubes synthesized on a Fe–Mo/MgO catalytic system, Phys. Lett. A 372 (2008) 3051–3057.

[144] T. Baird, J.R. Fryer, B. Grant, Carbon formation on iron and nickel foils by hydrocarbon pyrolysis reactions at 700 °C, Carbon 12 (1974) 591–602.
[145] Y.A. Zhu, Z.J. Sui, T.J. Zhao, Y.C. Dai, Z.M. Cheng, W.K. Yuan, Modeling of fishbone-type carbon nanofibers: a theoretical study, Carbon 43 (2005) 1694–1699.
[146] Y.D. Li, J.L. Chen, L. Chang, Catalytic growth of carbon fibers from methane on a nickel–alumina composite catalyst prepared from Feitknecht compound precursor, Appl. Catal. A: Gen. 163 (1997) 45–57.
[147] Y.D. Li, J.L. Chen, Y.M. Ma, J.B. Zhao, Y.N. Qin, L. Chang, Formation of bamboo-like nanocarbon and evidence for the quasi-liquid state of nanosized metal particles at moderate temperatures, Chem. Commun. (1999) 1141–1142.
[148] J.L. Chen, Y.D. Li, Y.M. Ma, Y.N. Qin, L. Chang, Formation of bamboo-shaped carbon filaments and dependence of their morphology on catalyst composition and reaction conditions, Carbon 39 (2001) 1467–1475.
[149] X.X. Zhang, Z.Q. Li, G.H. Wen, K.K. Fung, J.L. Chen, Y.D. Li, Microstructure and growth of bamboo-shaped carbon nanotubes, Chem. Phys. Lett. 333 (2001) 509–514.
[150] C.N. He, N.Q. Zhao, X.W. Du, C.S. Shi, J. Ding, J.J. Li, Y.D. Li, Low-temperature synthesis of carbon onions by chemical vapor deposition using a nickel catalyst supported on aluminum, Scripta Mater. 54 (2006) 689–693.
[151] C.N. He, N.Q. Zhao, C.S. Shi, X.W. Du, J.J. Li, Carbon nanotubes and onions from methane decomposition using Ni/Al catalysts, Mater. Chem. Phys. 97 (2006) 109–115.
[152] Y. Li, X.B. Zhang, X.Y. Tao, J.M. Xu, F. Chen, W.Z. Huang, F. Liu, Growth mechanism of multi-walled carbon nanotubes with or without bundles by catalytic deposition of methane on Mo/MgO, Chem. Phys. Lett. 386 (2004) 105–110.
[153] N. Hamada, S. Sawada, A. Oshiyama, New one-dimensional conductors: graphitic microtubules, Phys. Rev. Lett. 68 (1992) 1579–1581.
[154] S. Helveg, C. Lopez-Cartes, J. Sehested, P.L. Hansen, B.S. Clausen, J.R. Rostrup-Nielsen, F. Abild-Pedersen, J.K. Norskov, Atomic-scale imaging of carbon nanofibre growth, Nature 427 (2004) 426–429.
[155] M. Monthioux, L. Noe, L. Dussault, J.C. Dupin, N. Latorre, T. Ubieto, E. Romeo, C. Royo, A. Monzon, C. Guimon, Texturising and structurising mechanisms of carbon nanofilaments during growth, J. Mater. Chem. 17 (2007) 4611–4618.
[156] Z.Q. Li, J.L. Chen, X.X. Zhang, Y.D. Li, K.K. Fung, Catalytic synthesized carbon nanostructures from methane using nanocrystalline Ni, Carbon 40 (2002) 409–415.
[157] R.S. Ruoff, D.C. Lorents, B. Chan, R. Malhotra, S. Subramoney, Single crystal metals encapsulated in carbon nanoparticles, Science 259 (1993) 346–348.
[158] D.X. Li, J.L. Chen, Y.D. Li, Evidence of composition deviation of metal particles of a Ni–Cu/Al_2O_3 catalyst during methane decomposition to CO_x-free hydrogen, Int. J. Hydrogen Energy 34 (2009) 299–307.
[159] M. Audier, M. Coulon, L. Bonnetain, Disproportionation of CO on iron–cobalt alloys. I. Thermodynamic study, Carbon 21 (1983) 93–97.
[160] M. Audier, M. Coulon, L. Bonnetain, Disproportionation of CO on iron–cobalt alloys. II. Kinetic study on iron–cobalt alloys of different compositions, Carbon 21 (1983) 99–103.
[161] M. Audier, M. Coulon, L. Bonnetain, Disproportionation of CO on iron–cobalt alloys. III. Kinetic laws of the carbon growth and catalyst fragmentation, Carbon 21 (1983) 105–110.
[162] R.T. Yang, J.P. Chen, Mechanism of carbon filament growth on metal catalysts, J. Catal. 115 (1989) 52–64.
[163] S. Helveg, P.L. Hansen, Atomic-scale studies of metallic nanocluster catalysts by in situ high-resolution transmission electron microscopy, Catal. Today 111 (2006) 68–73.
[164] V.V. Chesnokov, V.I. Zaikovskii, R.A. Buyanov, V.V. Molchanov, L.M. Plyasova, Morphology of carbon from methane on nickel-containing catalysts, Catal. Today 24 (1995) 265–267.
[165] J.L. Chen, X.M. Li, Y.D. Li, Y.N. Qin, Production of hydrogen and nanocarbon from direct decomposition of undiluted methane on high-nickeled Ni–Cu–Alumina catalysts, Chem. Lett. 32 (2003) 424–425.
[166] J.W. Snoeck, G.F. Froment, M. Fowles, Filamentous carbon formation and gasification: thermodynamics, driving force, nucleation, and steady-state growth, J. Catal. 169 (1997) 240–249.
[167] S. Takenaka, M. Ishida, M. Serizawa, E. Tanabe, K. Otsuka, Formation of carbon nanofibers and carbon nanotubes through methane decomposition over supported cobalt catalysts, J. Phys. Chem. B 108 (2004) 11464–11472.
[168] S. Takenaka, S. Kobayashi, H. Ogihara, K. Otsuka, Ni/SiO_2 catalyst effective for methane decomposition into hydrogen and carbon nanofiber, J. Catal. 217 (2003) 79–87.
[169] S. Amelinckx, X.B. Zhang, D. Bernaerts, X.F. Zhang, V. Ivanov, J.B. Nagy, A formation mechanism for catalytically grown helix-shaped graphite nanotubes, Science 265 (1994) 635–639.
[170] V.V. Kovalevski, A.N. Safronov, Pyrolysis of hollow carbons on melted catalyst, Carbon 36 (1998) 963.
[171] M. Lin, J.P.Y. Tan, C. Boothroyd, K.P. Loh, E.S. Tok, Y.L. Foo, Dynamical observation of bamboo-like carbon nanotube growth, Nano Lett. 7 (2007) 2234.
[172] Z.L. Li, J.A. Larsson, P. Larsson, R. Ahuja, J.M. Tobin, J.P. O'Byrne, M.A. Morris, G. Attard, J.D. Holmes, Copper/molybdenum nanocomposite particles as catalysts for the growth of bamboo-structured carbon nanotubes, J. Phys. Chem. C 112 (2008) 12201–12206.
[173] J.P. O'Byrne, Z.l. Li, J.M. Tobin, J.A. Larsson, P. Larsson, R. Ahuja, J.D. Holmes, Growth of carbon nanotubes from heterometallic palladium and copper catalysts, J. Phys. Chem. C 114 (2010) 8115–8119.
[174] Y. Saito, Nanoparticles and filled nanocapsules, Carbon 33 (1995) 979–988.
[175] J. Kong, A.M. Cassell, H.J. Dai, Chemical vapor deposition of methane for single-walled carbon nanotubes, Chem. Phys. Lett. 292 (1998) 567–574.
[176] A.M. Cassell, J.A. Raymakers, J. Kong, H.J. Dai, Large scale CVD synthesis of single-walled carbon nanotubes, J. Phys. Chem. B 103 (1999) 6484–6492.
[177] S.Y. Son, Y. Lee, S. Won, D.H. Lee, S.D. Kim, S.W. Sung, High-quality multiwalled carbon nanotubes from catalytic decomposition of carboneous materials in gas–solid fluidized beds, Ind. Eng. Chem. Res. 47 (2008) 2166–2175.
[178] A.C. Dupuis, The catalyst in the CCVD of carbon nanotubes – a review, Prog. Mater. Sci. 50 (2005) 929–961.
[179] P. Nikolaev, M. Bronikowski, R. Bradley, F. Rohmund, D. Colbert, K. Smith, Gas-phase catalytic growth of single-walled carbon nanotubes from carbon monoxide, Chem. Phys. Lett. 313 (1999) 91–97.
[180] H.J. Dai, A.G. Rinzler, P. Nikolaev, A. Thess, D.T. Colbert, R.E. Smalley, Single-wall nanotubes produced by metal-catalyzed disproportionation of carbon monoxide, Chem. Phys. Lett. 260 (1996) 471–475.
[181] Y. Shibuta, S. Maruyama, Molecular dynamics simulation formation process of single-walled carbon nanotubes by CCVD method, Chem. Phys. Lett. 382 (2003) 381–386.
[182] S.P. Chai, S.H.S. Zein, A.R. Mohamed, The effect of catalyst calcination temperature on the diameter of carbon nanotubes synthesized by the decomposition of methane, Carbon 45 (2007) 1535–1541.
[183] C.S. Kuo, A. Bai, C.M. Huang, Y.Y. Li, C.C. Hu, C.C. Chen, Diameter control of multiwalled carbon nanotubes using experimental strategies, Carbon 43 (2005) 2760–2768.
[184] S.G. Kang, K.K. Cho, K.W. Kim, G.-B. Cho, Catalytic growth of single- and double-walled carbon nanotubes from Fe–Mo nanoparticles supported on MgO, J. Alloys Compd. 449 (2008) 269–273.
[185] G.L. Hornyak, L. Grigorian, A.C. Dillon, P.A. Parilla, K.M. Jones, M.J. Heben, A temperature window for chemical vapor decomposition growth of single-wall carbon nanotubes, J. Phys. Chem. B 106 (2002) 2821–2825.
[186] J.W. Snoeck, G.F. Froment, M. Fowles, Kinetic study of the carbon filament formation by methane cracking on a nickel catalyst, J. Catal. 169 (1997) 250–262.
[187] K. Otsuka, S. Kobayashi, S. Takenaka, Hydrogen–Deuterium exchange studies on the decomposition of methane over Ni/SiO_2, J. Catal. 200 (2001) 4–9.
[188] J.R. Rostrup-Nielsen, in: J.R. Anderson, M. Boudart (Eds.), Catalytic Steam Reforming, Springer, Berlin, 1984 (reprinted from vol. 5 of series Catalysis, Science and Technology, 1983).
[189] J.H. Larsen, I. Chorkendorff, From fundamental studies of reactivity on single crystals to the design of catalysts, Surf. Sci. Rep. 35 (1999) 163–222.
[190] T.V. Choudhary, D.W. Goodman, Methane activation on Ni and Ru model catalysts, J. Mol. Catal. A: Chem. 163 (2000) 9–18.
[191] F.C. Schouten, O.L.J. Gijzeman, G.A. Bootsma, Interaction of methane with Ni(1 1 1) and Ni(1 0 0)-diffusion of carbon into nickel through the (1 0 0) surface; an AES–Leed study, Surf. Sci. 87 (1979) 1–12.
[192] T.P. Beebe Jr., D.W. Goodman, B.D. Kay, J.T. Yates, Kinetics of the activated dissociative adsorption of methane on the low index planes of nickel single-crystal surfaces, J. Chem. Phys. 87 (1987) 2305–2315.
[193] L. Hanley, Z. Xu, J.T. Yates Jr., Methane activation on Ni(1 1 1) at high-pressures, Surf. Sci. Lett. 248 (1991) L265–273.
[194] C.T. Rettner, H.E. Pfnur, D.J. Auerbach, Dissociative chemisorption of CH_4 on W(1 1 0): dramatic activation by initial kinetic-energy, Phys. Rev. Lett. 54 (1985) 2716–2719.
[195] T.C. Lo, G. Ehrlich, Activated chemisorption of methane and tunneling, Surf. Sci. 179 (1987) L19–25.
[196] M.B. Lee, Q.Y. Yang, S.T. Ceyer, Dynamics of the activated dissociative chemisorption of CH_4 and implication for the pressure gap in catalysis: a molecular beam high resolution electron energy loss study, J. Chem. Phys. 87 (1987) 2724–2741.
[197] P.M. Holmblad, J. Wambach, I. Chorkendorff, Molecular beam study of dissociative sticking of methane on Ni(1 0 0), J. Chem. Phys. 102 (1995) 8255–8263.
[198] B.O. Nielsen, A.C. Luntz, P.M. Holmblad, I. Chorkendorff, Activated dissociative chemisorption of methane on Ni(1 0 0): a direct mechanism under thermal conditions, Catal. Lett. 32 (1995) 15–30.
[199] A.V. Hamza, R.J. Madix, The activation of alkanes on Ni(1 0 0), Surf. Sci. 179 (1987) 25–46.
[200] F.C. Schouten, E.W. Kaleveld, G.A. Bootsma, AES–LEED–Ellipsometry study of the kinetics of the interaction of methane with Ni(1 1 0), Surf. Sci. 63 (1977) 460–474.
[201] I. Chorkendorff, I. Alstrup, S. Ullmann, XPS study of chemisorption of CH_4 on Ni(1 1 0), Surf. Sci. 227 (1990) 291–296.
[202] X.D. Jiang, D.W. Goodman, The effect of Suffer on the dissociative adsorption of methane on nickel, Catal. Lett. 4 (1990) 173–180.
[203] R.A. Campbell, J. Szanyi, P. Lenz, D.W. Goodman, Methane activation on clean and oxidized Ni(1 0 0), Catal. Lett. 17 (1993) 39–46.
[204] R.C. Egeberg, S. Ullmann, I. Alstrup, C.B. Mullins, I. Chorkendorff, Dissociation of CH_4 on Ni(1 1 1) and Ru(0 0 0 1), Surf. Sci. 497 (2002) 183–193.
[205] B. Xing, X.Y. Pang, G.C. Wang, Z.F. Shang, Investigation the active site of methane dissociation on Ni-based catalysts: a first-principles analysis, J. Mol. Catal. A: Chem. 315 (2010) 187.
[206] O. Swang, K. Faegri Jr., O. Gropen, U. Wahlgren, P. Siegbahn, A theoretical study of the chemisorption of methane on a Ni(1 0 0) surface, Chem. Phys. 156 (1991) 379–386.
[207] H.S. Bengaard, I. Alstrup, I. Chorkendorff, S. Ullmann, J.R. Rostrup-Nielsen, J.K. Norskov, Chemisorption of methane on Ni(1 0 0) and Ni(1 1 1) surfaces with preadsorbed potassium, J. Catal. 187 (1999) 238–244.

[208] W.Z. Lai, D.Q. Xie, D.H. Zhang, First-principles study of adsorption of methyl, coadsorption of methyl and hydrogen, and methane dissociation on Ni(1 0 0), Surf. Sci. 594 (2005) 83–92.
[209] G. Henkelman, A. Arnaldsson, H. Jonsson, Theoretical calculations of CH_4 and H_2 associative desorption from Ni(1 1 1): could subsurface hydrogen play an important role? J. Chem. Phys. 124 (2006) 044708-1–44708-9.
[210] R.M. Watwe, H.S. Bengaard, J.R. Rostrup-Nielsen, J.A. Dumesic, J.K. Nørskov, Theoretical studies of stability and reactivity of CH_x species on Ni(1 1 1), J. Catal. 189 (2000) 16–30.
[211] Y.A. Zhu, Y.C. Dai, D. Chen, W.K. Yuan, First-principles calculations of CH_4 dissociation on Ni(1 0 0) surface along different reaction pathways, J. Mol. Catal. A: Chem. 264 (2007) 299–308.
[212] J.N. Carstens, A.T. Bell, Methane activation and conversion to higher hydrocarbons on supported ruthenium, J. Catal. 161 (1996) 423–429.
[213] J.M. Wei, E. Iglesia, Reaction pathways and site requirements for the activation and chemical conversion of methane on Ru-based catalysts, J. Phys. Chem. B 108 (2004) 7253–7262.
[214] M.C. Wu, D.W. Goodman, High-resolution electron energy-loss measurements of sticking coefficients of methane decomposition on Ru(0 0 0 1), Surf. Sci. Lett. 306 (1994) L529–533.
[215] A.E.B. Presland, P.L. Warker Jr., Growth of single-crystal graphite by pyrolysis of acetylene over metals, Carbon 7 (1969) 1–8.
[216] L.B. Avdeeva, O.V. Goncharova, D.I. Kochubey, V.I. Zaikovskii, L.M. Plyasova, B.N. Novgorodov, S.K. Shaikhutdinov, Coprecipitated Ni–alumina and Ni–Cu–alumina catalysts of methane decomposition and carbon decomposition. II. Evolution of the catalysts in reaction, Appl. Catal. A: Gen. 141 (1996) 117–129.
[217] H. Yoshida, S. Takeda, T. Uchiyama, H. Kohno, Y. Homma, Atomic-scale in-situ observation of carbon nanotube growth from solid state iron carbide nanoparticles, Nano Lett. 8 (2008) 2082–2086.
[218] W.L. Holstein, The roles of ordinary and soret diffusion in the metal-catalyzed formation of filamentous carbon, J. Catal. 152 (1995) 42–51.
[219] C.P. Deck, K. Vecchio, Prediction of carbon nanotube growth success by the analysis of carbon-catalyst binary phase diagrams, Carbon 44 (2006) 267–275.
[220] S. Hofmann, G. Csanyi, A.C. Ferrari, M.C. Payne, J. Robertson, Surface diffusion: the low activation energy path for nanotube growth, Phys. Rev. Lett. 95 (2005) 036101-1–36101-4.
[221] D.J. Siegel, J.C. Hamilton, First-principles study of the solubility, diffusion, and clustering of C in Ni, Phys. Rev. B 68 (2003) 094105-1–094105-7.
[222] D.J. Siegel, J.C. Hamilton, Computational study of carbon segregation and diffusion within a nickel grain boundary, Acta Mater. 53 (2005) 87–96.
[223] F. Abild-Pedersen, J.K. Norskov, J.R. Rostrup-Nielsen, J. Sehested, S. Helveg, Mechanisms for catalytic carbon nanofiber growth studied by ab initio density functional theory calculations, Phys. Rev. B 73 (2006), 115419-1–115419-13.
[224] P.L. Hansen, S. Helveg, A.K. Datye, Atomic-scale Imaging of supported metal nanocluster catalysts in the working state, Adv. Catal. 50 (2006) 77–95.
[225] J.L. Pinilla, I. Suelves, M.J. Lazaro, R. Moliner, J.M. Palacios, Activity of NiCuAl catalyst in methane decomposition studied using a thermobalance and the structural changes in the Ni and the deposited carbon, Int. J. Hydrogen Energy 33 (2008) 2515–2524.
[226] R.A. Buyanov, V.V. Chesnokov, A.D. Afanasev, V.S. Babenko, Carbide mechanism of carbon deposition on iron–chromium dehydrogenation catalysts and properties of the deposit, Kinet. Katal. 18 (1977) 1021–1028.
[227] V.V. Chesnokov, R.A. Buyanov, The formation of carbon filaments upon decomposition of hydrocarbons catalysed by iron subgroup metals and their alloys, Russ. Chem. Rev. 69 (2000) 623–638.
[228] M.T. Taveres, C.A. Bernardo, I. Alstrup, J.R. Rostrup-Nielsen, Reactivity of carbon deposited on nickel–copper alloy catalysts from the decomposition of methane, J. Catal. 100 (1986) 545–548.
[229] I. Alstrup, M.T. Taveres, Kinetics of carbon formation from $CH_4 + H_2$ on silica-supported nickel and Ni–Cu catalysts, J. Catal. 139 (1993) 513–524.
[230] P.K. de Bokx, A.J.H.M. Kock, E. Boellaard, W. Klop, J.W. Geus, The formation of filamentous carbon on iron and nickel catalysts. I. Thermodynamics, J. Catal. 96 (1985) 454–467.
[231] A.J.H.M. Kock, P.K. de Bokx, E. Boellaard, W. Klop, J.W. Geus, The formation of filamentous carbon on iron and nickel catalysts. II. Mechanism, J. Catal. 96 (1985) 468–480.
[232] E. Boellaard, P.K.D. de Bokx, A.J.H.M. Kock, J.W. Geus, The formation of filamentous carbon on iron and nickel catalysts. III. Morphology, J. Catal. 96 (1985) 481–490.
[233] U. Narkiewicz, W. Arabczyk, W. Konicki, Kinetics of carbon deposit formation by methane decomposition on nanocrystalline iron carbide, Fullerenes Nanotubes Carbon Nanostruct. 13 (2005) 99–105.
[234] S. Hofmann, R. Sharma, C. Ducati, G.H. Du, C. Mattevi, C. Cepek, M. Cantoro, S. Pisana, A. Parvez, F. Cervantes-Sodi, A.C. Ferrari, R. Dunin-Borkowski, S. Lizzit, L. Petaccia, A. Goldoni, J. Robertson, In situ observations of catalyst dynamics during surface-bound carbon nanotube nucleation, Nano Lett. 7 (2007) 602–608.
[235] D.X. Li, Y.D. Li, In situ XRD study of methane catalytic decomposition on Fe catalyst, in: The 14th National Congress on Catalysis of China, 2008, p. 109.
[236] M. Lin, T.J.P. Ying, C. Boothroyd, K.P. Loh, E.S. Tok, Y.L. Foo, Direct observation of single-walled carbon nanotube growth at the atomistic scale, Nano Lett. 6 (2006) 449–452.
[237] D. Chen, K.O. Christensen, E. Ochoa-Fernandez, Z.X. Yu, B. Totdal, N. Latorre, A. Monzon, A. Holmen, Synthesis of carbon nanofibers: effects of Ni crystal size during methane decomposition, J. Catal. 229 (2005) 82–96.
[238] R.T. Yang, K.L. Yang, Evidence for temperature driven carbon diffusion mechanism of coke deposition on catalysts, J. Catal. 93 (1985) 182–185.
[239] M. Audier, A. Oberlin, M. Oberlin, M. Coulon, L. Bonnetain, Morphology and crystalline order in catalytic carbons, Carbon 19 (1981) 217–224.
[240] M. Audier, M. Coulon, Kinetic and microscopic aspects of catalytic carbon growth, Carbon 23 (1985) 317–323.
[241] T.S. Cale, Nickel crystallite thermometry during ethane hydrogenolysis, J. Catal. 90 (1984) 40–48.
[242] T.S. Cale, J.M. Lawson, Application of catalytic crystallite thermometry to interphase transport studies, Chem. Eng. Commun. 39 (1985) 241–245.
[243] G.G. Tibbetts, M.G. Devour, E.J. Rodda, An adsorption–diffusion isotherm and its application to the growth of carbon filaments on iron catalyst particles, Carbon 25 (1987) 367–375.
[244] W.L. Holstein, M. Boudart, The temperature difference between a supported catalyst particle and its support during exothermic and endothermic catalytic reactions, Revista Latinoamericana de Ingenieria Quimica y Quimica Aplicada 13 (1983) 107–120.
[245] G.G. Tibbetts, Why are carbon filaments tubular? J. Cryst. Growth 66 (1984) 632–638.
[246] R. Sharma, Design and applications of environmental cell transmission electron microscope for in situ observations of gas–solid reactions, Microsc. Microanal. 7 (2001) 494–506.
[247] R. Sharma, P.A. Crozier, R. Marx, K. Weiss, An environmental transmission electron microscope for in-situ observation of chemical processes at the nanometer level, Microsc. Microanal. 9 (2003) 912–913.
[248] M.M.J. Treacy, M. Brown, P. Rez, G.H. Du, R. Sharma, In-situ TEM observations of carbon nanotube growth by the catalytic decomposition of acetylene, Microsc. Microanal. 12 (2006) 786–787.
[249] R. Sharma, Z. Iqbal, In situ observations of carbon nanotube formation using environmental transmission electron microscopy, Appl. Phys. Lett. 84 (2004) 990–992.
[250] R. Sharma, P. Rez, M. Brown, G.H. Du, M.M.J. Treacy, Dynamic observations of the effect of pressure and temperature conditions on the selective synthesis of carbon nanotubes, Nanotechnology 18 (2007), 125602-1–125602-8.
[251] P.L. Gai, R. Sharma, F.M. Ross, Environmental (S)TEM studies of gas–liquid–solid interactions under reaction conditions, MRS Bull. 33 (2008) 107–114.
[252] R. Sharma, P. Rez, M.M.J. Treacy, S.J. Stuart, In situ observation of the growth mechanisms of carbon nanotubes under diverse reaction conditions, J. Electron. Spectrosc. 54 (2005) 231–237.
[253] Y.F. Sun, Z.J. Sui, J.H. Zhou, P. Li, X.G. Zhou, D. Chen, Catalytic decomposition of methane over supported Ni catalysts with different particle sizes, Asia-Pac. J. Chem. Eng. 4 (2009) 814–820.
[254] M.A. Ermakova, D.Y. Ermakov, G.G. Kushinov, Effective catalysts for direct cracking of methane to produce hydrogen and filamentous carbon. Part I. Nickel catalysts, Appl. Catal. A: Gen. 201 (2000) 61–70.
[255] M.A. Ermakova, D.Y. Ermakov, L.M. Plyasova, G.G. Kuvshinov, XRD studies of evolution of catalytic nickel nanoparticles during synthesis of filamentous carbon from methane, Catal. Lett. 62 (1999) 93–97.
[256] J.L. Pinilla, I. Suelves, M.J. Lazaro, R. Moliner, J.M. Palacios, Influence of nickel crystal domain size on the behaviour of Ni and NiCu catalysts for the methane decomposition reaction, Appl. Catal. A: Gen. 363 (2009) 199–207.
[257] K.C. Khulbe, R.S. Mann, Nature of Ni–Cu alloys and their role in chemical reactions, Catal. Rev. Sci. Eng. 24 (1982) 311–328.
[258] X.P. Zhang, C.J. Liu, Tiehejin cidian (Dictionary of Iron Alloys), 317, Liaoning Keji Publisher, Shenyang, China, 1996.
[259] Y. Qi, T. Cagin, W.L. Johnson, W.A. Goddard III, Melting and crystallization in Ni nanoclusters: the mesoscale regime, J. Chem. Phys. 115 (2001) 385–394.
[260] L. Wang, H. Yang, X.F. Bian, X.Z. Li, Melting of Ni clusters with free surface, Acta Phys. Chim. Sin. 17 (2001) 1097–1101.
[261] C.L. Cheung, A. Kurtz, H.K. Park, C.M. Lieber, Diameter-controlled synthesis of carbon nanotubes, J. Phys. Chem. B 106 (2002) 2429–2433.
[262] Y. Li, J. Liu, Y.Q. Wang, Z.L. Wang, Preparation of monodispersed Fe–Mo nanoparticles as the catalyst for CVD synthesis of Carbon Nanotubes, Chem. Mater. 13 (2001) 1008–1014.
[263] E. Lamouroux, P. Serp, P. Kalck, Catalytic routes towards single wall carbon nanotubes, Catal. Rev. Sci. Eng. 49 (2007) 341–405.
[264] A.M. Rashidi, M.M. Akbarnejad, A.A. Khodadadi1, Y. Mortazavi, A. Ahmadpourd, Single-wall carbon nanotubes synthesized using organic additives to Co–Mo catalysts supported on nanoporous MgO, Nanotechnology 18 (2007), 315605-1–315605-5.
[265] Y.M. Li, W. Kim, Y.G. Zhang, M. Rolandi, D.W. Wang, H.J. Dai, Growth of single-walled carbon nanotubes from discrete catalytic nanoparticles of various sizes, J. Phys. Chem. B 105 (2001) 11424–11431.
[266] Y. Zhang, Y. Li, W. Kim, D. Wang, H. Dai, Imaging as-grown single-walled carbon nanotubes originated from isolated catalytic nanoparticles, Appl. Phys. A 74 (2002) 325–328.
[267] H.C. Choi, W. Kim, D.W. Wang, H.J. Dai, Delivery of catalytic metal species onto surfaces with dendrimer carriers for the synthesis of carbon nanotubes with narrow diameter distribution, J. Phys. Chem. B 106 (2002) 12361–12365.
[268] A. Govindaraj, E. Flahaut, C. Laurent, A. Peigney, A. Rousset, C.N.R. Rao, An investigation of carbon nanotubes obtained from the decomposition of methane over reduced $Mg_{1-x}M_xAl_2O_4$ spinel catalysts, J. Mater. Res. 14 (1999) 2567–2576.
[269] E. Flahaut, A. Govindaraj, A. Peigney, C. Laurent, A. Rousset, C.N.R. Rao, Synthesis of single-walled carbon nanotubes using binary (Fe, Co, Ni) alloy

nanoparticles prepared in situ by the reduction of oxide solid solutions, Chem. Phys. Lett. 300 (1999) 236–242.
[270] G.Q. Ning, F. Wei, Q. Wen, G.H. Luo, Y. Wang, Y. Jin, Improvement of Fe/MgO catalysts by calcination for the growth of single- and double-walled carbon nanotubes, J. Phys. Chem. B 110 (2006) 1201–1205.
[271] S.J. Tauster, S.C. Fung, R.T.K. Baker, J.A. Horsley, Strong interactions in supported-metal catalysts, Science 13 (1981) 1121–1125.
[272] S.J. Tauster, Strong metal–support interactions, Acc. Chem. Res. 20 (1987) 389–394.
[273] Y. Li, B.C. Zhang, X.L. Tang, Y.D. Xu, W.J. Shen, Hydrogen production from methane decomposition over Ni/CeO_2 catalysts, Catal. Commun. 7 (2006) 380–386.
[274] X.N. Li, Y. Zhang, K.J. Smith, Metal–support interaction effects on the growth of filamentous carbon over Co/SiO_2 catalysts, Appl. Catal. A: Gen 264 (2004) 81–91.
[275] X.L. Zhu, D.G. Cheng, P.Y. Kuai, Catalytic decomposition of methane over Ni/Al_2O_3 catalysts: effect of plasma treatment on carbon formation, Energy Fuels 22 (2008) 1480–1484.
[276] H. Ago, K. Nakamura, N. Uehara, M. Tsuji, Roles of metal–support interaction in growth of single- and double-walled carbon nanotubes studied with diameter-controlled iron particles supported on MgO, J. Phys. Chem. B 108 (2004) 18908–18915.
[277] P. Forzatti, L. Lietti, Catalyst deactivation, Catal. Today 52 (1999) 165–181.
[278] J.T. Richardson, Principles of Catalyst Development, Springer, 1989.
[279] T.J. Zhang, M.D. Amiridis, Hydrogen production via the direct cracking of methane over silica-supported nickel catalysts, Appl. Catal. A: Gen. 167 (1998) 161–172.
[280] B. Gaudernack, S. Lynum, Hydrogen from natural gas without release of CO_2 to the atmosphere, Int. J. Hydrogen Energy 23 (1998) 1087–1093.
[281] E. Ruckenstein, Y.H. Hu, Catalytic preparation of narrow pore size distribution mesoporous carbon, Carbon 36 (1998) 269–275.
[282] S. Takenaka, E. Kato, Y. Tomikubo, K. Otsuka, Structural change of Ni species during the methane decomposition and the subsequent gasification of deposited carbon with CO_2 over supported Ni catalysts, J. Catal. 219 (2003) 176–185.
[283] S.G. Zavarukhin, G.G. Kuvshinov, The kinetic model of formation of nanofibrous carbon from CH_4–H_2 mixture over a high-loaded nickel catalyst with consideration for the catalyst deactivation, Appl. Catal. A: Gen. 272 (2004) 219–227.
[284] J. Salmones, J.A. Wang, M.A. Valenzuela, E. Sanchez, A. Garcia, Pore geometry influence on the deactivation behavior of Ni-based catalysts for simultaneous production of hydrogen and nanocarbon, Catal. Today 148 (2009) 134–139.
[285] J. Ashok, S.N. Kumar, M. Subrahmanyam, A. Venugopal, Production of CO_x free hydrogen by catalytic decomposition of methane over Ni/HY catalysts, Catal. Lett. 118 (2007) 139–145.
[286] J. Ashok, S.N. Kumar, M. Subrahmanyam, A. Venugopal, Pure H_2 production by decomposition of methane over Ni supported on hydroxyapatite catalysts, Catal. Lett. 121 (2008) 283–290.
[287] S. Takenaka, H. Ogihara, I. Yamanaka, K. Otsuka, Decomposition of methane over supported-Ni catalysts: effects of the supports on the catalytic lifetime, Appl. Catal. A: Gen. 217 (2001) 101–110.
[288] Y. Zhang, K.J. Smith, Carbon formation thresholds and catalyst deactivation during CH_4 decomposition on supported Co and Ni catalysts, Catal. Lett. 95 (2004) 7–12.
[289] J.L. Chen, X.Z. Zhou, L. Cao, Y.D. Li, CO_x-free hydrogen and carbon nanofibers production by decomposition of methane on Fe, Co and Ni metal catalysts, Stud. Surf. Sci. Catal. 147 (2004) 73–78.
[290] J. Hagen (Ed.), Industrial Catalysis: A Practical Approach, second edition, WILEY-WCH, 2006.
[291] S.H.S. Zein, A.R. Mohamed, $Mn/Ni/TiO_2$ catalyst for the production of hydrogen and carbon nanotubes from methane decomposition, Energy Fuels 18 (2004) 1336–1345.
[292] H. Ichi-oka, N. Higashi, Y. Yamada, T. Miyake, T. Suzuki, Carbon nanotube and nanofiber syntheses by the decomposition of methane on group 8–10 metal-loaded MgO catalysts, Diam. Relat. Mater. 16 (2007) 1121–1125.
[293] M.A. Ermakova, D.Y. Ermakov, Ni/SiO_2 and Fe/SiO_2 catalysts for production of hydrogen and filamentous carbon via methane decomposition, Catal. Today 77 (2002) 225–235.
[294] S. Takenaka, M. Serizawa, K. Otsuka, Formation of filamentous carbons over supported Fe catalysts through methane decomposition, J. Catal. 222 (2004) 520–531.
[295] L.B. Avdeeva, T.V. Reshetenko, Z.R. Ismagilov, V.A. Likholobov, Iron-containing catalysts of methane decomposition: accumulation of filamentous carbon, Appl. Catal. A: Gen. 228 (2002) 53–63.
[296] P. Zarabadi-Poor, A. Badiei, A.A. Yousefi, B.D. Fahlman, A. Abbasi, Catalytic chemical vapour deposition of carbon nanotubes using Fe-doped alumina catalysts, Catal. Today 150 (2010) 100–106.
[297] L.B. Avdeeva, D.I. Kochubey, S.K. Shaikhutdinov, Cobalt catalysts of methane decomposition: accumulation of the filamentous carbon, Appl. Catal. A: Gen. 117 (1999) 43–51.
[298] A. Fonseca, K. Hernadi, J.B. Nagy, D. Bernaerts, A.A. Lucas, Optimization of catalytic production and purification of buckytubes, J. Mol. Catal. A: Chem. 107 (1996) 159–168.
[299] Y.D. Li, J.L. Chen, L. Chang, Y.N. Qin, The doping effect of copper on the catalytic growth of carbon fibers from methane over a Ni/Al_2O_3 catalyst prepared from Feitknecht compound precursor, J. Catal. 178 (1998) 76–83.
[300] I. Suelves, M.J. Lazaro, R. Moliner, Y. Echegoyen, J.M. Palacios, Characterization of NiAl and NiCuAl catalysts prepared by different methods for hydrogen production by thermo catalytic decomposition of methane, Catal. Today 116 (2006) 271–280.
[301] I. Suelves, M.J. Lazaro, R. Moliner, Y. Echegoyen, J.M. Palacios, Hydrogen production by catalytic decomposition of methane: Ni and Ni–Cu catalysts development, in: 2nd European Hydrogen Energy Conference, November, Zaragoza, Spain, 2005, p. 22.
[302] A.F. Cunha, J.J.M. Orfao, J.L. Figueiredo, Methane decomposition on Ni–Cu alloyed Raney-type catalysts, Int. J. Hydrogen Energy 34 (2009) 4763–4772.
[303] A.F. Cunha, J.J.M. Orfao, J.L. Figueiredo, Methane decomposition on Fe–Cu Raney-type catalysts, Fuel Process. Technol. 90 (2009) 1234–1240.
[304] J. Ashok, P.S. Reddy, G. Raju, M. Subrahmanyam, A. Venugopal, Catalytic decomposition of methane to hydrogen and carbon nanofibers over $Ni–Cu–SiO_2$ Catalysts, Energy Fuels 23 (2009) 5–13.
[305] A. Monzon, N. Latorre, T. Ubieto, C. Royo, E. Romeo, J.I. Villacampa, L. Dussault, J.C. Dupin, C. Guimon, M. Montioux, Improvement of activity and stability of Ni–Mg–Al catalysts by Cu addition during hydrogen production by catalytic decomposition of methane, Catal. Today 116 (2006) 264–270.
[306] M.J. Lazaro, Y. Echegoyen, C. Alegre, I. Suelves, R. Moliner, J.M. Palacios, TiO_2 as textural promoter on high loaded Ni catalysts for methane decomposition, Int. J. Hydrogen Energy 33 (2008) 3320–3329.
[307] H. Baker (Ed.), ASM Handbook, Volume 3. Alloy Phase Diagrams, ASM International, New York, 1992.
[308] A.R. Naghash, Z. Xu, T.H. Etsell, Coprecipitation of nickel–copper–aluminum takovite as catalyst precursors for simultaneous production of carbon nanofibers and hydrogen, Chem. Mater. 17 (2005) 815–821.
[309] A.R. Naghash, T.H. Etsell, S. Xu, XRD and XPS study of Cu–Ni interactions on reduced copper–nickel–aluminum oxide solid solution catalysts, Chem. Mater. 18 (2006) 2480–2488.
[310] I. Gonzalez, J.C. de Jesus, C.U. de Navarro, M. Garcia, Effect of Cu on Ni nanoparticles used for the generation of carbon nanotubes by catalytic cracking of methane, Catal. Today 149 (2010) 352–357.
[311] V.V. Chesnokov, A.S. Chichkan, Production of hydrogen by methane catalytic decomposition over $Ni–Cu–Fe/Al_2O_3$ catalyst, Int. J. Hydrogen Energy 34 (2009) 2979–2985.
[312] S. Takenaka, Y. Shigeta, E. Tanabe, K. Otsuka, Methane decomposition into hydrogen and carbon nanofibers over supported Pd–Ni catalysts, J. Catal. 220 (2003) 468–477.
[313] N. Shah, D. Panjala, G.P. Huffman, Hydrogen production by catalytic decomposition of methane, Energy Fuels 15 (2001) 1528–1534.
[314] H. Ogihara, S. Takenaka, I. Yamanaka, E. Tanabe, A. Genseki, K. Otsuka, Formation of highly concentrated hydrogen through methane decomposition over Pd-based alloy catalysts, J. Catal. 238 (2006) 353–360.
[315] J.L. Chen, Y.H. Qiao, Y.D. Li, Promoting effects of doping ZnO into coprecipitated $Ni–Al_2O_3$ catalyst on methane decomposition to hydrogen and carbon nanofibers, Appl. Catal. A: Gen. 337 (2008) 148–154.
[316] O.A. Gonzalez, M.A. Valenzuela, J.A. Wang, Catalytic decomposition of methane over cerium-doped Ni catalysts, Mater. Res. Soc. Symp. Proc. 885E (2006), 0885-A09-49.1–0885-A09-49.6.
[317] B. Zapata, M.A. Valenzuel, J. Palacios, E. Torres-Garcia, Effect of Ca, Ce or K oxide addition on the activity of Ni/SiO_2 catalysts for the methane decomposition reaction, Int. J. Hydrogen Energy 35 (2010) 12091–12097.
[318] W.Z. Qian, T. Liu, F. Wei, Z.W. Wang, D.Z. Wang, Y.D. Li, Carbon nanotubes with large cores produced by adding sodium carbonate to the catalyst, Carbon 41 (2003) 2683–2686.
[319] E.C. Kruissink, H.L. Pelt, J.R.H. Ross, L.L. van Reuen, The effect of sodium on the methanation activity of nickel/alumina coprecipitated catalysts, Appl. Catal. 1 (1981) 23–29.
[320] S.T. Hussain, S. Gul, M. Mazhar, D.H. Anjum, F. Larachi, Effect of surface structure on the catalytic behavior of Ni:Cu/Al and Ni:Cu:K/Al catalysts for methane decomposition, J. Nat. Gas Chem. 17 (2008) 374–382.
[321] G. Italiano, C. Espro, F. Arena, A. Parmaliana, F. Frusteri, Doped Ni thin layer catalysts for catalytic decomposition of natural gas to produce hydrogen, Appl. Catal. A: Gen. 365 (2009) 122–129.
[322] H. Ago, N. Uehara, N. Yoshihara, M. Tsuji, M. Yumura, N. Tomonaga, T. Setoguchi, Gas analysis of the CVD process for high yield growth of carbon nanotubes over metal-supported catalysts, Carbon 44 (2006) 2912–2918.
[323] S. Tang, Z. Zhong, Z. Xiong, L. Sun, L. Liu, J. Lin, Z.X. Shen, K.L. Tan, Controlled growth of single-walled carbon nanotubes by catalytic decomposition of CH_4 over Mo/Co/MgO catalysts, Chem. Phys. Lett. 350 (2001) 19–26.
[324] L. Ni, K.J. Kuroda, L.P. Zhou, T. Kizuka, K. Ohta, K. Matsuishi, J.J. Nakamura, Kinetic study of carbon nanotube synthesis over Mo/Co/MgO catalysts, Carbon 44 (2006) 2265–2272.
[325] Y.J. Yoon, J.C. Bae, H.K. Baik, S.J. Cho, S.J. Lee, K.M. Song, N.S. Myung, Nucleation and growth control of carbon nanotubes in CVD process, Physica B 323 (2002) 318–320.
[326] X. Wang, W.B. Yue, M.S. He, M.H. Liu, J. Zhang, Z.F. Liu, Bimetallic catalysts for the efficient growth of SWNTs on surfaces, Chem. Mater. 16 (2004) 799–805.
[327] M.L. Toebes, J.H. Bitter, A.J. van Dillen, K.P. de Jong, Impact of the structure and reactivity of nickel particles on the catalytic growth of carbon nanofibers, Catal. Today 76 (2002) 33–42.
[328] G. Bonura, O.D. Blasi, L. Spadaro, F. Arena, F. Frusteri, A basic assessment of the reactivity of Ni catalysts in the decomposition of methane for the production of "CO_x-free" hydrogen for fuel cells application, Catal. Today 116 (2006) 298–303.

[329] Y.H. Hu, E. Ruckenstein, Binary MgO-based solid solution catalysts for methane conversion to syngas, Catal. Rev. Sci. Eng. 44 (2002) 423–453.
[330] W. Gac, A. Denis, T. Borowiecki, L. Kepinski, Methane decomposition over Ni–MgO–Al_2O_3 catalysts, Appl. Catal. A: Gen. 357 (2009) 236–243.
[331] Z.R. Ismagilov, N.V. Shikina, V.N. Kruchinin, N.A. Rudina, V.A. Ushakov, N.T. Vasenin, H.J. Veringa, Development of methods of growing carbon nanofibers on silica glass fiber supports, Catal. Today 102–103 (2005) 85–93.
[332] L. Chen, H.T. Liu, K. Yang, J.K. Wang, X.L. Wang, Catalytic synthesis of carbon nanotubes from the decomposition of methane over a Ni–Co/La_2O_3 catalyst, Can. J. Chem. 87 (2009) 47–53.
[333] M. Kuras, Y. Zimmermann, C. Petit, Reactivity of perovskite-type precursor in MWCNTs synthesis, Catal. Today 138 (2008) 55–61.
[334] G.S. Gallego, J. Barrault, C. Batiot-Dupeyrat, F. Mondragon, Production of hydrogen and MWCNTs by methane decomposition over catalysts originated from $LaNiO_3$ perovskite, Catal. Today 149 (2010) 365–371.
[335] M.E. Rivas, J.L.G. Fierro, R. Guil-Lopez, M.A. Pena, V. La Parola, M.R. Goldwasser, Preparation and characterization of nickel-based mixed-oxides and their performance for catalytic methane decomposition, Catal. Today 133–135 (2008) 367–373.
[336] B.C. Liu, S.H. Tang, Z.L. Yu, B.L. Zhang, T. Chen, S.Y. Zhang, Catalytic growth of single-walled carbon nanotubes with a narrow distribution of diameters over Fe nanoparticles prepared in situ by the reduction of $LaFeO_3$, Chem. Phys. Lett. 357 (2002) 297–300.
[337] A.F. Cunha, N. Mahata, J.J.M. Orfao, J.L. Figueiredo, Methane decomposition on La_2O_3-promoted Raney-type Fe catalysts, Energy Fuels 23 (2009) 4047–4050.
[338] J.L. Figueiredo, J.J.M. Orfao, A.F. Cunha, Hydrogen production via methane decomposition on Raney-type catalysts, Int. J. Hydrogen Energy 35 (2010) 9795–9800.
[339] T.V. Reshetenko, L.B. Avdeeva, Z.R. Ismagilov, A.L. Chuvilin, Catalytic filamentous carbon as supports for nickel catalysts, Carbon 42 (2004) 143–178.
[340] T.V. Reshetenko, L.B. Avdeeva, Z.R. Ismagilov, A.L. Chuvilin, V.B. Fenelonov, Catalytic filamentous carbons-supported Ni for low-temperature methane decomposition, Catal. Today 102–103 (2005) 115–120.
[341] S.K. Shaikhutdinov, L.B. Avdeeva, B.N. Novgorodov, V.I. Zaikovskii, D.I. Kochubey, Nickel catalysts supported on carbon nanofibers: structure and activity in methane decomposition, Catal. Lett. 47 (1997) 35–42.
[342] J. Ashok, S.N. Kumar, A. Venugopal, V.D. Kumari, M. Subrahmanyam, CO_x-free H_2 production via catalytic decomposition of CH_4 over Ni supported on zeolite catalysts, J. Power Sources 164 (2007) 809–814.
[343] J.C. Guevara, J.A. Wang, L.F. Chen, M.A. Valenzuela, P. Salas, A. García-Ruiz, J.A. Toledo, M.A. Cortes-Jácome, C. Angeles-Chavez, O. Novaro, Ni/Ce-MCM-41 mesostructured catalysts for simultaneous production of hydrogen and nanocarbon via methane decomposition, Int. J. Hydrogen Energy 35 (2010) 3509–3521.
[344] J. Ziebro, I. Lukasiewicz, E. Borowiak-Palen, B. Michalkiewicz, Low temperature growth of carbon nanotubes from methane catalytic decomposition over nickel supported on a zeolite, Nanotechnology 21 (2010), 145308-1–145308-6.
[345] J.M. Jehng, W.C. Tung, C.H. Kuo, The formation mechanisms of multi-wall carbon nanotubes over the Ni modified MCM-41 catalysts, J. Porous Mater. 15 (2008) 43–51.
[346] T.V. Choudhary, C. Sivadinarayana, A. Klinghoffer, D.W. Goodman, Catalytic decomposition of methane: towards production of CO-free hydrogen for fuel cells, Stud. Surf. Sci. Catal. 136 (2001) 197–202.
[347] L.G. Tang, D. Yamaguchi, N. Burke, D. Trimm, K. Chiang, Methane decomposition over ceria modified iron catalysts, Catal. Commun. 11 (2010) 1215–1219.
[348] E. Odier, Y. Schuurman, C. Mirodatos, Non-stationary catalytic cracking of methane over ceria-based catalysts: mechanistic approach and catalyst optimization, Catal. Today 127 (2007) 230–237.
[349] Q.W. Li, H. Yan, Y. Cheng Yan, J. Zhang, Z.F. Liu, A scalable CVD synthesis of high-purity single-walled carbon nanotubes with porous MgO as support material, J. Mater. Chem. 12 (2002) 1179–1183.
[350] G.Q. Ning, Y. Liu, F. Wei, Q. Wen, G.H. Luo, Porous and lamella-like Fe/MgO catalysts prepared under hydrothermal conditions for high-yield synthesis of double-walled carbon nanotubes, J. Phys. Chem. C 111 (2007) 1969–1975.
[351] J.Q. Nie, W.Z. Qian, Q. Zhang, Q. Wen, F. Wei, Very high-quality single-walled carbon nanotubes grown using a structured and tunable porous Fe/MgO catalyst, J. Phys. Chem. C 113 (2009) 20178–20183.
[352] M. Paillet, V. Jourdain, P. Poncharal, J.L. Sauvajol, A. Zahab, Versatile synthesis of individual single-walled carbon nanotubes from nickel nanoparticles for the study of their physical properties, J. Phys. Chem. B 108 (2004) 17112–17118.
[353] J. Kong, H.T. Soh, A.M. Cassell, C.F. Quate, H.J. Dai, Synthesis of individual single-walled carbon nanotubes on patterned silicon wafers, Nature 395 (1998) 878–881.
[354] C.N. He, N.Q. Zhao, X.W. Du, C.S. Shi, J.J. Li, F. He, Characterization of bamboo-shaped CNTs prepared using deposition–precipitation catalyst, Mater. Sci. Eng. A 479 (2008) 248–252.
[355] P. Wang, E. Tanabe, K. Ito, J. Jia, H. Morioka, T. Shishido, K. Takehira, Filamentous carbon prepared by the catalytic pyrolysis of CH_4 on Ni/SiO_2, Appl. Catal. A: Gen. 231 (2002) 35–44.
[356] M.A. Ermakova, D.Y. Ermakov, G.G. Kuvshinov, L.M. Plyasova, New nickel catalysts for the formation of filamentous carbon in the reaction of methane decomposition, J. Catal. 187 (1999) 77–84.
[357] Y. Echegoyen, I. Suelves, M.J. Lazaro, M.L. Sanjuan, R. Moliner, Thermo catalytic decomposition of methane over Ni–Mg and Ni–Cu–Mg catalysts: effect of catalyst preparation method, Appl. Catal. A: Gen. 333 (2007) 229–237.
[358] M.J. Lazaro, Y. Echegoyen, I. Suelves, J.M. Palacios, R. Moliner, Decomposition of methane over Ni–SiO_2 and Ni–Cu–SiO_2 catalysts: effect of catalyst preparation method, Appl. Catal. A: Gen. 329 (2007) 22–29.
[359] M. Su, B. Zheng, J. Liu, A scalable CVD method for the synthesis of single-walled carbon nanotubes with high catalyst productivity, Chem. Phys. Lett. 322 (2000) 321–326.
[360] L.Y. Piao, J.L. Chen, Y.D. Li, Carbon nanotubes via methane decomposition on an alumina supported cobalt aerogel catalyst, China Particuol. 1 (2003) 266–270.
[361] G.B. Nuernberg, H.V. Fajardo, D.Z. Mezalira, T.J. Casarin, L.F.D. Probst, N.L.V. Carreno, Preparation and evaluation of Co/Al_2O_3 catalysts in the production of hydrogen from thermo-catalytic decomposition of methane: influence of operating conditions on catalyst performance, Fuel 87 (2008) 1698–1704.
[362] C. Valles, M. Perez-Mendoz, W.K. Maser, M.T. Martinez, L. Alvarez, J.L. Sauvajol, A.M. Benito, Effects of partial and total methane flows on the yield and structural characteristics of MWCNTs produced by CVD, Carbon 47 (2009) 998–1004.
[363] S.K. Shaikhutdinov, L.B. Avdeeva, O.V. Goncharova, D.I. Kochubey, B.N. Novgorodov, L.M. Plyasova, Coprecipitated Ni–Al and Ni–Cu–Al catalysts for methane decomposition and carbon decomposition. I. genesis of calcined and reduced catalysts, Appl. Catal. A: Gen. 126 (1995) 125–139.
[364] I. Suelves, J.L. Pinilla, M.J. Lazaro, R. Moliner, J.M. Palacios, Effects of reaction conditions on hydrogen production and carbon nanofiber properties generated by methane decomposition in a fixed bed reactor using a NiCuAl catalyst, J. Power Sources 192 (2009) 35–42.
[365] J.L. Pinilla, R. Moliner, I. Suelves, M.J. Lazaro, Y. Echegoyen, J.M. Palacios, Production of hydrogen and carbon nanofibers by thermal decomposition of methane using metal catalysts in a fluidized bed reactor, Int. J. Hydrogen Energy 32 (2007) 4821–4829.
[366] E.C. Kayser, Preparing a catalyzer for converting unsaturated fatty acids into saturated compounds, US patent 1004034, 1911.
[367] J.R.H. Ross, M.C.F. Steel, A. Zeini-Isfahani, Evidence for the participation of surface nickel aluminate sites in the steam reforming of methane over nickel/alumina catalysts, J. Catal. 52 (1978) 280–290.
[368] G. van Veen, E.C. Kruissink, E.B.M. Doesburg, J.R.H. Ross, L.L. van Reijen, The effect of preparation conditions on the activity and stability of coprecipitated Ni/Al_2O_3 catalysts for the methanation of carbon monoxide, React. Kinet. Catal. Lett. 9 (1978) 143–148.
[369] E.C. Kruissink, L.L. van Reijen, J.R.H. Ross, Coprecipitated nickel–alumina catalysts for methanation at high temperature. Part 1. Chemical composition and structure of the precipitates, J. Chem. Soc. Faraday Trans. I 77 (1981) 649–663.
[370] L.E. Alzamora, J.R.H. Ross, E.C. Kruissink, L.L. van Reijen, Coprecipitated nickel–alumina catalysts for methanation at high temperature. Part 2. Variation of total and metallic areas as a function of sample composition and method of pretreatment, J. Chem. Soc. Faraday Trans. I 77 (1981) 665–681.
[371] H.G.L. Lansink Rotgerink, H. Bosch, J.G. van Ommen, J.R.H. Ross, The effect of Ni–Al ratio on the properties of coprecipitated nickel–alumina catalysts with high nickel contents, Appl. Catal. 27 (1986) 41–53.
[372] J.R.H. Ross, Metal catalysed methanation and steam reforming, in: G.C. Bond, G. Webb (Eds.), Catalysis. Specialist Periodical Reports, vol. 7, Royal Society of Chemistry, London, 1985, pp. 1–45.
[373] J.S. Valente, J. Hernandez-Cortez, M.S. Cantu, G. Ferrat, E. Lopez-Salinas, Calcined layered double hydroxides Mg–Me–Al (Me: Cu, Fe, Ni, Zn) as bifunctional catalysts, Catal. Today 150 (2010) 340–345.
[374] F. Cavani, F. Trifiro, A. Vaccari, Hydrotalcite-type anionic clays: preparation, properties and applications, Catal. Today 11 (1991) 173–301.
[375] D.P. Debecker, E.M. Gaigneaux, G. Busca, Exploring, tuning, and exploiting the basicity of hydrotalcites for applications in heterogeneous catalysis, Chem. Eur. J. 15 (2009) 3920–3935.
[376] P. Courty, C. Marcilly, A scientific approach to the preparation of bulk mixed oxide catalysts, Stud. Surf. Sci. Catal. 16 (1983) 485–519.
[377] A. Vaccari, Clays and catalysis: a promising future, Appl. Clay Sci. 14 (1999) 161–198.
[378] S.M. Auerbach, K.A. Carrado, P.K. Dutta (Eds.), Handbook of Layered Materials, Marcel Dekker, Inc., 2004.
[379] X. Duan, D.G. Evans (Eds.), Layered Double Hydroxides, Springer, 2006.
[380] X.X. Guo, F.Z. Zhang, D.G. Evans, X. Duan, Layered double hydroxide films: synthesis, properties and applications, Chem. Commun. 46 (2010) 5197–5210.
[381] B.F. Sels, D.E. de Vos, P.A. Jacobs, Hydrotalcite-like anionic clays in catalytic organic reactions, Catal. Rev. Sci. Eng. 43 (2001) 443–488.
[382] D. Tichit, C. Gerardin, R. Durand, B. Coq, Layered double hydroxides: precursors for multifunctional catalysts, Top. Catal. 39 (2006) 89–96.
[383] D.C. Puxley, I.J. Kitchener, C. Komodromos, N.D. Purkyns, The effect of preparation method upon the structures, stability and metal/support interactions in nickel/alumina catalysts, Stud. Surf. Sci. Catal. 16 (1983) 237–271.
[384] O. Clause, B. Rebours, E. Merlen, F. Trifiro, A. Vaccari, Preparation and characterization of nickel–aluminum mixed oxides obtained by thermal decomposition of hydrotalcite-type precursors, J. Catal. 133 (1992) 231–246.
[385] V.R. Hosemann, A. Preisinger, W. Vogel, Alpha-Fe–$FeAl_2O_4$ mixed crystal in activated ammonia catalysts, Ber. Bunsenges. Phys. Chem. 70 (1966) 796–802.
[386] C.J. Wright, C.G. Windsor, D.C. Puxley, Paracrystallinity in a coprecipitated nickel/alumina catalyst, J. Catal. 78 (1982) 257–261.

[387] E.B.M. Doesburg, P.H.M. de Korte, H. Schaper, L.L. van Reijen, The sintering of coprecipitated nickel alumina catalysts, Appl. Catal. 11 (1984) 155–160.
[388] L. Dussault, J.C. Dupin, C. Guimon, M. Monthioux, N. Latorre, T. Ubieto, E. Romeo, C. Royo, A. Monzon, Development of Ni–Cu–Mg–Al catalysts for the synthesis of carbon nanofibers by catalytic decomposition of methane, J. Catal. 251 (2007) 223–232.
[389] J.L. Chen, Q. Ma, T.E. Rufford, Y.D. Li, Z.H. Zhu, Influence of calcination temperatures of Feitknecht compound precursor on the structure of Ni–Al_2O_3 catalyst and the corresponding catalytic activity in methane decomposition to hydrogen and carbon nanofibers, Appl. Catal. A: Gen. 362 (2009) 1–7.
[390] P. Benito, M. Herrero, F.M. Labajos, V. Rives, C. Royo, N. Latorre, A. Monzon, Production of carbon nanotubes from methane: use of Co–Zn–Al catalysts prepared by microwave-assisted synthesis, Chem. Eng. J. 149 (2009) 455–462.
[391] Q. Zhang, W.Z. Qian, Q. Wen, Y. Liu, D.Z. Wang, F. Wei, The effect of phase separation in Fe/Mg/Al/O catalysts on the synthesis of DWCNTs from methane, Carbon 45 (2007) 1645–1650.
[392] M.Q. Zhao, Q. Zhang, J.Q. Huang, J.Q. Nie, F. Wei, Layered double hydroxides as catalysts for the efficient growth of high quality single-walled carbon nanotubes in a fluidized bed reactor, Carbon 48 (2010) 3260–3270.
[393] M.Q. Zhao, Q. Zhang, X.L. Jia, J.Q. Huang, Y.H. Zhang, F. Wei, Hierarchical composites of single/double-walled carbon nanotubes interlinked flakes from direct carbon deposition on layered double hydroxides, Adv. Funct. Mater. 20 (2010) 677–685.
[394] Q. Zhang, M.Q. Zhao, D.M. Tang, F. Li, J.Q. Huang, B. Liu, W.C. Zhu, Y.H. Zhang, F. Wei, Carbon nanotube-array double helices, Angew. Chem. Int. Ed. 49 (2010) 3642–3645.
[395] A.F. Cunha, J.J.M. Orfao, J.L. Figueiredo, Catalytic decomposition of methane on Raney-type catalysts, Appl. Catal. A: Gen. 348 (2008) 103–112.
[396] Y. Li, B.C. Zhang, X.W. Xie, J.L. Liu, Y.D. Xu, W.J. Shen, Novel Ni catalysts for methane decomposition to hydrogen and carbon nanofibers, J. Catal. 238 (2006) 412–424.
[397] W. Zhang, Q.J. Ge, H.Y. Xu, Influences of precipitate rinsing solvents on Ni catalyst for methane decomposition to CO_x-free hydrogen, J. Phys. Chem. A114 (2010) 3818–3823.
[398] P. Jana, V.A. de la Pena OShea, J.M. Coronado, D.P. Serrano, Cobalt based catalysts prepared by pechini method for CO_2-free hydrogen production by methane decomposition, Int. J. Hydrogen Energy 35 (2010) 10285–10294.
[399] M.C. Demicheli, E.N. Ponzi, O.A. Ferretti, A.A. Yeramian, Kinetics of carbon formation from CH_4–H_2 mixtures on nickel–alumina catalyst, Chem. Eng. J. 46 (1991) 129–136.
[400] I. Alstrup, M.T. Tavares, The kinetics of carbon formation from $CH_4 + H_2$ on a silica-supported nickel catalyst, J. Catal. 135 (1992) 147–155.
[401] S.H.S. Zein, A.R. Mohamed, P.S.T. Sai, Kinetic studies on catalytic decomposition of methane to hydrogen and carbon over Ni/TiO_2 catalyst, Ind. Eng. Chem. Res. 43 (2004) 4864–4870.
[402] I. Alstrup, M.T. Tavares, C.A. Bernardo, O. Sorensen, J.R. Rostrup-Nielsen, Carbon formation on nickel and nickel–copper alloy catalysts, Mater. Corros. 49 (1998) 367–372.
[403] E.R. Gilliland, P. Harriott, Reactivity of deposited carbon, Ind. Eng. Chem. 46 (1954) 2195–2202.
[404] Y. Wang, J.M. Zhou, Q.B. Li, G.D. Lin, H.B. Zhan, Intrinsic kinetics of pyrolysis of CH_4 to grow CNTs over a Ni–Mg–O catalyst, J. Xiamen Univ. 43 (2004) 522 (in Chinese).
[405] Y. Zhang, K.J. Smith, A kinetic model of CH_4 decomposition and filamentous carbon formation on supported Co catalysts, J. Catal. 231 (2005) 354–364.
[406] M. Borghei, R. Karimzadeh, A. Rashidi, N. Izadi, Kinetics of methane decomposition to CO_x-free hydrogen and carbon nanofiber over Ni–Cu/MgO catalyst, Int. J. Hydrogen Energy 35 (2010) 9479–9488.
[407] G.G. Kuvshinov, Y.I. Mogilnykh, D.G. Kuvshinov, Kinetics of carbon formation from CH_4–H_2 mixtures over a nickel containing catalyst, Catal. Today 42 (1998) 357–360.
[408] N. Latorre, E. Romeo, J.I. Villacampa, F. Cazana, C. Royo, A. Monzon, Kinetics of carbon nanotubes growth on a Ni–Mg–Al catalyst by CCVD of methane: influence of catalyst deactivation, Catal. Today 154 (2010) 217–223.
[409] I. Kvande, D. Chen, Z. Yu, M. Ronning, A. Holmen, Optimization and scale-up of CNF production based on intrinsic kinetic data obtained from TEOM, J. Catal. 256 (2008) 204–214.
[410] Y.A. Zhu, X.G. Zhou, D. Chen, W.K. Yuan, First-principles study of C adsorption and diffusion on the surfaces and in the subsurfaces of nonreconstructed and reconstructed Ni (1 0 0), J. Phys. Chem. C 111 (2007) 3447–3453.
[411] Y.A. Zhu, Y.C. Dai, D. Chen, W.K. Yuan, First-principles study of carbon diffusion in bulk nickel during the growth of fishbone-type carbon nanofibers, Carbon 45 (2007) 21–27.
[412] A. Steinfeld, V. Kirillov, G. Kuvshinov, Y. Mogilnykh, A. Reller, Production of filamentous carbon and hydrogen by solarthermal catalytic cracking of methane, Chem. Eng. Sci. 52 (1997) 3599–3603.
[413] N. Muradov, Hydrogen via methane decomposition: an application for decarbonization of fossil fuels, Int. J. Hydrogen Energy 26 (2001) 1165–1175.
[414] B.C. Liu, S.H. Tang, L.Z. Gao, Q. Liang, B.L. Zhang, M.Z. Qu, G.Z. Xiong, Z.L. Yu, Preparation of carbon nanotubes using a fluidized bed reactor, Chin. J. Catal. 22 (2001) 151–153.
[415] W.Z. Qian, T. Liu, F. Wei, Z.W. Wang, Y.D. Li, Enhanced production of carbon nanotubes: combination of catalyst reduction and methane decomposition, Appl. Catal. A: Gen. 258 (2004) 121–124.
[416] N. Shah, S. Ma, Y. Wang, G.P. Huffman, Semi-continuous hydrogen production from catalytic methane decomposition using a fluidized-bed reactor, Int. J. Hydrogen Energy 32 (2007) 3315–3319.
[417] C.H. See, O.M. Dunens, K.J. MacKenzie, A.T. Harris, Process parameter interaction effects during carbon nanotube synthesis in fluidized beds, Ind. Eng. Chem. Res. 47 (2008) 7686–7692.
[418] C.H. See, A.T. Harris, A review of carbon nanotube synthesis via fluidized-bed chemical vapor deposition, Ind. Eng. Chem. Res. 46 (2007) 997–1012.
[419] F. Danafara, A. Fakhrul-Razi, M.A.M. Salleha, D.R.A. Biaka, Fluidized bed catalytic chemical vapor deposition synthesis of carbon nanotubes – a review, Chem. Eng. J. 155 (2009) 37–48.
[420] K.J. MacKenzie, O.M. Dunens, A.T. Harris, An updated review of synthesis parameters and growth mechanisms for carbon nanotubes in fluidized beds, Ind. Eng. Chem. Res. 49 (2010) 5323–5338.
[421] Y. Wang, G. Gu, F. Wei, J. Wu, Fluidization and agglomerate structure of SiO_2 nanoparticles, Powder Technol. 124 (2002) 152–159.
[422] Y. Wang, F. Wei, G. Gu, H. Yu, Agglomerated carbon nanotubes and its mass production in a fluidized-bed reactor, Physica B 323 (2002) 327–329.
[423] H. Yu, Q.F. Zhang, F. Wei, W.Z. Qian, G.H. Luo, Agglomerated CNTs synthesized in a fluidized bed reactor: agglomerate structure and formation mechanism, Carbon 41 (2003) 2855–2863.
[424] P. Ammendola, R. Chirone, G. Ruoppolo, G. Russo, Production of hydrogen from thermo-catalytic decomposition of methane in a fluidized bed reactor, Chem. Eng. J. 154 (2009) 287–294.
[425] J.L. Pinilla, M.J. Lazaro, I. Suelves, R. Moliner, J.M. Palacios, Characterization of nanofibrous carbon produced at pilot-scale in a fluidized bed reactor by methane decomposition, Chem. Eng. J. 156 (2010) 170–176.
[426] P. Ammendola, R. Chirone, G. Ruoppolo, G. Russo, R. Solimene, Some issues in modelling methane catalytic decomposition in fluidized bed reactors, Int. J. Hydrogen Energy 33 (2008) 2679–2694.
[427] H.T. Jang, W.S. Cha, Hydrogen production by the thermocatalytic decomposition of methane in a fluidized bed reactor, Korean J. Chem. Eng. 24 (2007) 374–377.
[428] R.A. Couttenye, M.H. de vila, S.L. Suib, Decomposition of methane with an autocatalytically reduced nickel catalyst, J. Catal. 233 (2005) 317–326.
[429] S.G. Zavarukhin, G.G. Kuvshinov, Mathematic modeling of the process of production of nanofibrous carbon from methane in an isothermal reactor with a fixed bed of the Ni–Al_2O_3 catalyst, Chem. Eng. J. 120 (2006) 139–147.
[430] S.G. Zavarukhin, G.G. Kuvshinov, Mathematical modeling of continuous production of carbon nanofibers from methane in a reactor with a moving bed of a nickel-containing catalyst, Theor. Found. Chem. Eng. 40 (2006) 519–525.
[431] S.G. Zavarukhin, G.G. Kuvshinov, Mathematical modeling of the continuous process for synthesis of nanofibrous carbon in a moving catalyst bed reactor with recirculating gas flow, Chem. Eng. J. 137 (2008) 681–685.
[432] T. Ishihara, Y. Miyashita, H. Iseda, Y. Takita, Decomposition of methane over Ni/SiO_2 catalysts with membrane reactor for the production of hydrogen, Chem. Lett. 2 (1995) 93–94.
[433] T. Ishihara, K. Nishida, H. Nishiguchi, Y. Takita, K. Chaki, A new reforming process based on CH_4 decomposition using a hydrogen-permeating membrane reactor, Res. Chem. Intermed. 32 (2006) 253–262.
[434] T. Ishihara, A. Kawahara, A. Fukunaga, H. Nishiguchi, H. Shinkai, M. Miyaki, Y. Takita, CH_4 decomposition with a Pd–Ag hydrogen-permeating membrane reactor for hydrogen production at decreased temperature, Ind. Eng. Chem. Res. 41 (2002) 3365–3369.
[435] G. Italiano, C. Espro, F. Arena, F. Frusteri, A. Parmaliana, Catalytic decomposition of natural gas for CO_x-free hydrogen production in a structured multilayer reactor, Appl. Catal. A: Gen. 357 (2009) 58–65.
[436] G. Italiano, A. Delia, C. Espro, G. Bonura, F. Frusteri, Methane decomposition over Co thin layer supported catalysts to produce hydrogen for fuel cell, Int. J. Hydrogen Energy 35 (2010) 11568–11575.
[437] J.L. Pinilla, R. Utrilla, M.J. Lazaro, I. Suelves, R. Moliner, J.M. Palacios, A novel rotary reactor configuration for simultaneous production of hydrogen and carbon nanofibers, Int. J. Hydrogen Energy 34 (2009) 8016–8022.
[438] L. Martinez-Latorre, P. Ruiz-Cebollada, A. Monzon, E. Garcia-Bordeje, Preparation of stainless steel microreactors coated with carbon nanofiber layer: impact of hydrocarbon and temperature, Catal. Today 147 (2009) S87–S93.
[439] L. Martinez-Latorre, S. Armenise, E. Garcia-Bordeje, Temperature-mediated control of the growth of an entangled carbon nanofiber layer on stainless steel micro-structured reactors, Carbon 48 (2010) 2047–2056.
[440] A. Agiral, L. Lefferts, J.G.E. Gardeniers, In situ CVD of carbon nanofibers in a microreactor, Catal. Today 150 (2010) 128–132.
[441] S.W. Liu, Z.H. Ye, F. Liang, Q.R. Liu, Y.D. Li, Hydrogen production from methane decomposition and catalyst regeneration by air in a fluidized bed reactor, J. Fuel Chem. Technol. 34 (2006) 567–571.
[442] P. Ferreira-Aparicio, I. Rodriguez-Ramos, A. Guerrero-Ruiz, Methane interaction with silica and alumina supported metal catalysts, Appl. Catal. A: Gen. 148 (1997) 343–356.
[443] Y. Zhang, K.J. Smith, CH_4 decomposition on Co catalysts: effect of temperature, dispersion, and the presence of H_2 or CO in the feed, Catal. Today 77 (2002) 257–268.
[444] W.Z. Qian, T. Tian, C.Y. Guo, Q. Wen, K.J. Li, H.B. Zhang, H.B. Shi, D.Z. Wang, Y. Liu, Q. Zhang, Y.X. Zhang, F. Wei, Z.W. Wang, X.D. Li, Y.D. Li, Enhanced activation and decomposition of CH_4 by the addition of C_2H_4 or C_2H_2 for hydrogen and carbon nanotube production, J. Phys. Chem. C 112 (2008) 7588–7593.

[445] N.Z. Muradov, CO_2-free production of hydrogen by catalytic pyrolysis of hydrocarbon fuel, Energy Fuels 12 (1998) 41–48.
[446] K. Asai, K. Takane, Y. Nagayasu, S. Iwamoto, E. Yagasaki, M. Inoue, Decomposition of methane in the presence of carbon dioxide over Ni catalysts, Chem. Eng. Sci. 63 (2008) 5083–5088.
[447] L. Cao, J.L. Chen, S.W. Liu, Y.D. Li, Hydrogen from stepwise reforming of methane: a process analysis, Stud. Surf. Sci. Catal. 147 (2004) 103–108.
[448] N.Z. Muradov, T.N. Veziroglu, "Green" path from fossil-based to hydrogen economy: an overview of carbon-neutral technologies, Int. J. Hydrogen Energy 33 (2008) 6804–6839.
[449] M.K. van der Lee, A.J. van Dillen, J.W. Geus, K.P. de Jong, J.H. Bitter, Catalytic growth of macroscopic carbon nanofiber bodies with high bulk density and high mechanical strength, Carbon 44 (2006) 629–637.
[450] J.L. Chen, Q.H. Chen, Y.D. Li, Characterization and adsorption properties of porous carbon nanofiber granules, China Particuol. 4 (2006) 238–242.
[451] N.Q. Zhao, C.N. He, Z.Y. Jiang, J.J. Li, Y.D. Li, Fabrication and growth mechanism of carbon nanotubes by catalytic chemical vapor deposition, Mater. Lett. 60 (2006) 159–163.
[452] N.Q. Zhao, C.N. He, J.J. Li, Z.Y. Jiang, Y.D. Li, Study on purification and tip-opening of CNTs fabricated by CVD, Mater. Res. Bull. 41 (2006) 2204–2209.
[453] N.Q. Zhao, C.N. He, Z.Y. Jiang, J.J. Li, Y.D. Li, Physical activation and characterization of multi-walled carbon nanotubes catalytically synthesized from methane, Mater. Lett. 61 (2007) 681–685.
[454] NanoSEE 2008: Nanomaterials Industrial Status and Expected Evolution.
[455] M.G. Poirier, C. Sapundzhiev, Catalytic decomposition of natural gas to hydrogen for fuel cell applications, Int. J. Hydrogen Energy 22 (1997) 429–433.
[456] K. Otsuka, S. Takenaka, H. Ohtsuki, Production of pure hydrogen by cyclic decomposition of methane and oxidative elimination of carbon nanofibers on supported-Ni-based catalysts, Appl. Catal. A: Gen. 273 (2004) 113–124.
[457] T.V. Choudhary, D.W. Goodman, CO-free production of hydrogen via stepwise steam reforming of methane, J. Catal. 192 (2000) 316–321.
[458] S. Takenaka, Y. Tomikubo, E. Kato, K. Otsuka, Sequential production of H_2 and CO over supported Ni catalysts, Fuel 83 (2004) 47–57.
[459] J. Li, K.J. Smith, Methane decomposition and catalyst regeneration in a cyclic mode over supported Co and Ni catalysts, Appl. Catal. A: Gen. 349 (2008) 116–124.
[460] K. Otsuka, A. Mito, S. Takenaka, I. Yamanaka, Production of hydrogen from methane without CO_2-emission mediated by indium oxide and iron oxide, Int. J. Hydrogen Energy 26 (2001) 191–194.
[461] P. Serp, M. Corrias, P. Kalck, Carbon nanotubes and nanofibers in catalysis, Appl. Catal. A: Gen. 253 (2003) 337–358.
[462] T.D. Tang, J.L. Chen, Y.D. Li, Study on sulfur tolerance of Pd–Pt catalyst supported on carbon nanofibers for hydrogenation of naphthalene to tetralin, Chin. J. Chem. Phys. 18 (2005) 1–3.
[463] T.D. Tang, J.L. Chen, Y.D. Li, Treatment of the carbon nanofiber surfaces in mixed concentrated HNO_3–H_2SO_4, and the catalytic activity of supported Pd–Pt for naphthalene hydrogenation, Acta Phys.-Chim. Sin. 21 (2005) 730–734.
[464] M. Lebert, M. Kaempgen, M. Soehn, T. Wirth, S. Roth, N. Nicoloso, Fuel cell electrodes using carbon nanostructures, Catal. Today 143 (2009) 64–68.
[465] R. Dagani, Putting the 'NANO' into composites, C&EN 77 (23) (1999) 25–37.
[466] R.T. Yang, Hydrogen storage by alkali-doped carbon nanotubes-revisited, Carbon 38 (2000) 623–641.
[467] L. Zhou, Y.P. Zhou, Determination of compressibility factor and fugacity coefficient of hydrogen in studies of adsorptive storage, Int. J. Hydrogen Energy 26 (2001) 597–601.
[468] F.H. Yang, R.T. Yang, Ab initio molecular orbital study of adsorption of atomic hydrogen on graphite: insight into hydrogen storage in carbon nanotubes, Carbon 40 (2002) 437–444.
[469] L. Zhou, Progress and problems in hydrogen storage methods, Renew. Sustain. Energy Rev. 9 (2005) 395–408.
[470] G.G. Tibbetts, M.L. Lake, K.L. Strong, B.P. Rice, A review of the fabrication and properties of vapor-grown carbon nanofiber/polymer composites, Compos. Sci. Technol. 67 (2007) 1709–1718.
[471] M.H. Al-Saleh, U. Sundararaj, A review of vapor grown carbon nanofiber/polymer conductive composites, Carbon 47 (2009) 2–22.
[472] P.J.F. Harris, Carbon nanotube composites, Int. Mater. Rev. 49 (2004) 31–43.
[473] M. Steinberg, Conversion of fossil and biomass fuels to electric power and transportation fuels by high efficiency integrated plasma fuel cell (IPFC) energy cycle, Int. J. Hydrogen Energy 31 (2006) 405–411.
[474] Q.H. Liu, Y. Tian, H.J. Li, L.J. Jia, C. Xia, L.T. Thompsonb, Y.D. Li, High efficiency chemical energy conversion system based on methane catalytic decomposition reaction and two fuel cells. Part II. Exergy analysis, J. Power Sources 195 (2010) 6532–6538.
[475] D.X. Cao, Y. Sun, G.L. Wang, Direct carbon fuel cell: fundamentals and recent developments, J. Power Sources 167 (2007) 250–257.
[476] Q.H. Liu, Y. Tian, C. Xia, L.T. Thompson, B. Liang, Y.D. Li, Modeling and simulation of a single direct carbon fuel cell, J. Power Sources 185 (2008) 1022–1029.
[477] H.J. Li, Q.H. Liu, Y.D. Li, A carbon in molten carbonate anode model for a direct carbon fuel cell, Electrochim. Acta 55 (2010) 1958–1965.
[478] W.W. Jacques, US Patent No. 555,551, 1896.
[479] J.F. Cooper, K. Berner, Presented in Fuel Cell Seminar, Direct Carbon Fuel Cell Workshop, Palm Springs, CA, USA, 14th November, 2005. Proceedings online: http://www.fuelcellseminar.com/pdf/Direct Carbon Fuel Cell Workshop/Cooper John.pdf.
[480] S. Zacevic, Presented in Direct Carbon Fuel Cell Workshop, NETL, Pittsburg, PA, USA, 30th July, 2003. Proceedings online: http://www.netl.doe.gov/publications/proceedings/03/dcfcw/Zecevic.pdf.
[481] I.I. Balachov, L.H. Dubois, M.D. Hornbostel, A.S. Lipilin, Presented in Fuel Cell Seminar, Direct Carbon Fuel Cell Workshop, Palm Springs, CA, USA, 14th November, 2005. Proceedings online: http://www.fuelcellseminar.com/pdf/Direct Carbon Fuel Cell Workshop/Balachov Iouri.pdf.
[482] L.J. Jia, Y. Tian, Q.H. Liu, C. Xia, J.S. Yu, Z.M. Wang, Y.C. Zhao, Y.D. Li, A direct carbon fuel cell with (molten carbonate)/(doped ceria) composite electrolyte, J. Power Sources 195 (2010) 5581–5586.
[483] Y.D. Li, Z.B. Rui, C. Xia, M. Anderson, Y.S. Lin, Performance of ionic-conducting ceramic/carbonate composite material as solid oxide fuel cell electrolyte and CO_2 permeation membrane, Catal. Today 148 (2009) 303–309.
[484] C. Xia, Y. Li, Y. Tian, Q.H. Liu, Y.C. Zhao, L.J. Jia, Y.D. Li, A high performance composite ionic conducting electrolyte for intermediate temperature fuel cell and evidence for ternary ionic conduction, J. Power Sources 188 (2009) 156–162.
[485] C. Xia, Y. Li, Y. Tian, Q.H. Liu, Z.M. Wang, L.J. Jia, Y.C. Zhao, Y.D. Li, Intermediate temperature fuel cell with a doped ceria–carbonate composite electrolyte, J. Power Sources 195 (2010) 3149–3154.
[486] Z.B. Rui, M. Anderson, Y.S. Lin, Y.D. Li, Modeling and analysis of carbon dioxide permeation through ceramic–carbonate dual-phase membranes, J. Membr. Sci. 345 (2009) 110–118.
[487] J.L. Chen, X. Yang, Y.D. Li, Investigation on the structure and the oxidation activity of the solid carbon produced from catalytic decomposition of methane, Fuel 89 (2010) 943–948.
[488] N.J. Cherepy, R. Krueger, K.J. Fiet, A.F. Jankowski, J.F. Cooper, Direct conversion of carbon fuels in a molten carbonate fuel cell, J. Electrochem. Soc. 152 (2005) A80–A87.